

**Regional Scale Land-Atmosphere Carbon Dioxide
Exchange: Data Design and Inversion within a Receptor
Oriented Modeling Framework**

A thesis presented by

Daniel Michael Matross

to

The Department of Earth and Planetary Sciences

in partial fulfillment of the requirements

for the degree of

Doctor of Philosophy

in the subject of

Earth and Planetary Sciences

Harvard University

Cambridge, Massachusetts

September, 2006

© 2006 Daniel Michael Matross

All Rights Reserved.

Dissertation Advisor: Professor Steven C. Wofsy

Author: Daniel M. Matross

Regional Scale Land-Atmosphere Carbon Dioxide Exchange: Data Design
and Inversion within a Receptor Oriented Modeling Framework

Abstract: This thesis presents a model-data fusion study to derive regional-scale ($\sim 10^4$ km²) CO₂ flux estimates for summer 2004 in the northeast United States and southern Quebec, using an end-to-end treatment that goes from strategizing observations to assimilating extensive data into a receptor-oriented modeling framework. Surface fluxes are specified using the Vegetation Photosynthesis and Respiration Model (VPRM), a simple, readily optimized biosphere model driven by satellite data, AmeriFlux eddy covariance measurements, and meteorological fields. The surface flux model is coupled to a Lagrangian atmospheric adjoint model, the Stochastic Time-Inverted Lagrangian Transport Model (STILT), which links point observations to upwind sources with high spatio-temporal resolution. Concentration data for assimilation comes from the CO₂ Budget and Regional Airborne Maine (COBRA-Maine) airborne campaign—which is described fully—and the NOAA-ESRL tall tower at Argyle, ME, as well as an ad-hoc regional network of surface observation stations. The variety of independent constraints provided by each input demonstrates the need for large amounts of data, shows the importance of both spatial and temporal coverage, and emphasizes the complementarity of tower and airborne observations. Although the dataset is dense and regionally representative, the surface source function is relatively insensitive to Bayesian optimization, providing an important counterexample to the current working paradigm of CO₂ data assimilation studies. Errors in transport and tracer boundary conditions and in representation of the atmospheric boundary layer contribute to variance at the surface which is large enough to limit the effectiveness of atmospheric data assimilation for constraining surface fluxes.

Table of Contents

<i>Abstract</i>	iii
<i>Acknowledgements</i>	vi
Chapter 1: Introduction	1
Chapter 2: Flight design and survey of observations from the COBRA-Maine airborne intensive campaign	5
2.1 Abstract.....	5
2.2 Introduction.....	5
2.3 Mission strategy.....	7
2.4 Flight Planning.....	17
2.4.1 General flight planning.....	17
2.4.2 Transit flights.....	21
2.4.3 Lagrangian experiments.....	24
2.5 Weather and climate during COBRA-Maine.....	34
2.6 Makeup of COBRA-Maine observations available for model use.....	39
2.7 Conclusion.....	60
Chapter 3: Estimating regional carbon exchange in New England and Quebec by combining atmospheric, ground based and satellite data	61
3.1 Abstract.....	61
3.2 Introduction.....	62
3.3 Methodology.....	65
3.3.1 STILT adjoint atmospheric model.....	65
3.3.2 Empirical lateral tracer boundary condition.....	67
3.3.3 Fossil fuel inventory.....	68
3.3.4 Vegetation photosynthesis and respiration model.....	69
3.3.5 Argyle tall tower measurements.....	73
3.3.6 Application of STILT+VPRM at Argyle tall tower.....	74
3.3.7 Optimization approach.....	75
3.4 Results and Discussion.....	79
3.4.1 Comparison of observations and initially calibrated STILT+VPRM results.....	79
3.4.2 Footprint and vegetation influence.....	83
3.4.3 Comparison of COBRA-Maine airborne data.....	88
3.4.4 Bayesian optimization incorporating tower concentration observations.....	93
3.5 Conclusions.....	96

Chapter 4: Assimilation of regional surface and network observations for CO₂ flux estimates from a receptor oriented modeling framework..	98
4.1 Abstract.....	98
4.2 Introduction.....	99
4.3 Data and Methods.....	102
4.3.1 Data for assimilation.....	102
4.3.2 STILT+VPRM receptor oriented modeling framework.....	104
4.3.2.1 STILT adjoint transport model.....	104
4.3.2.2 Fossil fuel inventory.....	107
4.3.2.3 VPRM CO ₂ surface flux model.....	107
4.3.3 Lateral tracer boundary condition.....	109
4.3.4 Optimization Setup.....	114
4.3.4.1 Receptor a priori concentration.....	114
4.3.4.2 Additive optimization factor.....	117
4.3.4.3 Bayesian framework.....	119
4.3.4.4 Definition of prior parameter uncertainty.....	121
4.3.4.5 Definition of error covariance matrix for measurements.....	122
4.3.4.6 Spatial and temporal correlation within the dataset.....	125
4.4 A priori model comparisons.....	129
4.4.1 Effects of meteorological driver fields.....	129
4.4.2 Application of the revised boundary condition.....	133
4.4.3 Airborne cross-section case study.....	135
4.4.4 Regionally specific representation error in the source function.....	142
4.5 Optimization results.....	146
4.6 Conclusion.....	155
Chapter 5: Summary and Conclusions.....	159
References.....	165

Acknowledgements

An often quoted African proverb says “It takes a village to raise a child”. It would also seem it takes a village to finish a doctorate. There are many whom I must acknowledge in helping me complete the work in this thesis and some of the work that didn’t quite make it in, but was equally instrumental in my graduate education. First and foremost, I must give deep thanks to Steve Wofsy for his eternal patience, creative problem solving, and absolute commitment to producing quality data and analysis. As the liberal quantity of references would indicate, the work presented here rests on the foundation John Lin and Christoph Gerbig collaboratively built and generously gave me. I thank them both for their continued input. I also must acknowledge other current and former members of the Wofsy group: Bruce Daube for his careful engineering and attention to all the other details that went into collecting the many of the observations analyzed here; Scott Saleska for helping me develop data analysis skills in my first two years; Bill Munger for his willingness to answer any and all questions about everything; Pathmathevan Mahadevan for developing many of the tools used in this analysis; and the corps of graduate students who have shared all or part of the Wofsy experience. All members of the Wofsy group had either direct or indirect impact on this work, so some credit must go to them.

Two fellowships have supported me during my graduate work: 1) A first-year graduate school fellowship awarded by the American Meteorological Society and generously funded by the National Science Foundation Division of Atmospheric Sciences. 2) A three-year NASA Earth System Science Fellowship (NGT5-30495). I thank both the AMS and NASA for their generous support.

I also thank my many friends who have kept me sane with frothy excursions from Madrid to Mendoza, Acton to Back Bay to Cambridge, and Somerville to Santa Monica; to maintain brevity I'll forego listing all my friends and instead express my appreciation in person, perhaps over a cold beverage. Beyond your encouragement, I am grateful for the willingness of all of you to take an interest in my work, help me keep it in touch with the real world, and explain it in both human and scientific terms. It goes almost without saying that my parents and family have provided never ending support and maintained a constant base to which I can always turn. Thank you.

Finally, I extend all my gratitude to Melissa Goldstein. She is the skilled sailor who has kept my ship upright and on an even keel in weather stormy and fair. I look forward to future adventures with her.

Chapter 1: Introduction

Regional scale ($\sim 10^4$ km²) terrestrial carbon budgets are vital to assessment of human impact on ecosystems and atmospheric composition, but obtaining and validating regional-scale fluxes of CO₂, one of the most biologically important trace gases, remains a scientific challenge. Much information has been gained from observing the distribution of atmospheric CO₂ and using it to infer surface fluxes through inversion studies (e.g. Tans et al., 1990). Early efforts have evolved into sophisticated CO₂ data assimilation studies which seek to use atmospheric observations to constrain vegetation flux models, but these have mainly focused on the global scale, splitting the world into 10-20 very large ($\sim 10^6$ to 10^8 km²) regions on monthly to annual timescales (e.g. Gurney et al., 2002; Gurney et al., 2004). The coarse scale and global focus are required in part because the observational network has been focused mainly on marine locations free from the influence of the terrestrial biosphere (Wofsy and Harriss, 2002; Patra et al., 2006) and in part because of formidable aggregation errors and transport errors that arise when global models attempt to represent atmospheric boundary layer processes over land (Gloor et al., 1999, Kaminski and Heimann, 2001).

Recently, the quantity and quality of terrestrial observations has increased enough to allow the use of daily, monthly, and seasonal terrestrial observations to constrain biophysical surface flux models – with tall (> 100 m) towers and airborne campaigns (e.g. Lin et al., 2006) offering terrestrial CO₂ concentration datasets representative of regional and continental scale influences. Modeling efforts have expanded as well. A number of studies have focused on using eddy covariance measurements (Law et al.,

2002) for information about temporal variability and environmental controls of land-atmosphere CO₂ exchange (Rastetter et al., 2003; Baldocchi, 2003), but the localized footprint of micrometeorological measurements presents difficulties in developing and testing regional flux models (Medlyn et al., 2005; Hollinger and Richardson, 2005). Increasing attention has therefore been paid to developing a set of rigorous optimization techniques (e.g. Michelak et al, 2004; Peters et al., 2005) and model-data fusion frameworks (Nicholls et al., 2004; Gerbig et al., 2003b) for assimilation of terrestrial CO₂ observations which can take full advantage of growing terrestrial atmospheric datasets.

The progression of data assimilation methodology and increase in continental observations together create substantial new opportunities to better quantify regional scale CO₂ fluxes, but the success of model-data fusion studies rests on detailed knowledge of limitations posed by the makeup of observations and limitations within models which are not affected by observations. Optimal solutions depend on merging an overall strategy for data collection with a modeling framework in a way that maximizes information transfer and minimizes error propagation. The co-development of observations and data assimilation techniques is only now reaching the stage where studies can explore how to best achieve these goals.

The overall objective of this thesis is to build a detailed, fully integrated link between observational strategies, multi-modal datasets, and modeling techniques to better understand the interplay between them within the context of quantifying regional scale terrestrial CO₂ exchange. A model-data fusion study of the northeast United States and southern Quebec in summer 2004 is presented in its entirety including conceptualizing the observation strategy and collecting the data; developing an enhanced assimilation

framework with a realistic surface flux parameterization; and applying an optimization that elucidates emergent aspects of the dataset and some of the infrequently explored limitations of currently available modeling techniques. Chapter 2 gives a full description of the CO₂ Budget and Regional Airborne – Maine (COBRA-Maine) campaign, the primary dataset, and a catalogue of sample observations with implications for data assimilation. Chapter 3 develops the STILT+VPRM receptor oriented modeling framework using tall tower data from the NOAA Global Monitoring Division Earth Systems Research Lab, complemented by the airborne observations. An optimization using the airborne dataset and a full regional network of surface observations makes up Chapter 4. Finally, Chapter 5 briefly summarizes the central findings and offers suggestions for future research.

Most of the work described has developed within a strongly collaborative environment. Of the various field campaigns in which I have participated as a doctoral student, COBRA-Maine was by far my deepest involvement. I was given the opportunity utilize instrument skills to collect and process much of the airborne CO₂ data presented, as well as nearly all of the CO data. Bruce Daube and Christoph Gerbig respectively should be credited as primary scientists for those instruments. Chapter 2 contains numerous small personal insights I gained during the 125 flight hours I spent onboard the research plane and the selection of data shown represents only a sample of the atmospheric phenomenon encountered. The discussions of flight planning in Chapter 2 are meant to showcase the considerable efforts of John Lin, Elaine Gottlieb, and V. Y. Chow.

Pathmathevan Mahadevan deserves most credit for developing the VPRM as a surface flux model from Xiangming Xiao's original ideas, but fully coupling it with John Lin's STILT model and Christoph Gerbig's receptor-oriented modeling framework and the forward model-data comparisons are my own contribution. Although I had some data in hand, the inversion work I conceptualized and executed in Chapters 3 and 4 depends on the willingness of collaborators to collect and share their data: foremost Arlyn Andrews for providing tall tower data at Argyle as well as WLEF, Bill Munger for Harvard Forest fluxes and concentrations, David Hollinger and John T. Lee for Howland Forest concentrations and fluxes, Hank Margolis for Fluxnet Canada Eastern Old Black Spruce Fluxes, Pieter Beckman and the University of New Hampshire AIRMAP program for concentrations at Thompson Farm, and finally Allen Goldstein and Dylan Millet for Chebogue Point concentration data.

COBRA-Maine was supported by a grant from the National Science Foundation Biocomplexity in the Environment Program (ATM-0221850).

Chapter 2: Flight design and survey of observations from the COBRA- Maine airborne intensive campaign

2.1 Abstract

Regional and continental terrestrial CO₂ exchange modeling studies can benefit greatly from airborne measurements, but their utility depends critically on mission strategy and flight design. This paper describes observations taken during the CO₂ Budget and Regional Airborne – Maine (COBRA-Maine) mission, an extensive and highly successful summer 2004 airborne campaign which sought to sample the boundary layer and free troposphere over New England and southern Quebec in order to link surface biological processes to their atmospheric signature. The full environmental and operational context of the mission is described, with emphasis on the mission and flight planning strategies developed to balance scientific goals with operational realities. Sample data, including cross-sections, vertical profiles, surface fluxes, and photographs, demonstrate the wide range of atmospheric conditions encountered and are discussed in terms of their implications for modeling studies.

2.2 Introduction

The work within this thesis rests upon the foundation of surface and airborne data collected during the summer 2004 CO₂ Budget and Regional Airborne –Maine (COBRA-Maine) campaign. COBRA-Maine started with the goal to link process-level biological knowledge gained from individual plants or ecosystems on short time scales to observations and models characterizing the regional and global scale interactions between

terrestrial ecosystems and the atmosphere. Aside from the transit flights across the continent, the COBRA-Maine airborne campaign maintained a nearly exclusive focus on regional flights in New England and Southern Quebec with an overarching objective to establish how well carbon fluxes in a limited region could be constrained (Lin et al., 2006). Maine and Southern Quebec comprise one of the best regions to initiate such comprehensive data and model studies because it has a comparatively contiguous landscape dominated by forests and generally removed from strong urban influences, a long tradition of forest investigations, relatively dense surface measurements, a strong biosphere-atmosphere exchange signal, and marked seasonality. Intensive airborne data expand a spectrum of data that already exists for the region: a recently installed tall tower observation station, long-running eddy covariance data at several sites, leaf level measurements, multi-decadal stand level assessments, and disturbance reconstructions (Medvigy, 2006).

The full spectrum of spatial and temporal scales represented in COBRA-Maine comprises an unprecedented surface and airborne dataset for use within an assimilation framework that couples a mechanistic terrestrial biosphere surface flux model to an atmospheric transport model. The inversion work presented in later chapters represents an important step forward in a developing such a data assimilation framework and gives an intermediate vantage point from which to reassess the original design of the observations and the ongoing design of future coupled data assimilation studies. A reassessment of COBRA-Maine airborne strategy using insights from post-hoc analyses is especially important as the geographic scope of campaign-mode airborne data expands with an

upcoming mission in the Amazon that political and regulatory concerns dictate will not soon be repeated.

Interpreting the many small but critical facets of regional inversion studies that make use of the rich COBRA-Maine observations depends on a detailed understanding of the dataset. Information that seems auxiliary at first has shaped the formulation of the inversion setup and interpretation of inversion results. Significant effort was put into mission design, flight strategy, and operational implementation to create an optimal dataset for inversion. When combined with knowledge gained from inversion studies, the mission design and data aspects represent an experiment unto themselves, addressing the question of how best to collect targeted regional data for assimilation to quantify surface CO₂ fluxes. This chapter provides the details of COBRA-Maine data strategy, collection, and analysis, so as to provide a comprehensive starting point for the regional inversion studies shown later and a lens through which to focus the inversion design. It also serves as a reference point for a later discussion of how future observational campaigns might be better designed based on knowledge gained from optimization of COBRA-Maine data.

2.3 Mission Strategy

COBRA-Maine is one in an ongoing series of CO₂ Budget and Regional Airborne (COBRA) experiments begun in 2000 (Lin et al., 2006). The COBRA program seeks to use aircraft to fill an observational gap by measuring CO₂ in the continental planetary boundary layer, as well as observe the horizontal variability on scales from 10¹ to 10³ km (Stephens et al., 2000; Lin et al., 2006). Common to all the COBRA campaigns is some combination of large-scale surveys on a continental scale of 10³ km and regional

influence-following pseudo-Lagrangian experiments (Lin et al., 2004) which span a more regional horizontal scale of 10^2 km, along with extensive vertical profiling from the surface up to 6-7 km. The proportion of continental-scale and regional-scale flights has varied across the experiments, but all experiments emphasize obtaining the maximum possible number of vertical profiles.

Even though it had the smallest operational scale and fewest flight hours, data from the first experiment, COBRA-2000, have been most extensively analyzed (Lin et al., 2004; Gerbig et al. 2003a; Gerbig et al., 2003b). In part, this is because COBRA-2000 served as a developmental prototype for the longer, more extensive campaigns that have followed. It was the first opportunity to employ an initial version of the Stochastic Time-Inverted Lagrangian Transport model (STILT; Lin et al., 2003) and develop methodology for the Lagrangian influence experiments that would become the central strategy for COBRA-Maine. COBRA-2003, originally meant to be deployed in the Brazilian Amazon but redeployed at the last minute to the U.S. and Canada, made two large loops of North America, traversing from east coast to west coast across the heartland of the U.S. and west coast to east coast through central Canada. By primarily focusing on long transects, COBRA-2003 proved it was logistically feasible to use an aircraft to obtain atmospheric concentration information at the horizontal, vertical, and temporal resolution necessary to inform continental-scale terrestrial carbon exchange models. COBRA-Maine is complementary to COBRA-2003 and was designed to quantify regional scale processes, utilizing long transects only in transiting the aircraft from its base in Wyoming to Maine. The mission strategy for the next experiment in the series, planned for Brazil in late 2006 under the Portuguese moniker “BARCA” (Balanço Atmosférico Regional de Carbono na

Amazônia; Regional Atmospheric Carbon Budget in Amazonia), is currently under development and will take into consideration scientific and operational lessons learned from the three COBRA missions.

The strategic scale and location for COBRA-Maine experiments were determined in part by the scientific enhancement that comes by linking flights directly to continuous tower-based regionally-representative CO₂ concentration measurements, in this case to NOAA's Earth Systems Research Laboratory Global Monitoring Division (ESRL-GMD) Argyle 107-m tall tower observation station in central Maine (45.20° N 68.74° N) established in fall 2003 as part of the COBRA-Maine experiment. GMD monitors CO₂ and CO at the 107 m level, with an additional CO₂ measurement at 25 m. In conjunction with eddy covariance CO₂ flux measurements on the Argyle tower and at Howland Forest located 19 km away (carried out by collaborators David Hollinger (USFS) and John T. Lee (University of Maine)), Argyle provides a surface based anchor point for the airborne observations. By centering the COBRA-Maine airborne campaign around the Argyle/Howland surface points, the spatially dense campaign-mode airborne data are linked to the temporally dense continuous tower observations. Harvard Forest provides a more distant (~400 km from Argyle) secondary anchor point, located in deciduous forest, rather than the mixed forest regime that dominates central Maine and Southern Quebec.

Logistically and scientifically, Bangor, ME was the obvious choice for the primary operational base in COBRA-Maine. Bangor provided a long runway, a U.S. customs point of entry, commercial transportation options, and extensive aircraft maintenance facilities. Having a logistically optimal base greatly increased the scientific flexibility for planning individual Lagrangian experiments. More importantly, the close

proximity of Bangor airport to Argyle and Howland allowed fly-bys on every descent and ascent, for an unprecedented number of vertical profiles over the surface anchor point (Figures 2.1 and 2.2). Every climb-out and return represented an additional vertical profile and flights were planned as much as possible to begin and/or end with tower fly-bys to maximize the tower-aircraft intercomparison opportunities.



Figure 2.1 – Howland Forest fly-by at 50 m above the canopy. The tower appears just to right of the aircraft nose boom



Figure 2.2 – King Air fly-by of the Argyle Tall Tower at 100 m above the canopy. The tower is located on a direct line with aircraft noseboom just below the horizon. Interstate 95 can be seen on the right.

The airborne platform chosen for COBRA-Maine was a Raytheon King Air 200T twin engine turboprop operated by the University of Wyoming (<http://flights.uwyo.edu/>) and contracted by the National Science Foundation (Figure 2.3). The King Air is a single pilot mid-sized aircraft capable of extended operations in the boundary layer and climbs well into the mid-troposphere. For flights typical of COBRA-Maine, with numerous climbs and descents from the surface to service ceiling, the King Air has an effective duration around 4 hours and a range around 1500 km for a single flight. A primary constraint on flight operations in COBRA-Maine was duty restrictions for the pilot, which limited single day operations to 7 total flight hours.



Figure 2.3 – Exterior view of the University of Wyoming King Air in the hanger

Although a the University of Wyoming can supply a number of potential meteorological instrument packages, the COBRA-Maine payload consisted only of the main instrument package, the Harvard University CO₂ instrument (Daube et al., 2002), and the Harvard vacuum ultra violet CO instrument (Gerbig et al., 1999). Available flight data are listed in Table 2.1. Flight crew consisted of a pilot, a University of Wyoming technician to operate the main data system, and one or two scientists from Harvard. The role of the onboard scientist was to monitor the Harvard instruments, maintain a log of observations, and provide scientific input when requested by the pilot on flight decisions not explicitly covered in the flight plan.

Table 2.1 – List of variables measured by the King Air during COBRA-Maine

<u>Available Datastream</u>	<u>Data Provider</u>
Time	University of Wyoming
Pressure	University of Wyoming
Temperature	University of Wyoming
Pressure altitude	University of Wyoming
Radar altitude	University of Wyoming
Inertial Navigation System position	University of Wyoming
GPS position and altitude	University of Wyoming
Turbulence	University of Wyoming
Liquid water content	University of Wyoming
Potential Temperature	University of Wyoming

NDVI	University of Wyoming
H ₂ O mixing ratio	University of Wyoming
O ₃ mixing ratio	University of Wyoming
CO ₂ mixing ratio (NDIR)	Harvard University
CO mixing ratio (Vacuum UV)	Harvard University

COBRA-Maine was allocated 200 flight hours for the King Air, which was at the time the largest allocation of flight hours ever provided for a single experiment. The mission was done in two deployments of one-month each to capture seasonal variability, the first centered on the early season growing period for Maine and southern Quebec, and the second focused on the mid-summer season. After a two-week integration, science flights went from May 14th to June 14th and July 14th to August 16th, 2004. In total, the King Air made 59 takeoffs and landings during COBRA-Maine for a total of 193 and 9 minutes of airborne flight time. Ground operations consumed the remainder of the allocated hours. Table 2.2 gives a complete list of individual flights that occurred.

Table 2.2 – List of flights from COBRA-Maine

Date	Launch Time(s) GMT	Duration	Takeoff and Landing point(s)	Flight purpose
First Deployment				
May 7	1631	3:54	Laramie, WY	Test Flight
May 12	1921	3:39	Laramie, WY	Test Flight
May 14	1941	1:41	Laramie, WY	Transit
	2220	2:05	Huron, SD Rhineland, WI	
May 15	1537	3:08	Rhineland, WI	
	2108	2:23	Niagara Falls, NY Bangor, ME	
May 17	1249	4:07	Bangor, ME	Single-day Lagrangian experiment
	1918	2:27		
May 19	1230	3:36	Bangor, ME	Multi-day

	1854	2:09	Trois Rivieres, QC	Lagrangian experiment
May 20	1300	3:33	Bangor, ME	
May 25	1224 1926	3:52 3:47	Bangor, ME Nashua, NH	Single-day Lagrangian Experiment
May 29	1229 1932	3:59 3:09	Bangor, ME Timmons, ON	Multi-day Lagrangian experiment
May 30	1308	3:46	Bangor, ME	
May 31	1231 1926	3:42 3:20	Bangor, ME Nashua, NH	Single-day Lagrangian Experiment
June 8	1149 1847	4:21 3:38	Bangor, ME Laconia, NH	Single-day Lagrangian Experiment
June 10	1228 1457 1955	1:38 3:16 3:23	Bangor, ME Trois Rivieres, QC La Grande Riviere, QC	Multi-day Lagrangian Experiment
June 11	1349 1922	3:36 3:19	Bangor, ME	
June 13	1358 1818	2:54 3:23	Bangor, ME Niagara Falls, NY Rhineland, WI	Transit
June 14	1408 1838	2:28 2:38	Rhineland, WI Huron, SD Laramie, WY	
Second Deployment				
July 14	1750 2056	2:29 2:22	Laramie, WY Watertown, SD Rhineland, WI	Transit FTS Intercomparison DC-8 Intercomparison
July 15	1348 1839	3:37 3:12	Rhineland, WI Niagara Falls, NY Bangor, ME	
July 17	1159 1830	3:50 3:52	Bangor, ME Quebec City, QC	Multi-day Lagrangian experiment
July 18	1220	3:27	Bangor, ME	
July 21	1140 1818	4:18 3:42	Bangor, ME Nashua, NH	Single-day Lagrangian experiment
July 22	1318 1913	4:33 3:52	Bangor, ME	Single-day Lagrangian experiment

July 25	1148 1814	3:55 3:48	Bangor, ME Montreal, QC	Multi-day Lagrangian experiment
July 26	1214	4:36	Bangor, ME	
July 30	1238 1853	3:11 2:30	Bangor, ME	Single-day Lagrangian experiment
August 4	1200 1835	4:17 3:17	Bangor, ME Quebec City, QC	Multi-day Lagrangian experiment
August 5	1159	3:56	Bangor, ME	
August 8	1213 1421 1825	1:06 4:26 2:29	Bangor, ME Montreal, QC Rouyn, QC	Multi-day Lagrangian experiment
August 9	1207 1738	3:37 3:17	Bangor, ME	
August 14	1258 1719	1:52 4:16	Bangor, ME Niagara Falls, NY Rhineland, WI	Transit FTS intercomparison
August 15	1334 1953	3:11 2:24	Rhineland, WI	Regional Flights near WLEF
August 16	1326 1752	2:33 2:00	Rhineland, WI Huron, SD Laramie, WY	

A final component of the overall COBRA-Maine mission strategy was to coordinate wherever possible with other surface or airborne investigations occurring in the vicinity. If the primary flight objectives could be met, every effort was made to coordinate flybys of additional surface stations in the region. To this end, there was a loose skeleton of surface stations which the King Air regularly visited (Figure 2.4). These included the anchor points, Argyle tall tower, Howland and Harvard flux towers, as well as the NOAA GMD-ESRL WLEF tall tower in Wisconsin (45.95° N, 90.27° W), the Fluxnet Canada eastern old black spruce and black spruce/jack pine cutover sites in central Quebec (49.67° N, 74.43° W & 49.26° N, 74.03° W respectively) and the University of California Berkeley concentration station at Chebogue Point, near

Yarmouth, Nova Scotia (43.75° N, 66.12° W). The King Air also made multiple climbing and descending spirals around WLEF to compare to a new Fourier Transform Spectrometer total column CO₂ instrument deployed there by the California Institute of Technology (P. Wennberg). Finally, air-to-air comparisons were attempted with the NASA DC-8, operating on the Intercontinental Chemical Transport Experiment – North America (INTEX-NA) mission. Collaborator data have all been added to the COBRA-Maine database, creating an impressive dataset with multiple scales of measurements and great utility for observational and modeling studies.

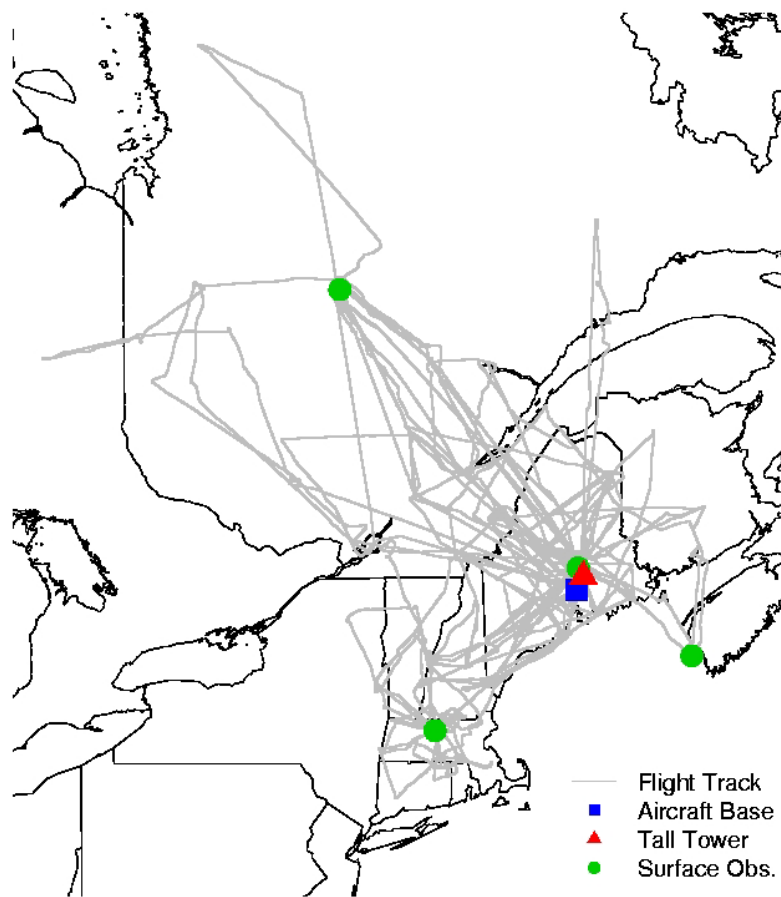


Figure 2.4 – COBRA-Maine regional flights and surface network

2.4 Flight Planning

2.4.1 General Flight Planning

Two guiding principles were used in planning individual flights for COBRA-Maine: 1) Work as much as possible within the air traffic control system, flying under instrument flight rules (IFR), where controllers could maintain positive radar contact with the King Air and could take responsibility for maintaining separation between it and others. 2) Within the scientific target region, maximize the number of vertical profiles from the surface to the lower free troposphere. As a general rule, COBRA-Maine flights avoided level-flight unless necessitated by the need to cover long horizontal distances or to conform to the requirements of air traffic control. Figure 2.5 shows a typical three-dimensional flight track consisting almost entirely of ascents and descents.

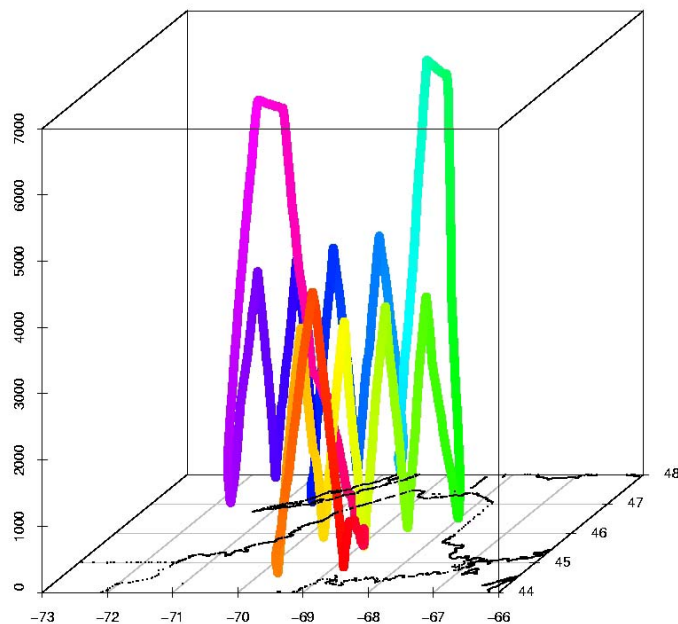


Figure 2.5 – Three dimensional depiction of the flight track from the morning flight on June 11th, 2004. The gradient of colors follows enroute time. The series of lower altitude climbs and descents are an example of sawtoothing.

Because radar coverage in most areas does not extend down to the surface, the most consistent way to simultaneously follow both these guidelines is to repeatedly utilize a flight exercise familiar to most pilots known as a “missed approach” (Figure 2.6). During a missed approach, air traffic control coordinates with an aircraft to follow published navigation procedures for descent to an airport runway. Instead of landing, the aircraft overflies the runway and departs the airport following another published navigation procedure. If the runway is in sight, the pilot is allowed to descend as low as he or she deems reasonable above the runway, an altitude that ranged from 3 to 15 meters during COBRA-Maine operations. For maximum efficiency, the King Air would keep its landing gear up and maintain a forward velocity around 275 km/hr. Low fly-bys at Argyle and Howland required the pilots to plan well ahead of the mission, obtain special permission from the FAA to waive the standard ground and obstacle clearance flight rules, and brief the air traffic controllers at Bangor in advance of operations. Once the Bangor controllers became accustomed to the standard COBRA-Maine inbound and outbound flight paths, they readily granted leeway for maneuvering.



Figure 2.6 – A typical missed approach at a small airport in northern Maine. The King Air was moving about 280 km per hour with landing gear up as this photo was taken.

Designing around missed approaches translates flight planning into an exercise of finding a series of airports in the scientific target region between which the aircraft can ascend and descend, with anywhere from 3 to 12 missed approaches in between takeoff and landing. To facilitate planning, an airport database was developed that could directly interface with the meteorological and air mass trajectory forecasting analyses described below. The northeast U.S. is generally dense with airports, but not all airports have published approach navigation procedures, and airports become far sparser in Quebec north of the Saint Lawrence River. Additionally, flights in a limited geographic area often could benefit from added vertical profiles between missed approaches. For these situations, the University of Wyoming crew and Harvard science team agreed upon a procedure dubbed “sawtoothing,” whereby enroute between airports the pilot would descend to ~200 m above the surface, as allowed by FAA regulations, then ascend to ~4 km above the surface and immediately begin another descent (Figure 2.5). The pilot worked with air traffic control on a case by case basis, sometimes getting a block altitude

clearance and sometimes reverting to visual flight rules (VFR), with radar-based air traffic advisories (rather than positive separation) from air traffic control. VFR operations were temporary whenever possible, but occasionally extended the duration of flight as dictated by air traffic control.

Most takeoffs were scheduled two to three hours after sunrise. In order to allow the University of Wyoming crew to readily fuel the aircraft, enter waypoints (i.e. airports for missed approaches) into King Air navigation systems, and coordinate as needed with customs and air traffic control, Harvard flight planners would deliver the flight plan the evening before takeoff. Once in flight, the goal was deviate from the pre-determined flight plan as little as possible. Unlike many other applications of aircraft in atmospheric research such as icing or convection studies, the scientific goals of COBRA-Maine require neither “chasing” any weather, nor interpreting any real time data. However, one advantage of the University of Wyoming King Air is the capability of the data system and experience of the crew to operate within a real-time decision-making environment, even if it was not utilized in COBRA-Maine. Early in mission, the University of Wyoming pilots quickly established a routine of a regularly seeking input from the Harvard onboard scientist on most real-time decisions, which marked a substantial increase in inflight communication and scientific input from the previous COBRA campaigns. Most real-time decisions involved working with air traffic control restrictions to the original flight plan, but they occasionally became more significant. Examples included eliminating a set of descents and deviating due to severe mesoscale storms in the area, deciding to continue a flight when the pilot’s onboard communication system failed

(relying instead on the onboard scientist's radio skills), and deciding to discontinue a flight when the University of Wyoming data system failed.

2.4.2 Transit flights

Each of the two deployments began and ended at the King Air's primary base in Laramie, WY, allowing for a total of four transits back and forth between Laramie and Bangor. Following the successful model employed in COBRA-2003, transit flights were designed to balance obtaining reasonable vertical sampling, while covering as much horizontal distance as possible, generally with two or three missed approaches on each leg. Each one-way transit consisted of four flights, with similar waypoints for missed approaches, fuel stops and an overnight in Rhineland, WI (Figure 2.7). Rhineland was chosen for its aircraft facilities and proximity to WLEF, another NOAA GMD-ESRL tall tower with instrumentation up to 396m. Focusing transit flights around fly-bys at WLEF allowed for a series of opportunistic intercomparisons in addition to the tall tower itself. Most successfully, COBRA-Maine data has been used in conjunction with NASA DC-8 in situ CO₂ data obtained during INTEX-NA, to validate surface based Fourier Transform Spectrometer measurements of total column CO₂ density (Washenfeller et al., 2006).



Figure 2.7 – COBRA-Maine transit flight tracks

The King Air and DC-8 performed concentric spirals (King-Air with 2.5 km radius; DC-8 with 8 km radius) around the WLEF tower, where the FTS was based. The CO₂ instrument onboard the DC-8 has a similar detector (Licor 6252) to the Harvard instrument (Licor 6251) and both frequently calibrate in-flight to standards traceable to the WMO Central CO₂ Laboratory or NOAA ESRL (Vay et al., 2003; Daube et al., 2002). Direct comparison between the Harvard CO₂ instrument and the DC-8 based instrument illustrates the difficulty of successfully comparing two airborne instruments on two separate platforms, even under near optimal conditions with a very favorable flight protocol (Figure 2.8). Although each instrument observes a similar general atmospheric structure for CO₂, the horizontal variations in the middle troposphere have strong gradients that confound quantitative comparison of the vertical profiles. Washenfelder et al. (2006) circumvented this problem by relying on column integrals from both datasets averaged over the 45-minutes of spiraling.

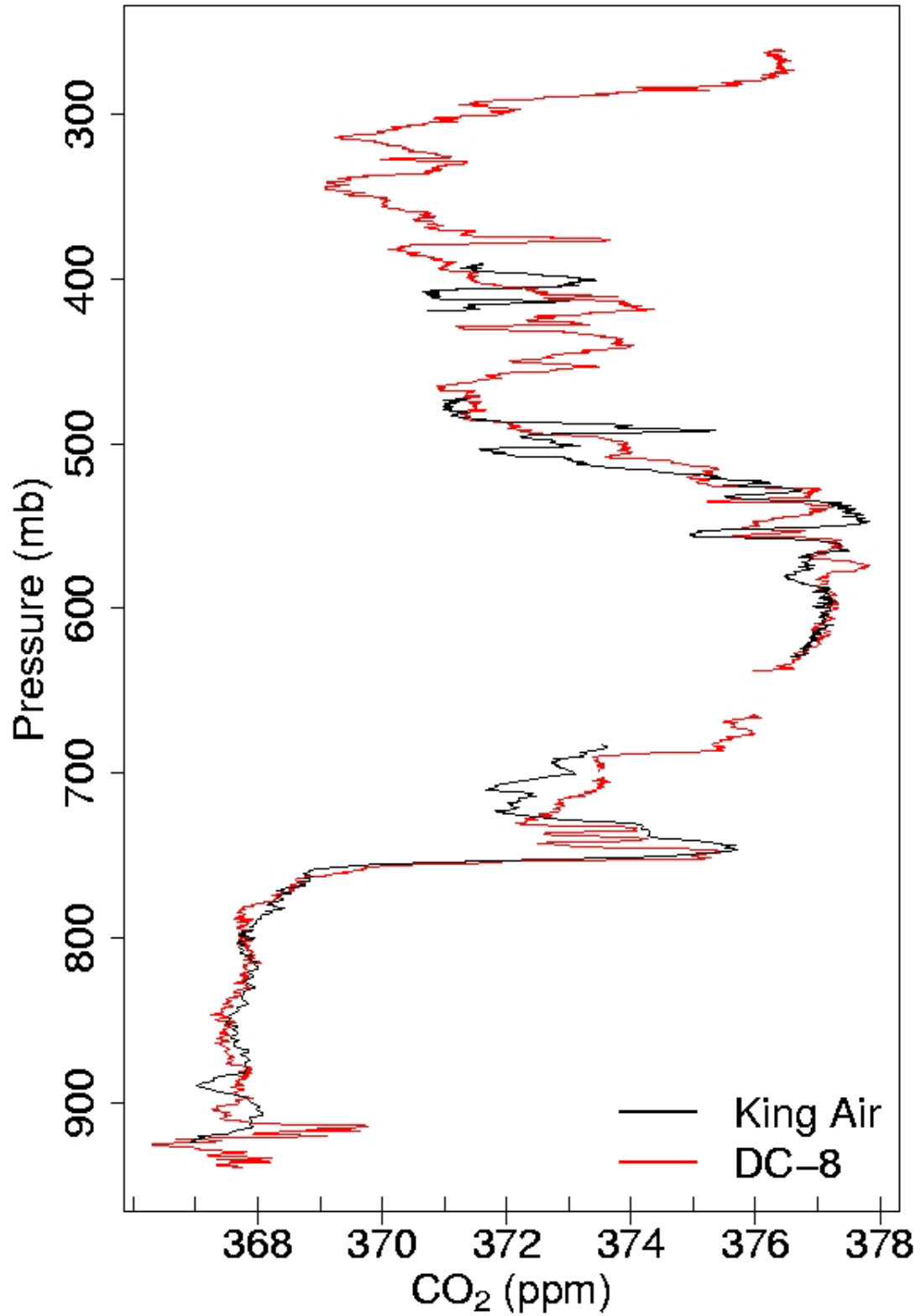


Figure 2.8 – Overlaid CO₂ profiles from the King Air and NASA DC-8 from concentric spirals flown over WLEF tower on July 15th, 2004.

On the final set of transit flights, an additional day was spent in Wisconsin, doing two flights around a set of 5 short towers (~20 m), all about 100 km from WLEF and set up by researchers at Penn State University to form a loose “ring” around the central tower. The goal of such a ring is to have a continuous set of experiments capturing changes in the CO₂ concentration as airmasses move from the perimeter ring towards the central tower and vice versa and are modified by surface fluxes from the interior landscape. A case study utilizing high density flight data should support analyses of this type, but as yet data from those flights have yet to be compared to ring surface observations.

2.4.3 Lagrangian experiments

The bulk of flight planning in COBRA-Maine centered on designing individual Lagrangian experiments in the mode of Lin et al. (2004). The overall goal of these experiments was to fly horizontal and vertical cross-sections through an airmass prior to its arrival over a target region of surface influence, then measure it again after as it reached a designated receptor point downstream of the surface region being studied. Thus, as designated by Lin et al. (2004), these flights constitute “influence-following” Lagrangian experiments, rather than airmass-following experiments, reflecting the fact that air parcels disperse rapidly in the boundary layer. In practice, COBRA-Maine influence following experiments only flew when there was an expectation the airmass moving over the source region would remain reasonably contiguous.

The general strategy for planning a single Lagrangian experiment involves picking a receptor point, usually associated with a surface flux tower or concentration

measurement, and using an ensemble approach to forecast the source region for air arriving at the receptor point at a designated receptor time. During COBRA-Maine, this process would begin three to four days before the first flight of any anticipated experiment. In the early planning phase, flight planners would begin an assessment of the overall synoptic situation through readily available online products (e.g. National Weather Service forecasts) and through custom “outlook” E-mail and phone briefings from Meridian Environmental Corporation of Grand Forks, ND (<http://web.meridian-enviro.com/>), a company contracted to provide operational forecasts for COBRA-Maine. If the synoptic situation looked favorable, with conditions fair enough for flight and an upstream fetch mostly over non-urban terrestrial areas, then a receptor point would be chosen based on the expected wind direction and upstream source region. In many cases for COBRA-Maine, it was the experience and judgment of the flight planner which determined the most appropriate receptor location.

There were usually two alternatives for receptor time: 1) in the morning around 1300 GMT (0900 EDT), with two upstream flights targeting the airmass ~22 hours upstream and ~16 hours upstream of when it would arrive at the receptor or 2) in the afternoon around 2000 GMT (1600 EDT), with one upstream flight targeting the airmass 6 to 8 hours upstream of arrival at the receptor. Situation 1 would require two days of flying. The first day would involve a relative long transit to the area of upstream influence, with as much up-and-down profiling as possible before refueling, followed by a couple hours on the ground and a return to base with enroute profiling. It is conceivable to overnight the airplane away from base in order to either expand the geographic characterization of the upstream airmass or sample it far more extensively, but the

logistical challenges were enough of a barrier in COBRA-Maine that this was never attempted. The second day of flying would involve a morning flight in and around the vicinity of the receptor point to fully characterize the airmass in the area of the receptor point at the receptor time and if fortunate, sample any residual layer that might contain a measurable signal of uptake from the day prior to the receptor time. Situation 2 would require one day of flying with two flights: a morning flight to the area of upstream influence, followed by a two- to three- hour lunch/refueling stop, and a second flight in the area of the receptor point. If the conditions were particularly favorable, situation 1 (morning receptor; 24-hour Lagrangian experiment) and situation 2 (afternoon receptor, 8-hour Lagrangian experiment) could be combined into a multi-flight series with multiple embedded experiments. This is the situation discussed below in the planning case study presented for the June 10th – 11th, 2004 flights.

Once an appropriate receptor was determined, the STILT model was then run in time-reversed forecast mode using coarser meteorological driver models (e.g. GFS-180 km, ETA-40km, MM5-45 km) from the chosen receptor point and time to predict the associated upstream source region location. Thus, particles would run backwards from the receptor location and time, which was usually 3 to 4 days in the future at this point of the flight planning cycle, using forecast winds. An artful ensemble approach, very analogous to operational weather forecasting methods, was then applied to determine the most appropriate influence region. Flight planners were looking for STILT ensemble forecasts to demonstrate good model agreement and a relatively coherent upstream influence region for the receptor point.

The flight planning process then became an iterative process through the morning and afternoons leading up to a potential Lagrangian experiment. Synoptic briefings from Meridian Environmental Technology became more and more and targeted on the specific region of potential flight and more detailed with regards to the extent and heights of cloud cover, any sort of convective potential, wind shear, and flight hazards. New STILT runs were begun automatically as each major forecast product became available on its usual 6, 8, or 12 hour cycle. Higher resolution mesoscale forecasts (ETA-12 km, MM5-15km) were also added to the ensemble as they became available closer to the receptor time.

By the day before flights in any given Lagrangian experiment needed to begin, two days prior to receptor time in a 24-hour experiment or one day prior to receptor time in an 8-hour experiment, flight planners could reasonably use experience and judgment to make a decision of whether a series of flights could constitute a viable Lagrangian experiment. If the decision was made to proceed, the final part of the planning cycle would begin in earnest. The latest STILT ensemble forecast would be combined with any operational limitations to determine the precise receptor time to the hour and the associated upstream locations to fly. Flight planning software would be employed to determine the first and second principal axes of the STILT ensemble upstream source region and the nearest airports in the database available for missed approaches. A logical flight sequence of missed approaches, with sawtoothing as needed, was developed to most efficiently fly the forecast upstream source and downstream receptor regions. Any flightspace restrictions, such as active Military Operations Areas or restricted areas, were included at this point and flightpaths altered as needed.

The last phase of the flight planning cycle involved communicating the plans to the pilot, who had final say on operational viability of any plans, on the afternoon or evening before the initial flight of a given experiment. Communication involved detailing a written set of waypoints and instructions for missed approaches and/or sawtoothing, along with estimated time and duration of each leg. During COBRA-Maine, the University of Wyoming pilots would sometimes request minor alternations, call to make sure fuel, ground power, or customs officers would be available if needed, and alert air traffic control facilities to mission activities. Once the pilots agreed, flight plans were rarely altered, and inflight deviations were only expected for unforeseen air traffic control difficulties, poor weather, or instrument failure. COBRA-Maine flight planners were normally working two to three potential Lagrangian experiments simultaneously, each at a different point in the flight planning cycle.

The flights of June 10th and 11th, 2004 provide an illustrative example of two overlapping Lagrangian experiments that were successfully planned and executed with a series of five individual flights. The planning cycle for these experiments began on June 7th, just as the planning cycle for another set of flights was nearing completion. Meridian briefings and National Weather Service forecasts indicated a relatively strong, fast moving cold front would move through Maine on the evening of June 9th. Behind the cold front would be post-frontal conditions of fair weather and strong flow from the northwest. This presented the opportunity for a 22-hour Lagrangian experiment, with a receptor point at Howland Forest on the morning of June 11th at 1300 GMT (0900 EDT). That meant upstream flights would need to occur over central Quebec on June 10th.

Model Compare: HOWLAND 061113

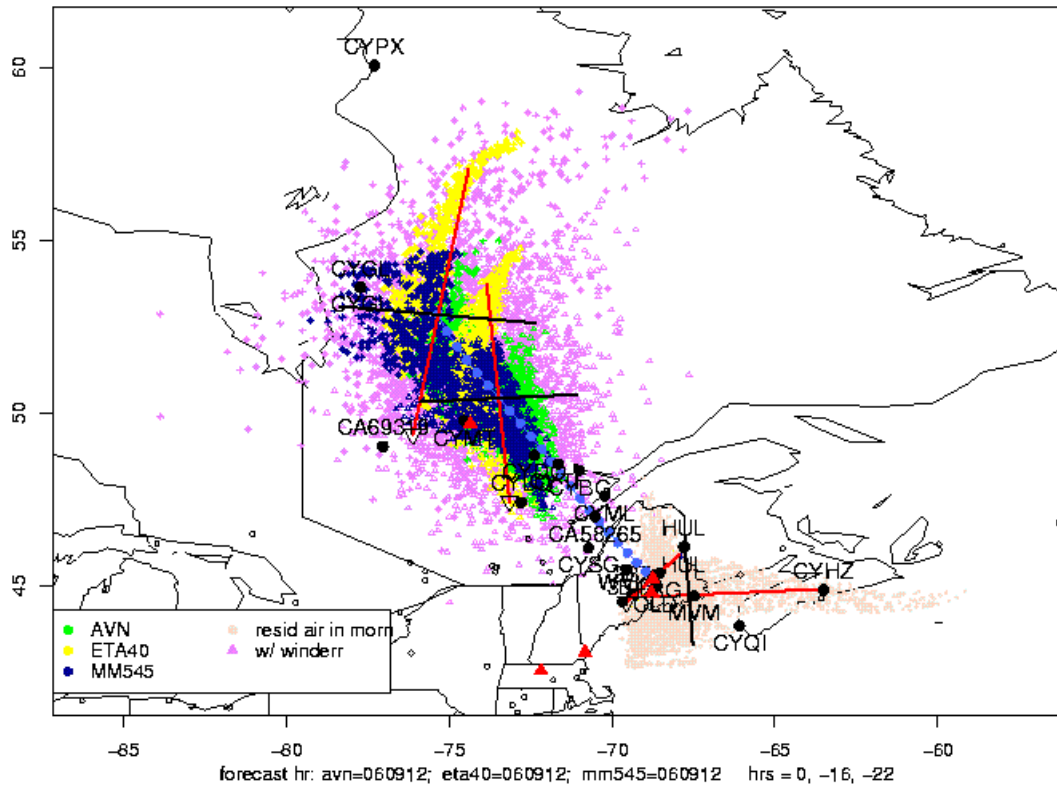


Figure 2.9 – The STILT derived ensemble forecast flight planning product used to design the Lagrangian flights of June 10th, 2004. The receptor point is Howland Forest on the morning of June 11th. This plot is based on forecasts run at 1200 GMT on June 9th. Results for three different meteorological drivers are shown with green, yellow, and dark blue circles; each driver produces a set of air parcel locations at 16 and 22 hours back in time. Light blue dots indicate the central location of the ensemble airmass at each hour back in time from the receptor point. Red and black lines indicate the first and second principal axes respectively of the ellipsoid region containing the ensemble of parcel locations at specified times (0, -16, and -22 hours here). Dark pink triangles give a visual indication of errors in the wind field propagated through the STILT model (Lin et. al, 2004). Light pink circles indicate the potential location of the residual layer on the morning of June 11th. Black points labeled with identifiers indicate potential airports for missed approaches. Red triangles indicate surface CO₂ flux or concentration observation sites. Unlabeled small black open circles denote the location of urban areas with populations in excess of 50,000 people.

Because the winds were forecast to be relatively fast, the upstream source region at the time the aircraft would need to fly (~1500 GMT July 10th; 22 hours upstream of the

receptor) was near James Bay, the southern extension of Hudson Bay, at the limit of the single-day range for the King Air and nearing pilot duty limitations. STILT runs demonstrated very good agreement among models and the source region fit directly into the mission strategy (Figure 2.9).

As the planning cycle continued over June 8th and June 9th, the forecasted post-frontal conditions seemed ideal for Lagrangian experiments, so planners decided to include a second, embedded one-day Lagrangian experiment for June 11th. Thus, the planned flight around the receptor point on the morning of June 11th would serve two purposes—a downstream receptor flight for the upstream flights of June 10th and an additional upstream flight itself for a later flight to occur downstream on the afternoon of June 11th. The two-flights with takeoffs and landings at Bangor on June 11th would represent a self-contained 6-hour Lagrangian experiment with a source range over northern and central Maine (Figure 2.10).

Three flights were planned for June 10th based on the final STILT ensemble calculated from forecasts produced on the morning June 9th. Because customs facilities in Canada are clustered in the southern part of the country, planners chose to utilize a three-flight strategy to sample the far upstream air mass for the 22-hour experiment. The first flight would be a transit with no vertical profiling to Trois-Rivières, Quebec, finishing with a “quick turn” to pass through customs and refuel with the shortest possible time on the ground between the first and second flights. The second flight would then proceed to the target region, with two missed approaches enroute and as much sawtoothing as possible in the region the STILT forecast to have influence 22-hours upstream of the Howland receptor point. Airport options are limited that far north, so lunch and a second

refueling were to be done at La Grande Rivière, the northernmost point of the entire mission. Pilot duty limitations limited ground time to 2 hours, and the third flight was planned directly to Bangor, with two missed approaches and sawtoothing in the vicinity of the Eastern Old Black Spruce (EOBS) flux tower, part of Fluxnet Canada.

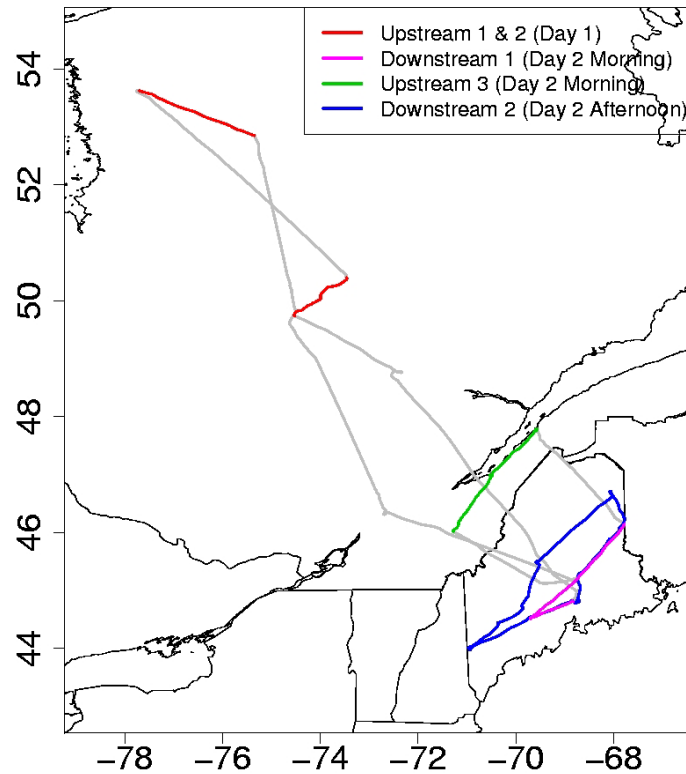


Figure 2.10a – Flight tracks for June 10th – 11th Lagrangian experiment, with legs designed to sample upstream and downstream across the northwest flow colored. Note the correspondence between the flight tracks and the forecast products shown in Figures 2.9 and 2.11.

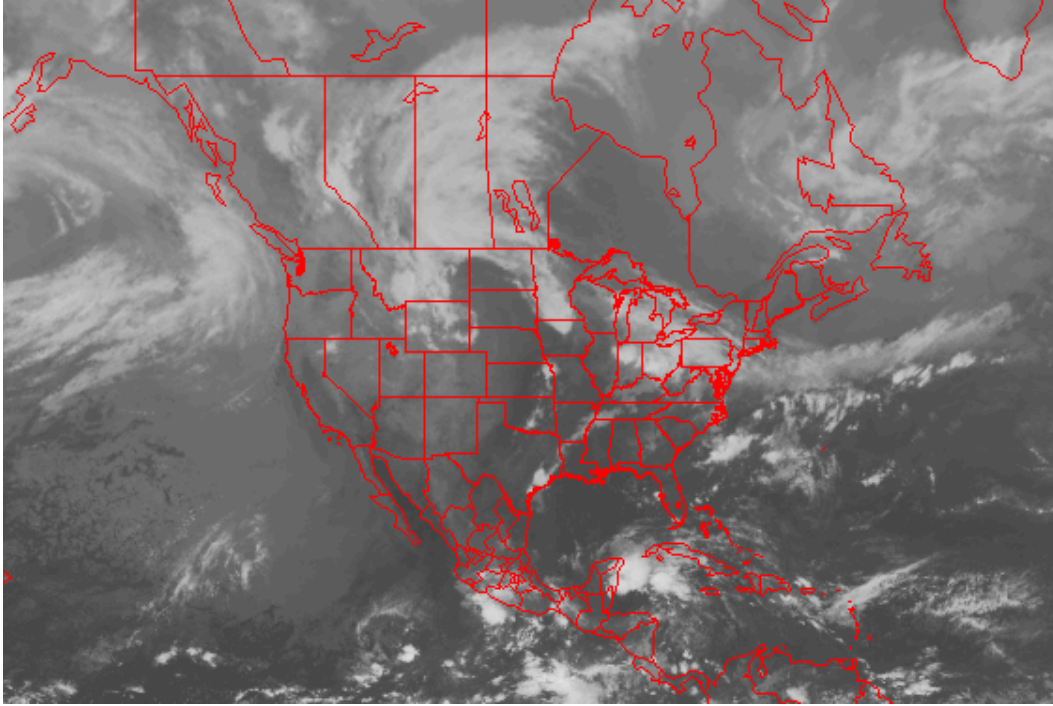


Figure 2.10b: Composite GOES infrared satellite image from 1145 GMT on June 11th, 2004. A cold front extends eastward from Pennsylvania into the Atlantic. Behind the front, there are fair skies and strong northwest flow bringing air across central Quebec into Maine. Image archived by Unisys Weather Corporation (<http://weather.unisys.com/archive/index.html>)

As the King Air was operating over central Quebec on June 10th, planners back in Bangor finalized the plans for two flights on June 11th based on ensemble forecasts produced on the morning of June 10th (Figure 2.11). The morning flight was planned to sample the downstream part of the 22-hour experiment by doing a broad cross-section and a fly-by of Howland, then proceed northwest (upstream) to make a series of missed approaches along the southern bank of the Saint Lawrence river which would sample the upstream air of the 6-hour experiment. Because the horizontal extent of the both the June 11th morning and afternoon flights was far more local to Bangor than the June 10th flights, as much vertical profiling as possible was planned. The afternoon flight would simply

trace broad swath of air perpendicular to the forecast flow (i.e. fly along a southwest to northeast path, perpendicular to flow from the northwest) and maximize vertical profiling, with multiple fly-bys of Howland and Argyle towers. The June 11th flights completed a series of five total flights and two overlapping Lagrangian experiments with multiple timescales.

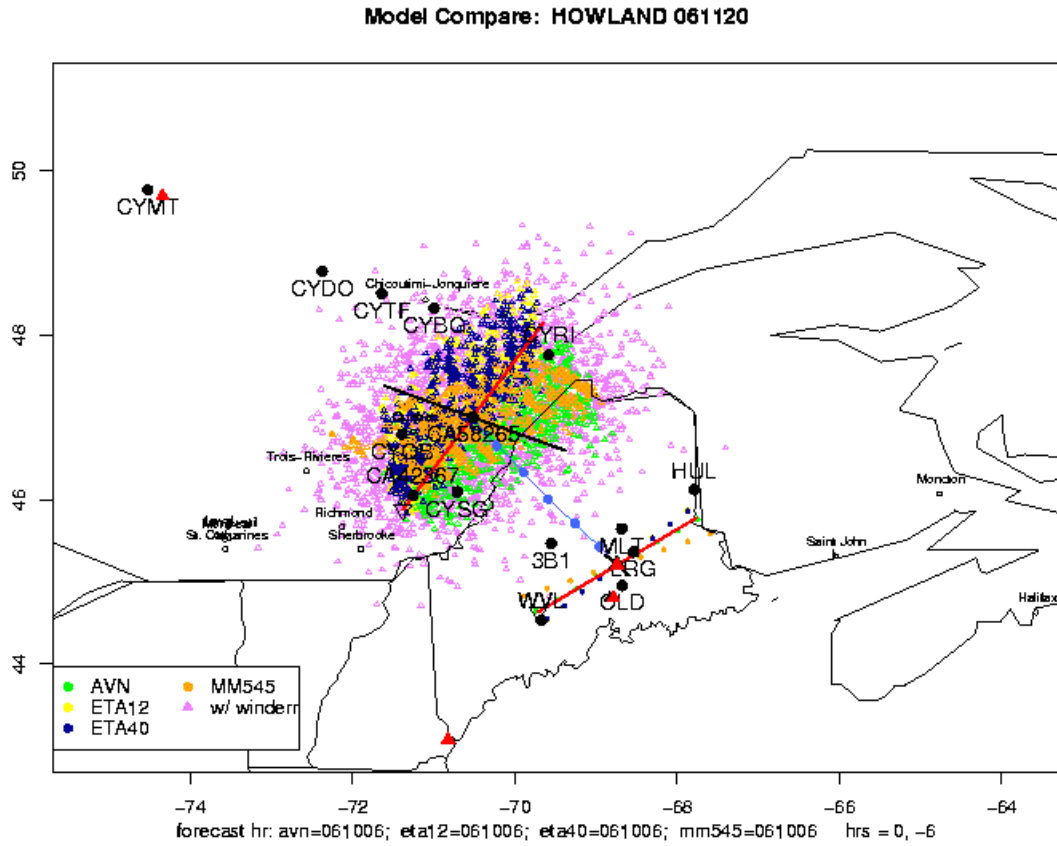


Figure 2.11 – The STILT derived ensemble forecast flight planning product used to design the Lagrangian flights of June 11th, 2004. The receptor is Howland forest on the afternoon of June 11th and four meteorological drivers are shown. See caption of Figure 2.9b for explanation of colors, symbols and lines. Since this product was used to plan an afternoon flight, a residual layer prediction was not made

2.5 Weather and climate during COBRA-Maine

General circulation brings variable weather to Maine and Quebec during a typical summer, with prevailing winds from the southwest. The prevailing flow is punctuated by passing mid-latitude cyclonic systems and that often bring postfrontal fair weather, cool air, and northwest winds with a long fetch over southern and central Quebec and Hudson Bay. Post-frontal conditions afforded excellent flying weather and are over-represented in the COBRA-Maine dataset. In addition to west-to-east moving cyclonic systems, occasionally low pressure systems move northeast along the U.S. eastern seaboard, lesser spring/summer analogues to powerful winter “Nor’easters”, which can bring east-northeast flow to central Maine and variable conditions to southern Quebec. The associated unsettled, stormy weather is challenging to forecast and difficult to model, making it a straightforward decision to not fly during days affected by such systems.

Statistics from the Northeast Regional Climate Center

(<http://www.nrcc.cornell.edu/climate/>) show that June-August 2004 was generally cool and wet in Maine, with a mean temperature of 16.8° C (0.83° C below the mean for 1971-2000) and multi-station mean accumulated precipitation of 32.66 cm (4.42 cm above the mean for 1971-2000). For the 110 years between 1895 and 2004, summer 2004 in Maine fell into the 15th percentile for temperature and 84th percentile for precipitation, but overall it was not necessarily cool and wet at the same time. A month-by-month analysis of the COBRA-Maine period (Table 2.3) shows Maine first had cool temperatures with normal precipitation in June, a slightly cool and slightly wet transitional month in July, then normal temperatures with high precipitation in August. The overall combination of

cool and wet conditions caused central Maine to have more days than usual of low hanging stratus and light showery weather.

Table 2.3 Northeast Regional Climate Center summer 2004 climate statistics for the state of Maine

	Mean Temp(°C)	Temp departure from 30-year mean (°C)	Temp 110 year Percentile	Mean Precip (cm)	Precip departure from 30-year mean (cm)	Precip 110-year Percentile
May	10.9	0.2	57	9.40	0.15	57
June	14.2	-1.8	6	6.83	-2.74	25
July	18.1	-0.8	19	11.10	1.60	81
August	18.0	0.2	55	14.73	5.56	93

Maine’s coastal location meant that COBRA-Maine sometimes flew in areas where the atmosphere took on a marine character. Only two flights went directly across the Gulf of Maine to or from Nova Scotia, but a number more involved missed approaches at coastal airports. Ocean temperatures in the Gulf of Maine followed a typical New England summer pattern, remaining quite cold at the beginning of May, and gradually increasing over May and June to summer norms (Figure 2.12). The comparatively cold water temperatures led to some strong marine inversions during May and June, an example of which is discussed below.

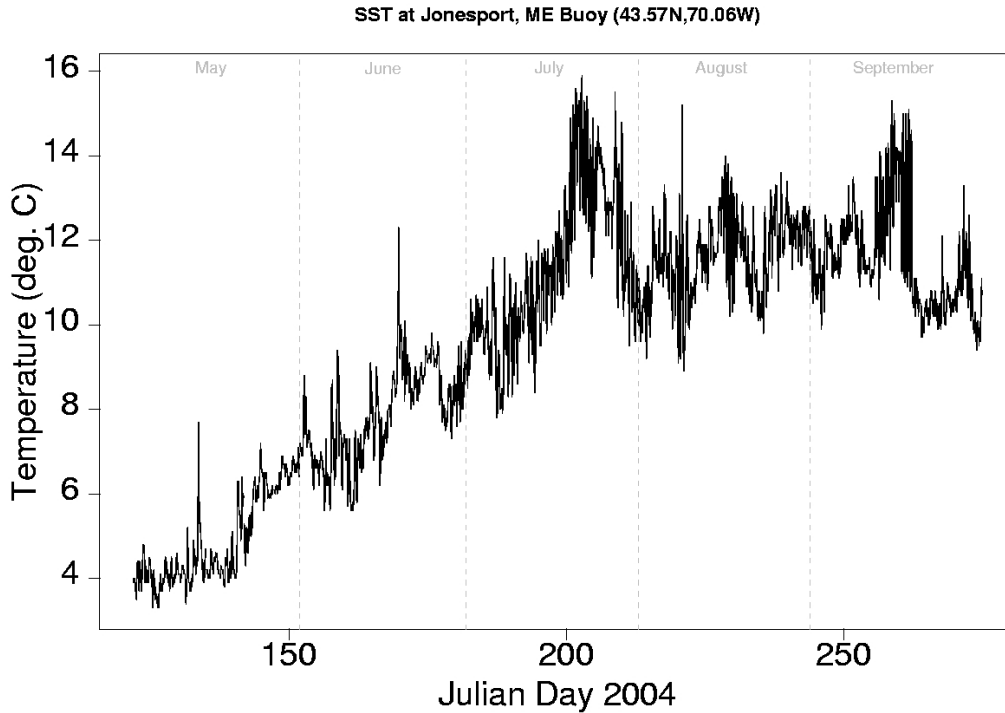


Figure 2.12 – Sea surface temperature measured at Jonesport, ME Buoy, offshore of Bar Harbor, during COBRA-Maine. Data courtesy of the NOAA National Buoy Data Center (<http://www.ndbc.noaa.gov/>)

Convective storms did not play a prominent role in COBRA-Maine, because every effort was made to avoid flying in stormy situations. By design, the aircraft flew almost entirely in high pressure interludes between passing mid-latitude cyclones. However, Maine weather was greatly influenced in early August by a tropical storm that passed directly offshore. Hurricane Alex affected the U.S. East Coast from August 1st to August 6th, 2004, making landfall in North Carolina on August 2nd, before moving north-northeast along a track few hundred kilometers offshore. Alex was unique in that it actually strengthened as it moved northward into the midlatitudes, reaching category 3 as it moved through 40° N and did not dissipate until reaching nearly 50° N in the middle of the North Atlantic (Figure 2.13). Although the eye of Alex was well offshore, a high resolution MODIS snapshot from August 4th, 2004 (Figure 2.14) shows how Alex

affected the east coast. As is the case with most hurricanes, diverging air aloft at the center and associated subsidence away from the center produced anti-cyclonic (clockwise) flow a few hundred kilometers from the eye of Alex. This translated into clear skies and comparatively moderate flows almost directly from the west over central Maine on August 3rd, 4th and 5th, 2004.

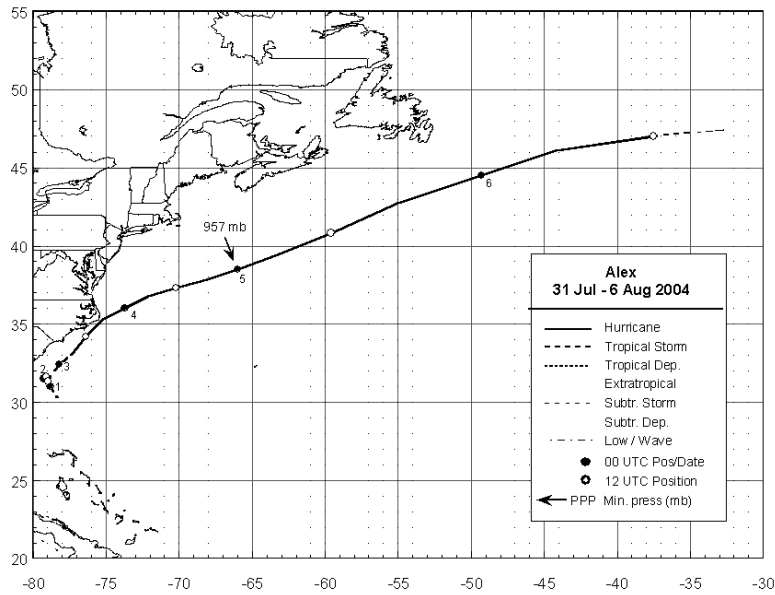


Figure 2.13 – Plot of the track of Hurricane Alex produced by the NOAA National Hurricane Center (<http://www.nhc.noaa.gov/2004alex.shtml>)

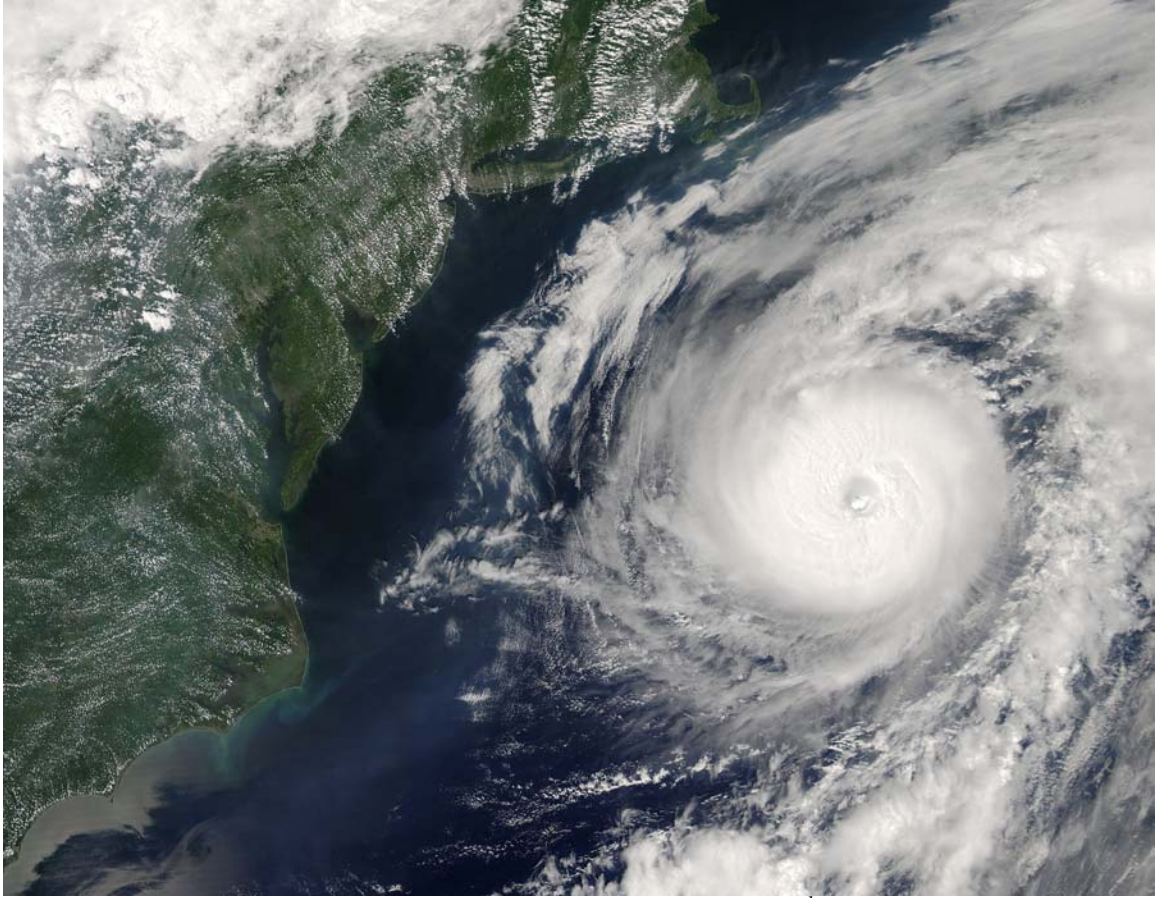


Figure 2.14 – MODIS image of Hurricane Alex from August 4th, 2004. The U.S. coastline stretching from South Carolina to Massachusetts can be discerned on the left. Subsidence a few hundred kilometers from the center of the storm brought fair weather and westerly flow to the U.S. east coast, but much of the air the middle atmosphere originated in the subtropical Atlantic.

Taking advantage of this circumstance, the King Air flew a two-day Lagrangian experiment with a receptor point at Chebogue Point, near Yarmouth, Nova Scotia, where the University of California Berkeley had set up a concentration measurement station in association with International Consortium for Atmospheric Research on Transport and Transformation (ICARTT) 2004 field operations. Unfortunately, the measurement station was temporarily shutdown during the COBRA-Maine flights of August 4th and 5th as a precaution in case Alex made landfall in Nova Scotia. More importantly, standard forecast and reanalysis products would be expected to have a very difficult time modeling

synoptic flows associated with a hurricane traversing the eastern edge of the North American domain. This challenge is compounded by the approach of an independent midlatitude cyclone from the west on August 5th. Since these standard products are used to drive the STILT model, the influence functions calculated during this period are subject to an additional, difficult to quantify uncertainty not normally present. Attempts to model CO₂ exchange in Maine during these days also need to be approached cautiously because although flow is from the west, the background air entering Maine during this time was clearly of tropical or subtropical Atlantic origin, representing a relatively rare situation. Indeed, the domains of the mesoscale products do not include the location of Alex during this time.

2.6 Makeup of COBRA-Maine observations available for model use

COBRA-Maine airborne data can be used for surface and satellite instrument validation (Washenfelder et. al., 2006; Emmons et al., 2006 respectively), but was collected primarily to be combined with regional tower data in models. A survey of the observations reveal the rich texture of information the airborne data can provide to model studies, as well demonstrate various ways to examine the data. A good place to begin a data survey is with a control scenario with respect to surface exchange with the atmosphere. Figure 2.15 shows a horizontal CO₂ cross-section along the flight track from the test flight of May 12th, 2004 over central Wyoming. It shows two distinct layers of atmospheric CO₂ concentrations above and below ~1500 m above the ground and no evidence of any drawdown from surface vegetation. This was a very early season flight over high elevation (> 2000 m) sparsely vegetated terrain and occurred in part during a

late season snow squall. It is reasonable to conclude that the air surveyed on this flight has little to no influence from surface vegetation, marking it as a useful if uninteresting control case.

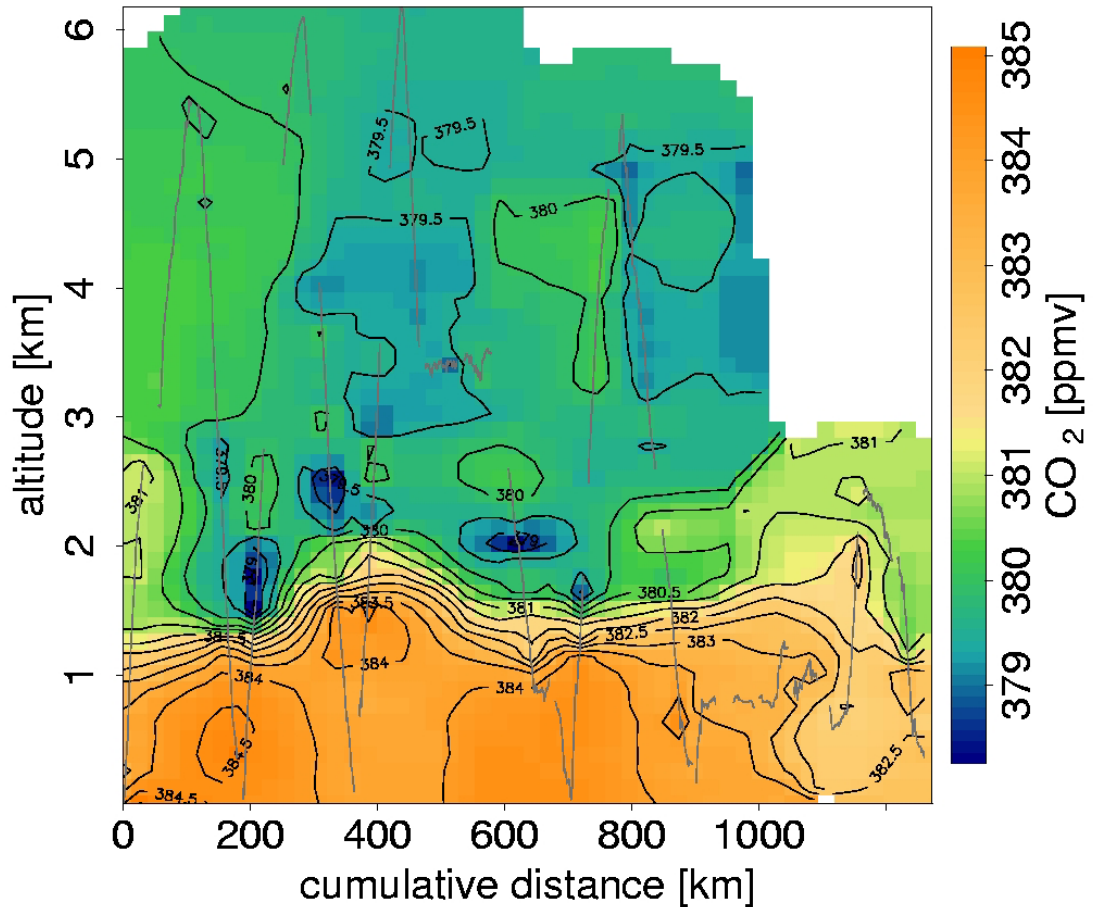


Figure 2.15 – Cross-section of CO_2 along the flight track from a test flight in central Wyoming on May 12th. There is very little surface vegetation influence on CO_2 concentrations making this a “control” scenario. On this and all the cross-sections that follow, the light gray lines indicate the flight track. Gaps in flight track indicate calibration periods of the CO_2 instrument.

Evidence of surface vegetation drawdown of atmospheric CO_2 is more readily discernable in other cross-sections and corresponds to data obtained from surface flux stations. Figures 2.17 and 2.18 show two latitude-altitude cross sections from mid-

afternoon flights traversing north to south from central Quebec to Bangor (Figure 2.16) on sunny days in early June and late July respectively. In the early June cross-section, there is very little evidence of surface activity in the far northern part of the cross-section, but noticeably reduced concentrations of CO₂ on the descent through central Maine. Figure 2.19 is a photograph which confirms that the northern edge of the cross-section, near James Bay, is snow-covered with very little biological activity. The late July cross-section shows a marked contrast to the early June cross-section in two respects. First, although there is still a north-south gradient in mid-afternoon CO₂ concentrations near the surface, it is not nearly as prominent as in early June, indicating the relative difference between surface vegetation uptake in central Quebec around 49° N and central Maine around 45° N is much smaller in late July than in early June. Second, the mid-afternoon surface drawdown is much greater in magnitude across the entire cross-section in late July than in early June.

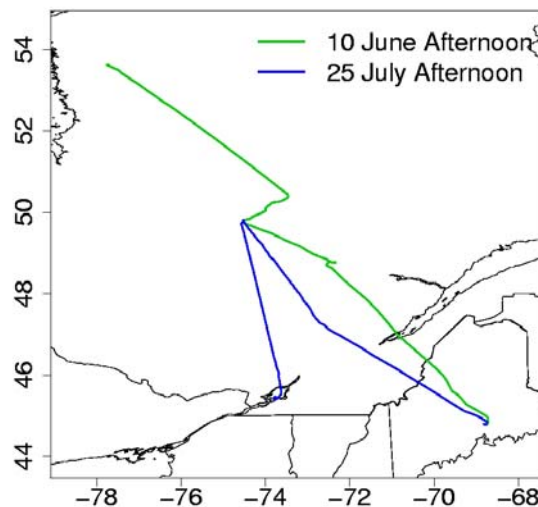


Figure 2.16 – Figure showing horizontal flight track corresponding to the cross-sections shown in Figures 2.17 and 2.18.

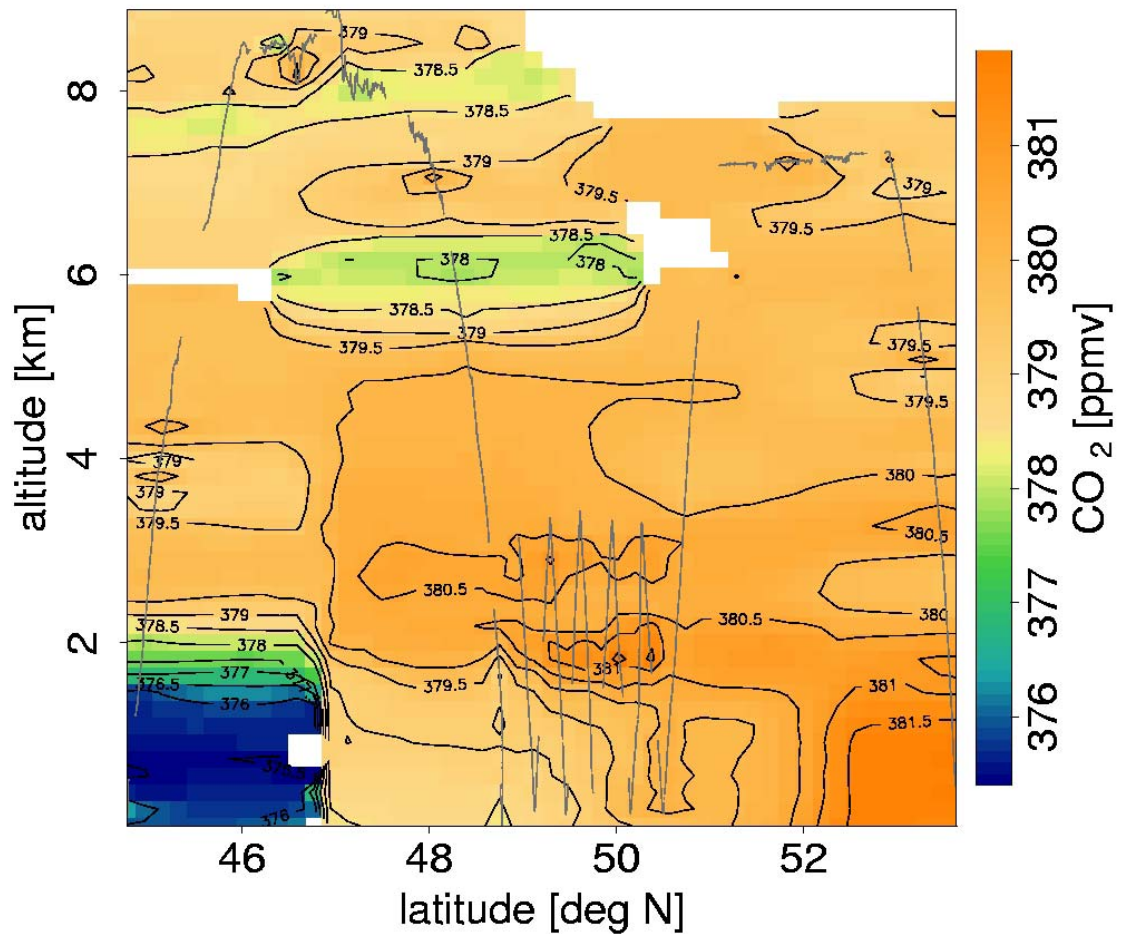


Figure 2.17 – Latitude altitude cross-section of the north to south afternoon flight on June 10th, 2004. There is very little vegetative uptake in the north and the telltale vertical gradient in the boundary layer indicating uptake in the south. The sharp horizontal gradient near the surface at 47° N is an artifact of interpolation. The aircraft was collecting data at in the free troposphere at that point.

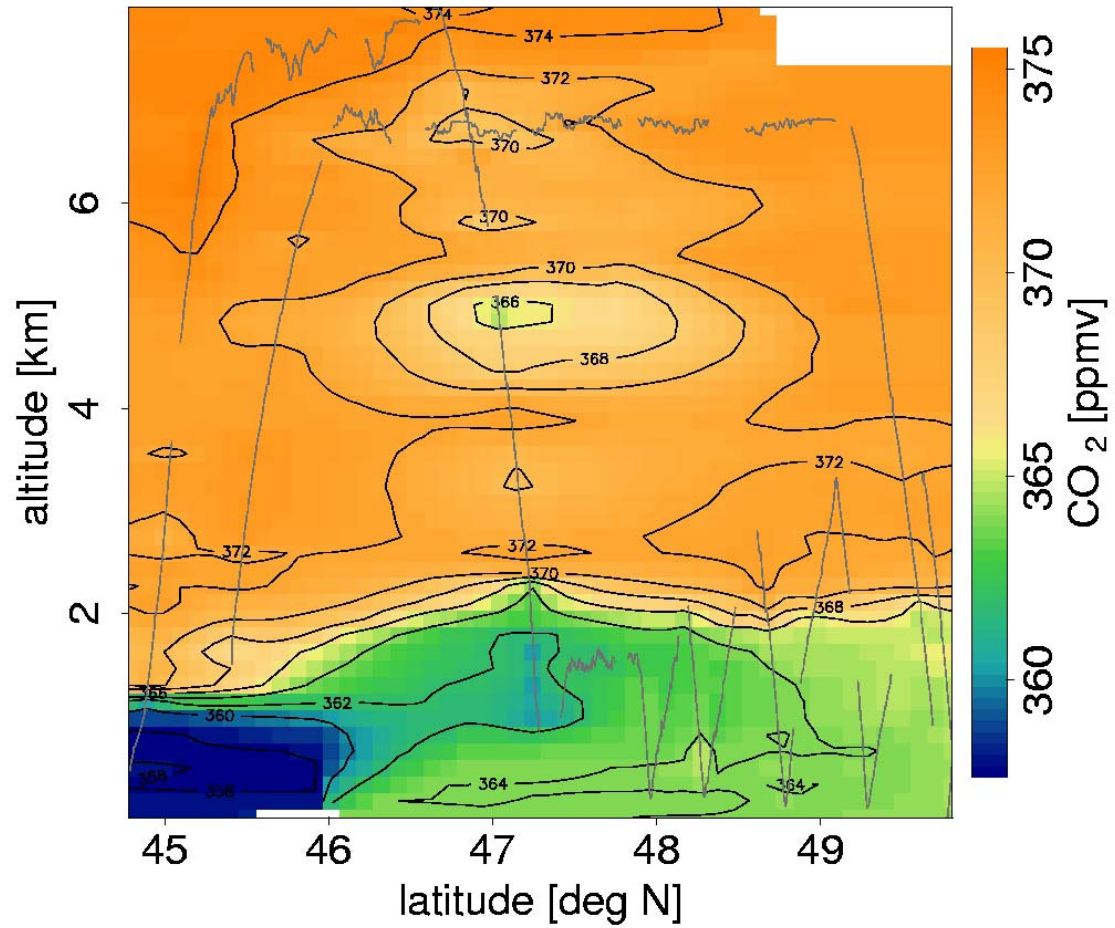


Figure 2.18 – Latitude altitude cross section from the afternoon flight on July 29th, providing a contrast to Figure 2.17. The northern latitudes now bear the signature of vegetative uptake and overall boundary layer CO₂ depletion is much stronger. There is also a north to south horizontal gradient in the boundary layer as well.



Figure 2.19 – Snow and ice covered landscape near La Grande Riviere, QC on July 10th, 2004. The waters of James Bay can be seen in the distance. It is assumed vegetation was dormant at this time and location.

Continuous surface flux data can provide a useful corroboration to the seasonal trends suggested by the snapshots seen in the airborne data. Figures 2.20 and 2.21 show the surface flux time series for three of the towers most regularly overflowed during COBRA-Maine: Fluxnet Canada Eastern Old Black Spruce (EOBS), Howland Forest, and Harvard Forest. The three towers lie along a north south gradient (49° N - 45° N - 42° N). The start of the growing season at each site in Figure 2.21 can be identified by the point when the magnitude of fluxes begins to increase, and growing season onset roughly follows latitudinal gradient —Harvard and Howland already reaching the growing season in early May, but EOBS lagging behind by a month. Fluxes at EOBS were still quite small in early June, consistent with the airborne observations. The differences in

magnitude among peak afternoon uptake values in Figure 2.20, Harvard taking up substantially more carbon than Howland and Howland taking up slightly more carbon than EOBS, imply a north-south gradient is expected in boundary layer concentrations across the region. If no air was moving, this gradient would be proportional to differences in fluxes. Most coupled surface-flux and atmospheric models should reasonably be able to capture the regional horizontal and local vertical afternoon boundary layer gradients observed in the airborne data, especially if they have been validated against flux tower data of the sort presented here.

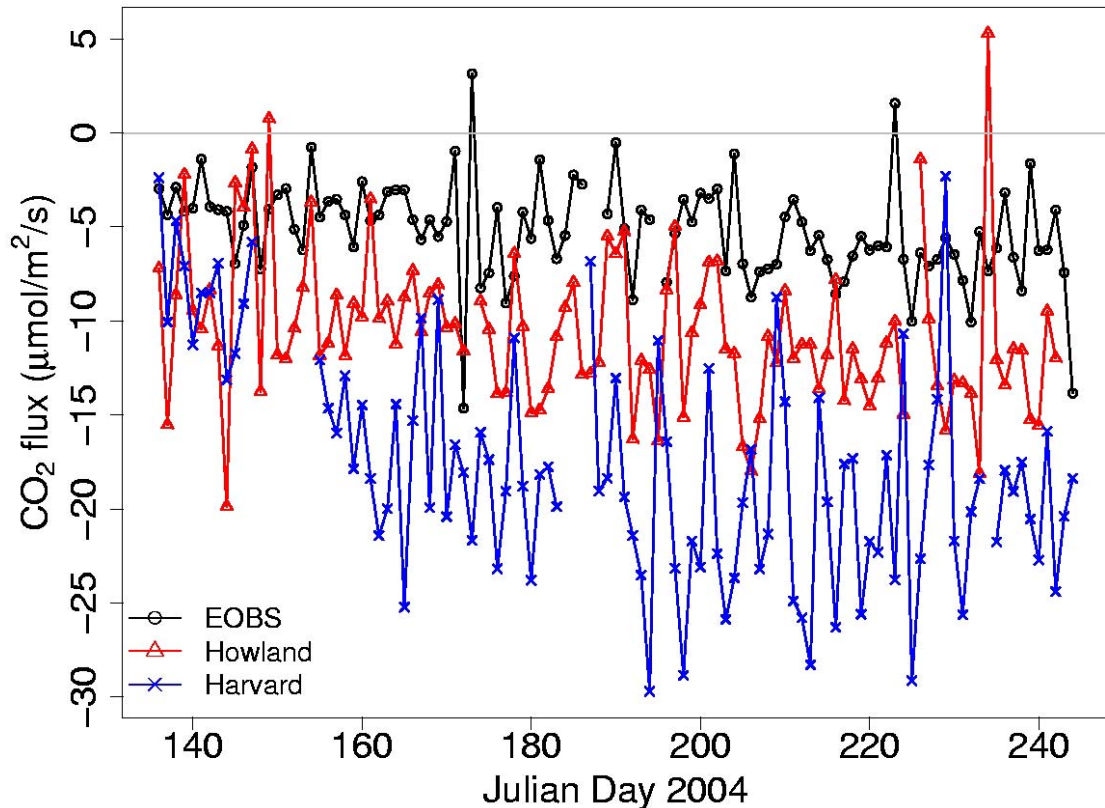


Figure 2.20 – Afternoon average flux values (one point per day) during COBRA-Maine for three flux towers demonstrating a north-south gradient in vegetation uptake.

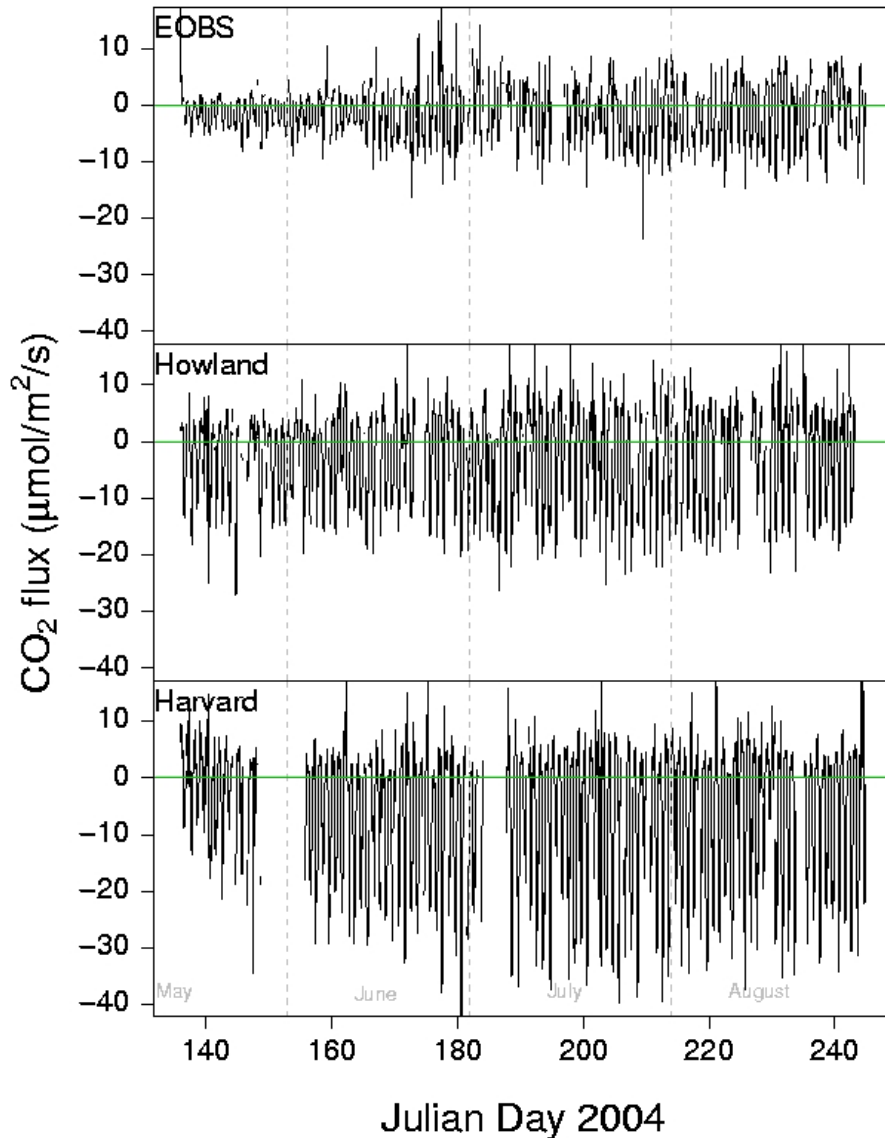


Figure 2.21 – Hourly Flux values from three flux towers along a latitude gradient showing the seasonal trends and magnitude of fluxes at each site

When interpreting Lagrangian experiments in the model of Lin et al. (2004), the atmospheric residual layer can provide valuable additional information. Stull (1988) defines the residual layer as a neutrally stratified layer of air formed as turbulence decays just before sunset that contains initial mean state variables of the formerly mixed layer from the afternoon. Passive tracers such as CO₂ concentration are conserved as the air is

advected downstream; and tracers not necessarily passive, such as water vapor, can be conserved as well. As a stable nocturnal boundary forms overnight, the residual layer sits on top of it and does not have direct contact with the ground. As the surface warms the following day, the residual layer from the previous day becomes entrained into a new mixed layer. For CO₂, a typical residual layer observed early in the day is marked by a layer of decreased concentration from vegetative uptake the previous day, situated above a surface layer of elevated concentrations from nighttime vegetative respiration the previous night. Figure 2.22 vividly demonstrates the classic daytime evolution of a residual layer in CO₂ from three profiles over Argyle on July 30th, 2004. The 9:05 EDT profile shows a very distinct layer of decreased CO₂ between 400 m and 1000 m. The 11:40 EDT profile demonstrates an intermediate stage partial mixing of the residual layer with the remains of the stable nocturnal boundary layer and a growing mixed layer. The 15:40 EDT profile shows a very well mixed boundary layer that extends to 1600 m, with a surface influence very similar to the previous day, as indicated by the very similar concentrations in the morning residual layer and the afternoon mixed layer. The residual layer can also be seen in altitude cross-sections along certain flight tracks. Figure 2.23 shows the cross-section from the June 8th morning flight over New England, with a prominent residual layer in the middle which breaks down over the course of the flight.

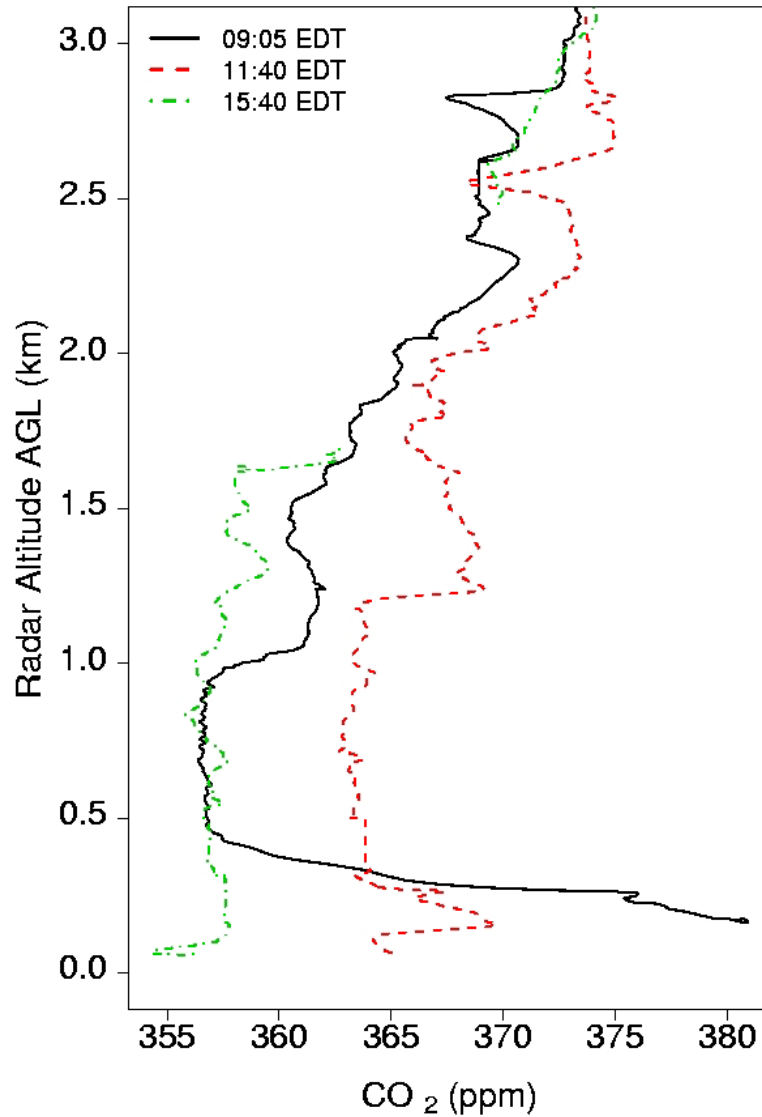


Figure 2.22 – Vertical profiles over Argyle tower at different times of day on July 30th. The morning profile demonstrates a classic residual layer with low CO₂ lying above the developing mixed layer with high CO₂. The afternoon profile indicates a well mixed planetary boundary layer with low CO₂ throughout.

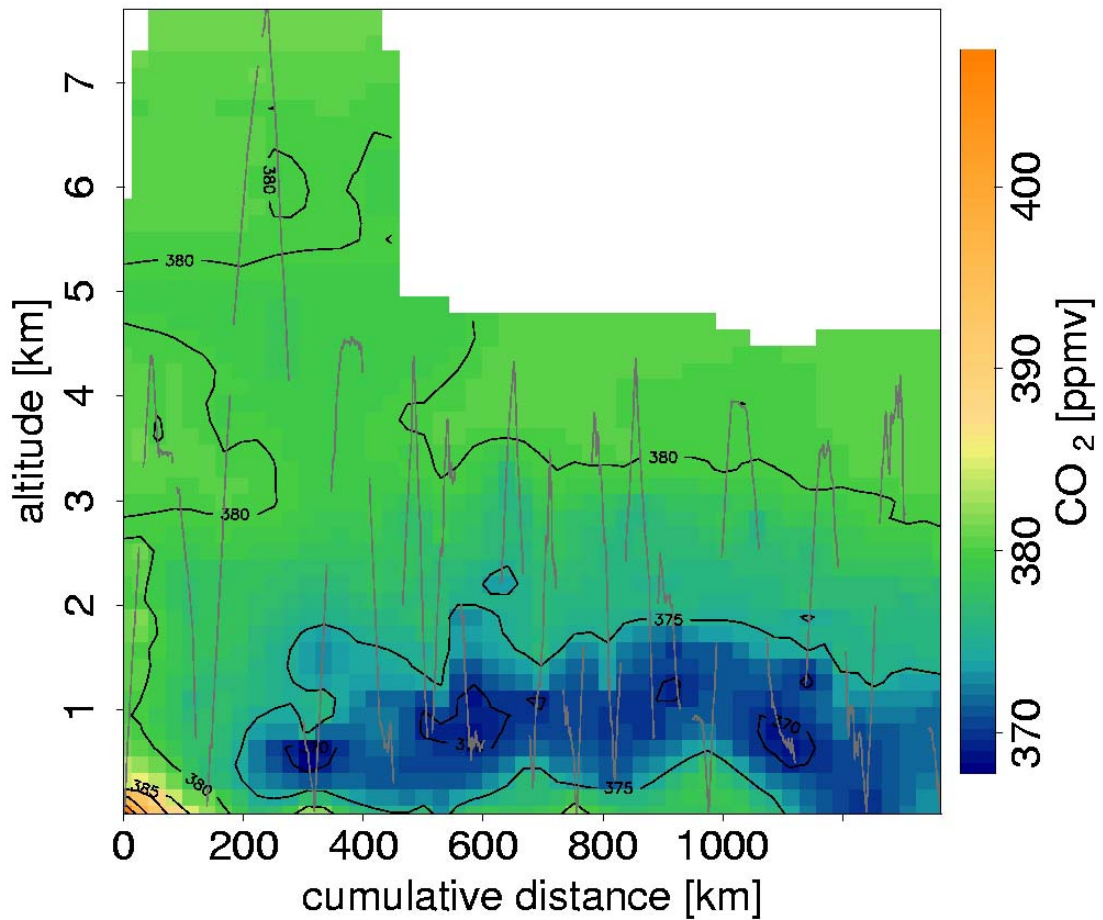


Figure 2.23 – Cross-section along the flight track of the morning of June 8th, taken over New England. There is a prominent residual layer in the middle, which mixes to the surface by the mid-morning culmination of the flight.

A profile taken while climbing out from a missed approach at the Bar Harbor airport on the morning of June 8th, 2004 (Figure 2.24) again shows a well defined residual layer containing the signature of terrestrial vegetative uptake from the previous day. There is a very sharp inversion at the bottom of the profile marking the marine layer. The marine layer is well defined because the water temperature is still relatively cold (around 7 °C; Figure 2.12) and in acute contrast to the air temperature above and the mid-morning land surface, creating a roughly 10 °C inversion during this period. The observed

inversion is borne out by Figure 2.25, a photograph which shows low hanging stratus directly over the water, but not over the land, and capped sharply by the inversion.

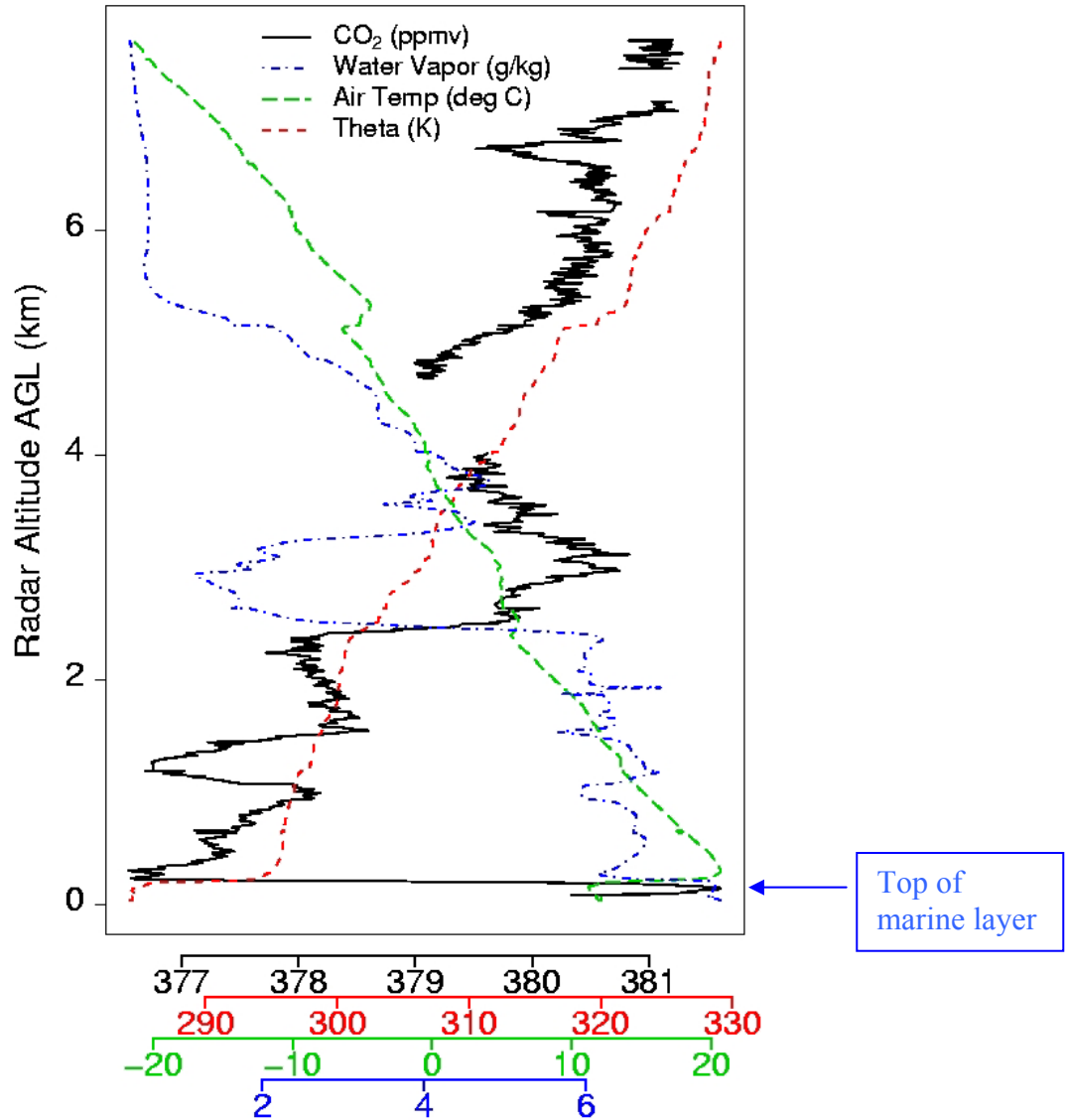


Figure 2.24 – Profile on climb out from a missed approach at Bar Harbor on June 8th. There is a sharp inversion at 300 m over the marine layer.

The shape of the cloudbank very distinctly follows the coastline near the airport. The coastline marks a sharp boundary in atmospheric regimes in the surface layer, which can also be seen in the cross-section along the flight path (Figures 2.23, 2.26). Modeling CO₂ concentrations at coastal locations like Bar Harbor and Chebogue Point require accurate

representation of the marine boundary layer, which is a very different situation to model than the concentrations at a tall tower such as Argyle away from the coast. Model-data fusion schemes seeking to use these observations in an inversion are very much dependent upon how well they can represent atmospheric dynamics, especially in the boundary layer, in these two very different situations.



Figure 2.25 – Bar Harbor Airport on the morning of June 8th, 2004. Low marine stratus sit over cold ocean water in nearby inlets, capped by a strong inversion, but clear skies persist over land.

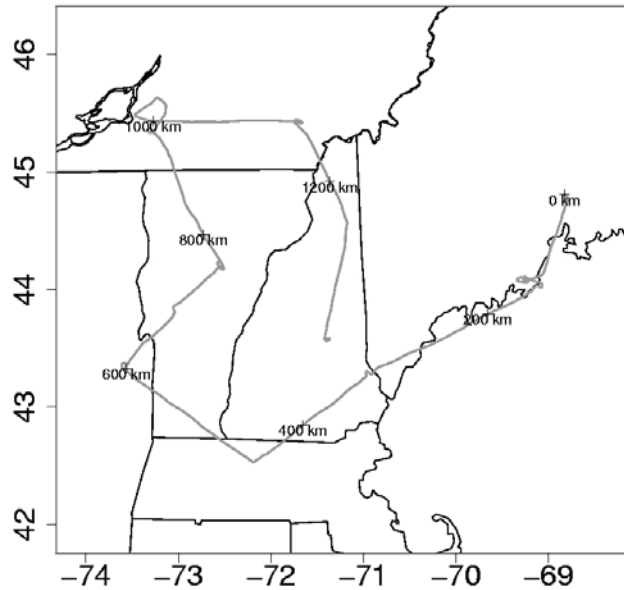


Figure 2.26 – Flight track from morning flight of June 8th.

The profile for CO corresponding to Figure 2.24 did not show any structure, indicating that there was not extensive pollution trapped in the marine layer near Bar Harbor that day, as can sometimes be the case. COBRA-Maine flights were designed to avoid anthropogenic pollution as much as possible, and only rarely encountered very obvious urban plumes. One of the few encounters with an urban plume can be seen in the tracer cross-sections from the morning flight on August 15th, 2004, where there is clearly elevated CO and CO₂ in the profile at 600 km along the flight track as the King Air descended into the boundary layer within sight of the Minneapolis-Saint Paul metropolitan area (Figures 2.27 and 2.28). Although rarely encountering pollution near the surface, COBRA-Maine did occasionally encounter layers of pollution at altitude that were clearly the result of longer range transport. Figure 2.29 shows a profile with a prominent layer of elevated CO, Ozone, and CO₂ at altitude taken enroute between Roberval and Chibougamau in central Quebec (around 49°N and 73°N), well away from

and upstream of any urban influences. There was a visible haze layer at altitude that corresponds to the elevated CO levels measured in the profile (Figure 2.30). Since flow was from the northwest at the time, the origin of this haze is as yet undetermined, but may very well be associated with intercontinental pollution transport. 2004 also had some of the largest Alaskan forest fires in recent memory, so the haze could also be associated with early season biomass burning.

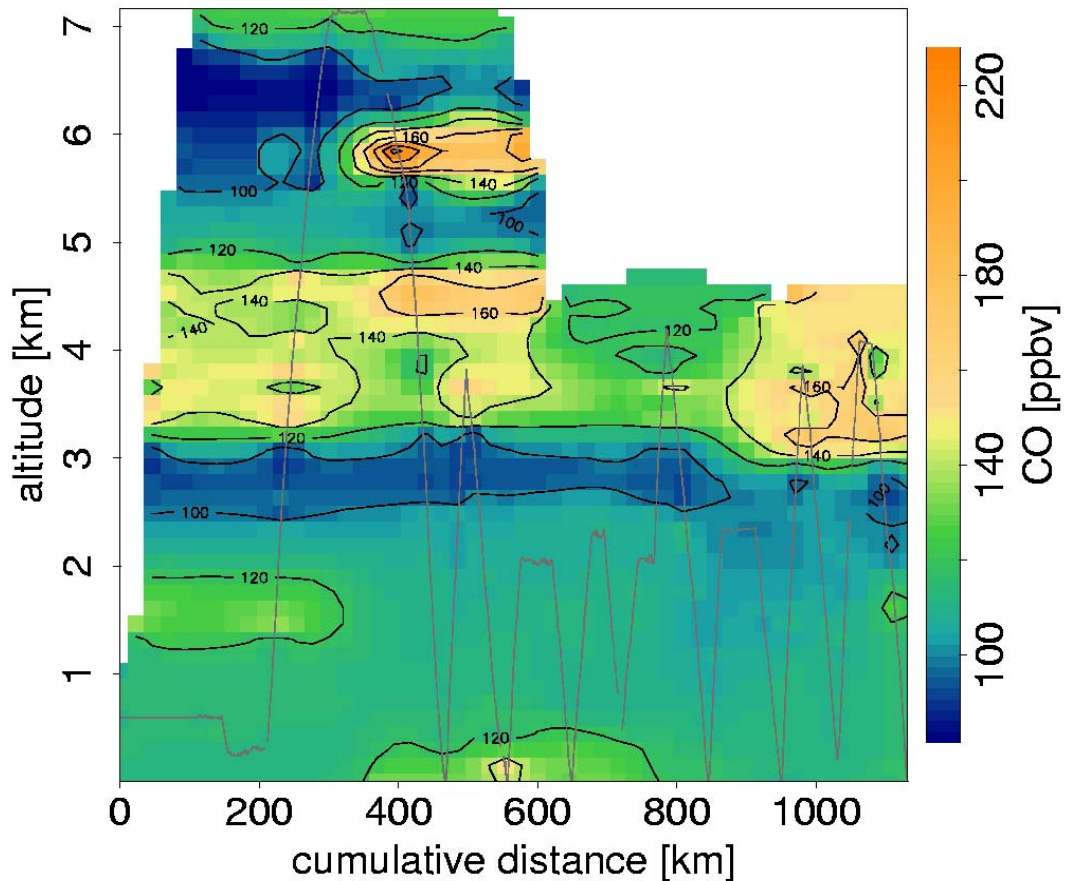


Figure 2.27 – CO cross-section from flight over Wisconsin on August 15th. There is evidence of encountering an urban plume from Minneapolis at ~600 km along the flight track

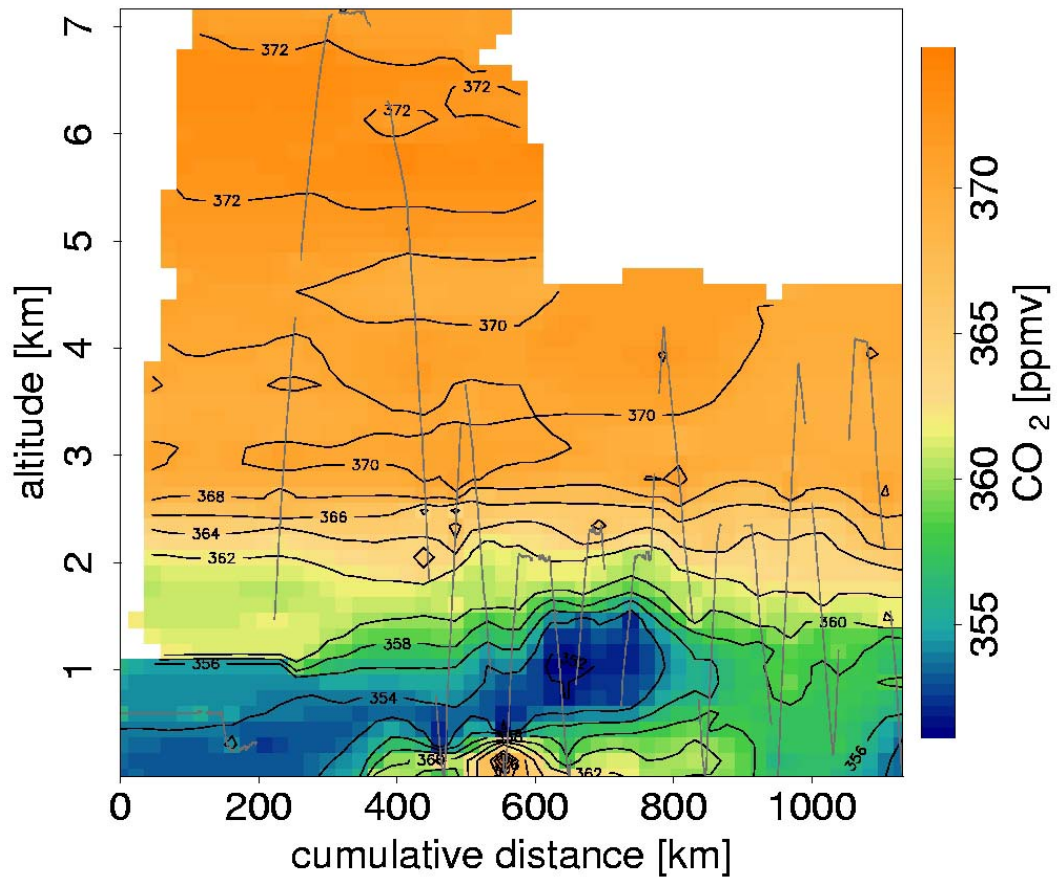


Figure 2.28 – CO₂ cross-section from flight over Wisconsin on August 15th. A residual layer can be seen in the middle of the flight track in addition to the urban plume in the boundary layer at ~600 km along the flight track.

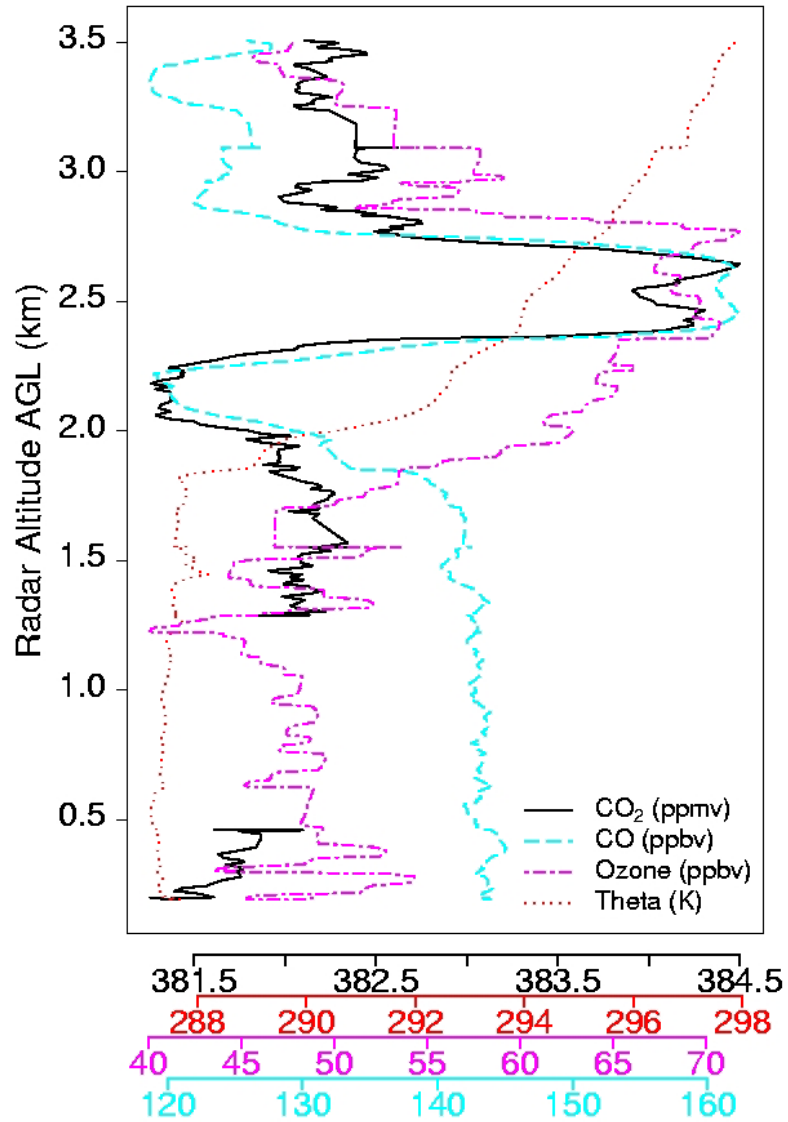


Figure 2.29 – Profile from the afternoon May 19th over central Quebec showing a haze layer of unknown origin at 2.5 km. The top of the mixed layer is sharply defined at 1.8 km.



Figure 2.30 – Thin layer of haze at altitude over Central Quebec on May 19th, 2004

Statistical characterization of COBRA-Maine data can provide a pointed tool for assessing and validating model performance. For example, one particularly important model variable for previous terrestrial CO₂ surface flux model data fusion studies (e.g. Gerbig et al., 2003b) and interpretation of Lagrangian experiments (Lin et al., 2004) is height of the mixed layer, z_i . COBRA-Maine collected 927 vertical profiles, a set of data which when taken as an ensemble can be used to derive error terms associated with calculation of z_i in atmospheric transport models. Visual inspection of the COBRA-Maine profiles of potential temperature, temperature, CO₂, CO, O₃, turbulence, and water vapor led to a discernable boundary layer in 600 cases. Figure 2.31 shows a QQ-norm plot the residual between z_i determined by manual examination of the profile tracer data and the z_i determined by the NCEP Eta Data Assimilation System (EDAS-40 km; Rolph, 1997) reanalysis transport model product. Residuals show a Gaussian pattern with a long tail and the model appears to have bias towards underestimating z_i by about 230 m.

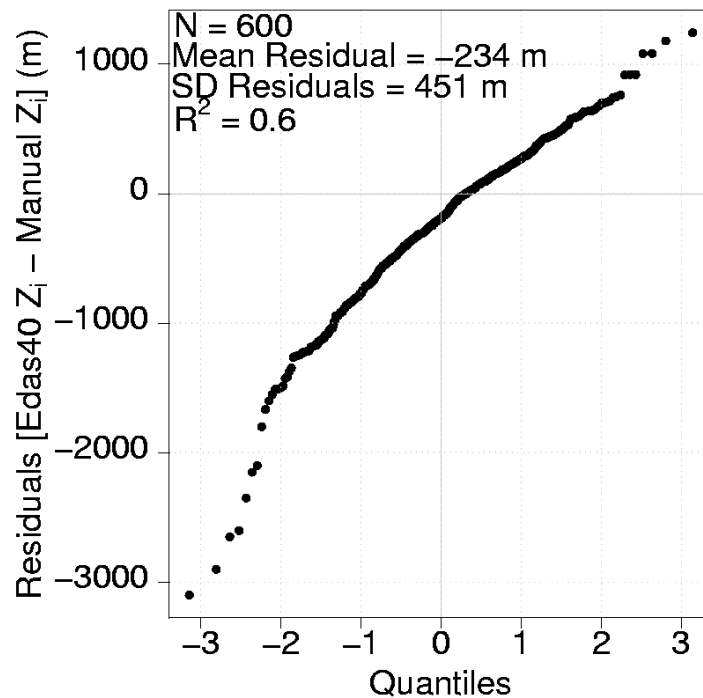


Figure 2.31 – QQ norm plot showing residuals from comparison of model-derived z_i and z_i determined from observed atmospheric tracer profiles.

In the absence of other errors, if one were to couple EDAS-40 to a vegetation surface flux model, it would be reasonable to expect this error to lead to underestimates of CO_2 concentration in the daytime boundary layer and overestimates in the nighttime boundary layer. In a Bayesian inversion framework, transport model errors in z_i can be included in calculation of the error covariance matrix for measurements taken in the boundary layer. Chapter 3 presents an example done at Argyle, using a subset of COBRA-Maine airborne profiles in its vicinity. With 200 hours of 1-Hz airborne data, the dataset has many future uses in assessing model performance in assorted contexts.

In addition to quantitative data, there exists a catalogue of qualitative observations recorded by COBRA-Maine onboard scientists which can provide key insights to explain atmospheric phenomenon present in the data. The onboard logs include lists of cloud

bases and cloud tops for each profile, any proximate features (e.g. smokestacks) that might explain anomalies in the data, and notes on haze, convection, and surface conditions. Notes on vegetation can be of particular value to regional-scale modelers of CO₂ surface exchange, as direct observation can be invaluable to verifying land surface type, identifying potential aggregation errors in vegetation type, and anticipating pockets within a regional domain where the surface flux model might fail. Two examples of areas posing particular challenges to regional CO₂ exchange models are shown below. Figure 2.32 shows the landscape in southern Quebec near Sherbrooke and Drummondville, which is classified as grassland in the USGS Global Land Cover Characteristics (GLCC 2.0; Loveland et al., 2000) 1-km resolution database (<http://edcsns17.cr.usgs.gov/glcc/background.html>).



Figure 2.32 – A landscape classified as grassland, but used for bovine grazing. Veins of mixed forest indicate this landscape may not behave like other grasslands in models

Although a grassland classification is the best option, the landscape is fairly patchy, dominated by pasture managed for grazing, but with a significant amount of mixed forest in sub-gridscale clusters. Figure 2.33 shows another challenging surface environment to successfully model, with wetlands in the foreground, a mix of productive and unproductive forest in the middle, a prominent lake, and mountains with varying vegetation in the distance. The real landscape is clearly complex, mostly governed by soil moisture dynamics, land use, and small scale topography which is difficult for land surface models to capture. Mesoscale atmospheric flows associated with the mountain regime further complicate efforts to model regionally representative CO₂ fluxes based on atmospheric concentration data.



Figure 2.33 – A very challenging landscape on which to accurately model CO₂ surface exchange. There is wide variability between the foreground and background, the mountains challenge atmospheric models, and productivity of the wetlands in the foreground very likely depends on small topographic gradients.

2.7 Conclusion

The above examples demonstrate various ways to aggregate, display, and interpret many facets of the COBRA-Maine dataset for use in atmospheric models. The rest of this thesis is devoted to putting COBRA-Maine tower and airborne observations together in a receptor-oriented framework for modeling and analyzing terrestrial CO₂ exchange, only one possible application. While a substantial amount airborne and accompanying tower data from multiple locations are included, the assimilation to be presented in the following chapters mostly uses the data in the coarsest sense, as a bulk set of airborne and tower observations made over a four month period. For example, individual Lagrangian experiments are not analyzed determine daily fluxes nor is information about surface exchange potentially available extracted from the structure of the observed residual layers. Other current studies, for example Emmons et al. (2006) for satellite validation, also use the COBRA-Maine airborne data as a primarily ensemble set of observations. A bulk treatment utilizing the most readily observed large trends is appropriate and necessary for investigations commencing immediately after completion of the campaign. However, future studies should seek to capitalize on the fine temporal and spatial structure of data in part presented here.

Chapter 3: Estimating regional carbon exchange in New England and Quebec by combining atmospheric, ground-based, and satellite data

(Accepted for publication in the Tellus B: International Carbon Dioxide Conference Special Issue, November 2006. Please see reference for Matross et. al., 2006)

3.1 Abstract

We derive regional-scale ($\sim 10^4$ km²) CO₂ flux estimates for summer 2004 in the northeast United States and southern Quebec by assimilating extensive data into a receptor-oriented model-data fusion framework. Surface fluxes are specified using the Vegetation Photosynthesis and Respiration Model (VPRM), a simple, readily optimized biosphere model driven by satellite data, AmeriFlux eddy covariance measurements, and meteorological fields. The surface flux model is coupled to a Lagrangian atmospheric adjoint model, the Stochastic Time-Inverted Lagrangian Transport Model (STILT), that links point observations to upwind sources with high spatio-temporal resolution. Analysis of CO₂ concentration data from the NOAA-ESRL tall tower at Argyle, ME and from extensive aircraft surveys, shows that the STILT + VPRM framework successfully links model flux fields to regionally-representative atmospheric CO₂ data, providing a bridge between “bottom-up” and “top-down” methods for estimating regional CO₂ budgets on timescales from hourly to monthly. The surface flux model, with initial calibration to eddy covariance data, produces an excellent *a priori* condition for inversion studies constrained by atmospheric concentration data. Exploratory optimization studies show that data from several sites in a region are needed to constrain model parameters for all

major vegetation types, because the atmosphere commingles the influence of regional vegetation types, and even high-resolution meteorological analysis cannot disentangle the associated contributions. Airborne data are critical to help define uncertainty within the optimization framework, showing for example, that in summertime CO₂ concentration at Argyle (107 m) is ~0.6 ppm lower than the mean in the planetary boundary layer.

3.2 Introduction

Terrestrial carbon budgets at regional and continental scales ($\sim 10^4$ to 10^6 km²) are key to assessment of human impact on ecosystems and atmospheric composition. However, obtaining and validating regional-scale fluxes of CO₂ and other important trace gases has proven to be a scientific challenge. Efforts to quantify distributions of sources and sinks of CO₂ have focused on global inverse modeling of CO₂ concentration data from the global monitoring network. Most recently, the globe has been split into 10-20 large regions (Gurney et al., 2002; Gurney et al., 2004). Aggregation errors and errors in atmospheric transport, both within the boundary layer and between the boundary layer and free troposphere, can be formidable obstacles to using this approach to obtain reliable quantitative estimates of carbon fluxes at regional and continental scales (Gloor et al., 1999). Global-scale inversions can not account for important planetary boundary layer processes which affect the concentrations on which they are based, subjecting them to an additional representation error (Kaminski and Heimann, 2001).

Observations of CO₂ over the continent can potentially provide the information needed to determine regional fluxes. The analysis must quantitatively account for the large variability introduced by sources and sinks in the near-field of the measurement

location (Gerbig et al., 2003a), requiring detailed understanding of terrestrial CO₂ sources and sinks at spatial and temporal scales much finer than those used in global inversions. In particular, climate variations and human impacts are often most readily evident at the regional and continental scales. Methods to quantify CO₂ sources and sinks at this scale, intermediate between global and very localized, are notably lacking. Moreover, different regions can vary markedly in response of the carbon cycle to a changing climate (Fung et al., 2005; Friedlingstein et al., 2003). From a policy perspective, the inability to reliably quantify carbon exchange at the regional scale presents a potential stumbling block to future regulatory goals, e.g. developing markets for verifiable trading of CO₂ emissions.

Eddy covariance measurements are a rich source of information on temporal variability and environmental controls of CO₂ exchange between the atmosphere and terrestrial ecosystems (Law et al., 2002); they have semi-continuous temporal coverage at an increasing number of sites across the continent. Unfortunately, it is difficult to reliably scale up eddy-flux measurements to regional scales from the localized footprint ($\sim 10^1 - 10^2 \text{ km}^2$) of the measurements or to test regional flux models developed using micrometeorological measurements.

Concentration data for CO₂ from tall towers ($> \sim 100 \text{ m}$) provide a potentially powerful constraint on “bottom-up” flux models, because the relatively large footprint provides an integrated signal of CO₂ exchange at the regional scale (Gloor et al., 2001). Previous efforts to interpret the signal of regional CO₂ exchange using tall tower concentration data have focused on simple one-dimensional atmospheric boundary layer budgets that rely on gradients in CO₂ concentrations between the boundary layer and the free troposphere (Helliker et al., 2004; Bakwin et al., 2004). These methods are limited to

monthly resolution by the need to smooth and average over several synoptic events. They also use a marine boundary layer surrogate for the free tropospheric CO₂ concentration over the continent, because of limited observations.

Gerbig et al. (2003a) and Lin et al. (2006) showed however that free tropospheric concentrations depart significantly from the MBL reference over the continent, leading to biases in calculations of regional CO₂ flux. These differences result largely from the time lag for vertical propagation of marine boundary layer concentration changes upward from the surface into the free troposphere (Gerbig et al., 2003a), as well as from meridional transport via meandering of the polar jet, and deep convective events (Gerbig et al., 2003a).

This paper uses CO₂ concentrations from a tall tower at Argyle, Maine to critically test a bottom-up CO₂ surface flux model based on assimilation of eddy covariance fluxes. The surface flux model is an application of the Vegetation Photosynthesis and Respiration Model (VPRM, http://people.deas.harvard.edu/~swofsy/VPRM_submitted.zip, hereafter referred to as Pathmathevan et al., 2006), a diagnostic CO₂ flux model with a minimum number of parameters (3 per vegetation class) driven by remote sensing and weather data. We focus on CO₂ sources and sinks for northern New England and southern Quebec in summer 2004, when we made extensive aircraft flights in the region. The Stochastic Time-Inverted Lagrangian Transport (STILT) Model (Lin et al., 2003), an adjoint transport model with high spatio-temporal resolution, provides the quantitative link between surface fluxes calculated with the VPRM and the time series of concentration observations at the Argyle, Maine. We then examine the number of degrees of freedom in

the STILT+VPRM inverse problem, applied at this single tall tower, to lay the groundwork for future inverse studies seeking to obtain regional or continental fluxes using a network of tall tower measurements.

3.3 Methodology

Gerbig et al. (2003b) developed the receptor-oriented modeling framework that provides the basis for this study, consisting of four major components: 1) influence functions from the STILT model that quantitatively link upstream spatially/temporally-resolved surface sources/sinks to concentration measurements at a receptor point (i.e. a measurement location) 2) a lateral continental CO₂ boundary condition for North America from Pacific observations; 3) Fossil fuel CO₂ inventories; 4) a model for surface CO₂ fluxes; in this case, the VPRM of Pathmathevan et al. (2006).

3.3.1 STILT Adjoint Atmospheric Model

STILT is analogous to the adjoint of an Eulerian transport model, with footprint elements representing the sensitivity of the mixing ratio at receptor location to any given surface flux (Errico, 1997). Information about a footprint, the upstream source region of surface influences on air at a particular measurement point, comes from computing transport of an ensemble of particles—representing air parcels—backward in time using winds and turbulence statistics from a high-resolution meteorological assimilation. STILT links the local concentration $C(\mathbf{x}_r, t_r)$ of a conserved tracer, measured at a receptor location \mathbf{x}_r at time t_r , to the surface sources S for the tracer emitted at upstream locations \mathbf{x} at prior time t , by computing the influence function $I(\mathbf{x}_r, t_r | \mathbf{x}, t)$ (Lin et al., 2003) through Equation 3.1a.

$$C(\mathbf{x}_r, t_r) = \int_{t_0}^{t_r} dt \int_V d^3x I(\mathbf{x}_r, t_r | \mathbf{x}, t) S(x, t) + \int_V d^3x I(\mathbf{x}_r, t_r | \mathbf{x}, t_0) C(\mathbf{x}, t_0) \quad (3.1a)$$

The first term in Equation 3.1a represents ΔCO_2 at the receptor due to surface sources in domain V between time t_0 and t_r . The second term in Equation 3.1a is the advected contribution from the initial tracer field, which in this case is represented by a boundary condition based on observations in the mid-Pacific (see below). STILT represents surface fluxes as volume sources distributed from the surface through a mixing height h . Lin et al. (2003) recast the first term in Equation 3.1a using Equation 3.1b, which incorporates a surface flux $F(\mathbf{x}, t)$ and a footprint element f , which is mathematically defined in Equation 3.2.

$$\Delta C(\mathbf{x}_r, t_r) = \int_{t_0}^{t_r} dt \int_A d^2x f(\mathbf{x}_r, t_r | \mathbf{x}, t) F(\mathbf{x}, t) \quad (3.1b)$$

$$f = \int_0^h dz I(\mathbf{x}_r, t_r | \mathbf{x}, t) \times m_{\text{air}} / (h \rho_{\text{air}}) \quad (3.2)$$

The value of the footprint calculation depends on the initial column height, h , below which turbulent mixing is strong enough to mix the surface signal. STILT calculates the height of the planetary boundary layer based on a modified Richardson number method (Lin et. al. 2003) and h is determined as a fraction of that value. Gerbig et al. (2003b) found that simulated footprints were insensitive to values of h between 10 and 100% of the planetary boundary layer height.

As currently implemented, the transport fields to drive STILT can come from operational global forecast or reanalysis products (e.g. Eta Data Assimilation System,

Nested Grid Model, European Center for Medium range Weather Forecast model) or from mesoscale models run specifically for periods and domains of interest (e.g. Regional Atmospheric Modeling System (RAMS), Weather Research and Forecasting model (WRF)). A stochastic Markov chain is used to represent sub-gridscale turbulence. STILT can explicitly model convection, e.g. in convective storms, if the driver provides convective mass fluxes. The footprint f is derived from the local density of particles by counting the number in surface-influenced boxes and determining the amount of time each particle spends in each surface volume element during each time step; the results can be visualized by plotting the time- and area-integrated footprint of f ($\langle\langle f \rangle\rangle$ units: $\text{ppm}/(\mu\text{mole m}^{-2} \text{ s}^{-1})$). Principal advantages of STILT include the great care taken to conserve mass and to maintain well-mixed conditions (viz. to obey the 2nd Law of Thermodynamics), the considerable computational advantage provided by the backward-time, receptor-oriented formulation: i.e., running a minimum number of representative particles backward in time, each of which influences the receptor point, and the high spatial and temporal resolution achieved at modest computational cost (Lin et. al, 2003; Gerbig et. al, 2003b).

3.3.2 Empirical Lateral Tracer Boundary Condition

A lateral tracer boundary condition is required to connect regional simulations to the global background distribution. We use a statistical approach based on available observations in the Pacific to characterize spatial and temporal dependence of tracer variations. The boundary condition for North America is imposed at 145° W, representing tracer concentrations over the mid-Pacific ocean before air parcels enter the dominant

westerly flow over North America. Most particles cross 145° W after being transported back for roughly six days from receptor points in the U.S. (Gerbig et al., 2003b).

Gerbig et al. (2003b) describe the full development of the lateral boundary condition, including a complete categorization of the extensive airborne and station data used in its development. The statistical analysis consists of a Fourier decomposition of observed CO₂ time series from marine surface stations to yield an analytical representation, followed by fitting a Green's function to aircraft CO₂ measurements, to represent the vertical propagation of the seasonal signal at the into the middle and upper troposphere. For this study, we updated the station data from Pacific ground stations in the NOAA GMD network (Cape Kumakahi, HI; Cold Bay, AK; and Barrow, AK) to include the period from January 1st, 1980 through December 31st, 2004. In addition, we updated upper air profiles from regular NOAA GMD aircraft flights over Carr, CO, Poker Flats, AK, and Park Falls, WI during 2003 and 2004, along with measurements from the Niwot Ridge surface station. The result is a time-latitude-height boundary condition, based on data from 1980 to 2004, consisting of meridional (145° W) cross-sections for CO₂ with spatial resolution of 0.5 km altitude by 2.5° latitude and daily time resolution.

3.3.3 Fossil Fuel Inventory

The fossil fuel inventory is unchanged from Gerbig et al. (2003b). Emissions of CO₂ from fossil fuel, cement production, and gas flaring come from the 1° x 1° database compiled by Marland et al. (1997), with methodology described by Andres et al. (1996). A linear extrapolation is applied, propagating the trend between 1992 and 1996, and resulting in a 10% total increase in emissions since 1996. Time-of-day and day-of-week

scaling factors are applied to account for time-dependence of emission fluxes following Ebel et al. (1997). As described in Gerbig et al. (2003b), the time factors for carbon monoxide are applied to CO₂, with the amplitude reduced by a factor of 2.5. The day-of-week factors are 0.95 on weekends and unity on weekdays. Time-of-day factors average to unity, and range from 0.69 in the middle of the night to 1.3 for the rush hour peak.

3.3.4 Vegetation Photosynthesis and Respiration Model

The VPRM is a powerful new data-driven diagnostic biosphere flux model fully described in Pathmathevan et al. (2006), extending the Vegetation Photosynthesis Model developed by Xiao et al. (2004) to include respiration and saturation of photosynthesis at high light levels. The VPRM conceptually partitions sunlight between photosynthetically active vegetation and non-photosynthetic components within the leaf and canopy. Satellite data provide independent information on the spatial and phenological variations of gross primary production using the Enhanced Vegetation Index (EVI) and Land Surface Water Index (LSWI), both from MODIS-Terra. Model parameters are initially determined through fitting to eddy covariance data from AmeriFlux sites. The model uses temperature from the same meteorological files used by STILT, and incident solar radiation from those same fields or from retrievals based on data from the North American Land Data Assimilation System (NLDAS; <http://ldas.gsfc.nasa.gov/>, Mitchell, et al., 2003;). Net flux is computed every hour on a grid of 1/4° longitude by 1/6° latitude.

The VPRM bins the GLCC 2.0 1-km resolution vegetation inventory (Loveland et al., 2000; <http://edcsns17.cr.usgs.gov/glcc/>) into eleven classes (ten vegetation + one flux neutral class; Figure 3.1) and calculates net ecosystem exchange (NEE) of CO₂ for each vegetation class in each grid square separately, scaled by vegetation fraction. NEE is the

sum of two model terms: a light-dependent term, identified with canopy photosynthesis (GEE), and a temperature-dependent term identified with ecosystem respiration (R).

GEE, as calculated in Equation 3.3, is assumed to be a function of shortwave incident flux (SW) and to the observed Enhanced Vegetation Index (EVI; Huete et al., 1997).

$$GEE = \lambda \times T_{scale} \times W_{scale} \times P_{scale} \times \frac{1}{\left(1 + \frac{SW}{SW_0}\right)} \times SW \times EVI, \quad (3.3)$$

where SW_0 is the half-saturation value for photosynthesis derived from eddy covariance data for each vegetation type.

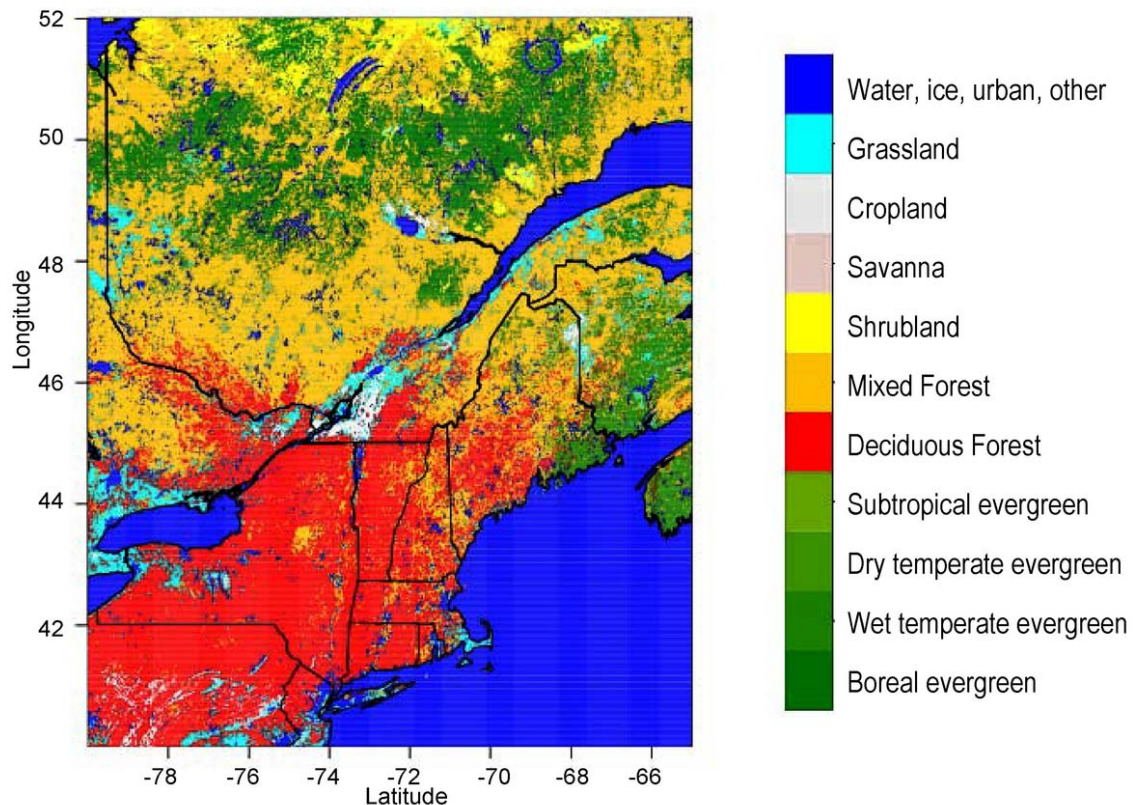


Figure 3.1 – VPRM vegetation classification (1-km resolution) for the Northeast U.S. and Southern Quebec, the area with significant influence on Argyle observations. This is modified from the GLCC 2.0 database (Loveland et al., 2000; Pathmathevan, et al. 2006).

The calculation of GEE in Equation 3.3 includes several scalar functions. These light-, temperature- and water-dependant scalars are defined as needed for individual vegetation classes in order to accommodate the large range of light- and water-utilization strategies observed in nature. The first scalar in Equation 3.3 is a temperature function (T_{scale}), as calculated in Equation 3.4, capturing temperature sensitivity of photosynthesis for each vegetation type.

$$T_{scale} = \frac{(T - T_{min}) \times (T - T_{max})}{[(T - T_{min}) \times (T - T_{max}) - (T - T_{opt})^2]} \quad (3.4)$$

The second scalar in Equation 3.3 adjusts for water-stress (W_{scale} based on the Land Surface Water Index (LSWI)), as calculated in Equations 3.5a and 3.5b.

$$W_{scale} (\text{grassland/savanna}) = \frac{(LSWI - LSWI_{min})}{(LSWI_{max} - LSWI_{min})} \quad (3.5a)$$

$$W_{scale} (\text{other vegetation types}) = \frac{(1 + LSWI)}{(1 + LSWI_{max})} \quad (3.5b)$$

The third scalar in Equation 3.3 is a phenology-tracking function based on LSWI (P_{scale}),

$$P_{scale} (\text{evergreen}) = 1 \quad \{\text{all times}\} \quad (3.6a)$$

$$P_{scale} (\text{grassland/savanna}) = \frac{(1 + LSWI)}{2} \quad \{\text{all times}\} \quad (3.6b)$$

$$P_{scale} (\text{other vegetation types}) = 1 \quad \{\text{full canopy period}\} \quad (3.6c)$$

$$= \frac{(1 + LSWI)}{2} \quad \{\text{bud-burst to full canopy}\}. \quad (3.6d)$$

The bud-burst and full canopy periods of Equations 3.6c and 3.6d are based on EVI, as outlined in Pathmathevan et al. (2006).

In the calibration of the VPRM to eddy covariance data, GEE is multiplied by an adjustable parameter (λ) for each vegetation type, representing the overall light use efficiency of the ecosystem. Adjustments which scale λ in our inverse modeling studies represent adjustments of the photosynthesis efficiency for a particular vegetation class over the landscape, as constrained by the tall tower data.

The VPRM utilizes a linear formulation for respiration (R), as calculated in Equation 3.7. R is a function of a second calibration factor (α) that captures the dependence of respiration on air temperature, when temperatures are above a minimum temperature T_{min} , and an additional calibration parameter (β) represents the basal respiration rate (e.g. during winter when $T < T_{\text{min}}$) for a given vegetation type.

$$\begin{aligned}
 R &= \alpha \times T + \beta && \{T > T_{\text{min}}\} \\
 R &= \alpha \times T_{\text{min}} + \beta && \{T \leq T_{\text{min}}\}
 \end{aligned}
 \tag{3.7}$$

The sets of three scaling parameters $\{\lambda, \alpha, \beta\}$ of the VPRM were calibrated for each of ten vegetation classes with eddy covariance data, using all valid hourly NEE measurements for 1-4 years, at ten AmeriFlux sites and validated using data from ten separate sites. The parameters were *not* initially adjusted to fit atmospheric concentration constraints in the present work. Model results with these 30 calibration parameters (dependent on vegetation class, invariant with time, determined using eddy covariance data) accounted for 60-80% of the variance of hourly flux data at the calibration sites, and 50-75% at validation sites; in most cases predictions of seasonal and annual sums at validation sites were quite close to observed values (Pathmathevan et al., 2006).

3.3.5 Argyle Tall Tower Measurements

The receptor oriented modeling framework (STILT, VPRM, fossil fuel inventories, lateral boundary condition) allows calculation of CO₂ concentration at a given receptor point in space for any hour given sunlight and meteorological data. In order to leverage simultaneous measurements being taken during the COBRA-Maine airborne campaign (see below, and Lin et al. 2006), the primary receptor point for this study is the NOAA Argyle tall tower, run by the Global Monitoring Division (GMD) of NOAA's Earth System Research Laboratory (ESRL). STILT is used to determine the influence functions and the upstream footprint, which are multiplied by the spatially-resolved, hourly biosphere fluxes from the VPRM and fossil fuel fluxes from the inventory. Contribution from CO₂ advected from the lateral boundary is added and the result compared to the observations at the receptor.

The Argyle site (45.03° N, 68.68° W) is a cell phone tower located in a northern mixed deciduous, evergreen forest in rural central Maine north of Bangor, elevation 50 m above sea level. The experimental set-up is similar to the WLEF tower (Bakwin et al., 1998), with CO₂ and CO concentration measurements taken every 4 minutes at 12 m and 107 m above ground level. CO₂ is measured with a Licor Li-7000 CO₂/H₂O analyzer calibrated with 5 standard gases. CO is measured with a Thermo Electron model 48CTL CO analyzer calibrated using 2 standard gases. The zero concentration reference for the CO analyzer is checked by catalytically scrubbing CO from ambient air using Sofnocat as a reagent as part of the standard measurement protocol. Supplementary flask samples are collected weekly from the top level and are shipped to the GMD/ESRL laboratory in Boulder, CO for analysis of CO₂, N₂O, CH₄, SF₆, H₂, and CO concentrations, as well as

isotope ratios of ^{13}C and ^{18}O in CO_2 . NOAA GMD began sampling at Argyle on September 17th, 2003.

The focus of this study is the time period of May through August, 2004, coinciding with the COBRA-Maine airborne campaign. COBRA-Maine utilized the University of Wyoming King Air for nearly 200 flight hours over 59 flights in Maine, greater New England and southern Quebec to characterize regional carbon exchange. The campaign was based out of the Bangor International Airport, located roughly 30 km south of Argyle. In total, the aircraft collected over 900 vertical profiles of CO_2 , CO, water vapor, ozone, and meteorological data from the surface to altitudes up to 8 km. Over 120 of those vertical profiles were flown within 50 km of the Argyle tall tower. The flight data provide characterization of CO_2 , CO, and atmospheric structure in the boundary layer and free troposphere in the vicinity of Argyle.

3.3.6 Application STILT+VPRM at Argyle Tall Tower

We utilized the STILT+VPRM receptor oriented modeling framework to compute hourly concentrations during summer 2004 for the receptor at 107m above the ground at Argyle. For each hour, STILT determined influence functions using 100 particles, transported back six days in time by Eta Data Assimilation System 40-km (EDAS-40) reanalysis fields obtained from the NOAA Air Resources Lab server (Rolph, 1997; <ftp://www.arl.noaa.gov/pub/archives/edas40/>). For consistency with Gerbig et al. (2003b), we took an initial column height h for the input of surface emissions (see equation 3.2) to be 50% of the planetary boundary layer height, as calculated from the reanalysis fields. Because we did not have convective mass fluxes available from EDAS-40, we did not explicitly model convection.

Eight-day EVI and LSWI were computed directly from MODIS radiances at 1-km resolution for each of the eleven vegetation classes (ten vegetated, plus non-vegetated such as ocean), using quality control as outlined in Pathmathevan et al. (2006), and aggregated onto a rectangular surface grid spanning 30° to 65° N and 51° to 140° W with resolution 1/6° latitude by 1/4° longitude, taking trimmed mean values from 1-km data for each parameter, for each vegetation type within a grid square. Temperatures to drive the VPRM were taken from the EDAS-40 analysis fields and shortwave radiation was taken from incoming downward solar radiation tabulated by the North American Land Data Assimilation System (NLDAS; Mitchell et al., 2003).

The convolution of STILT influence functions and VPRM fluxes yields a value for CO₂ concentration at Argyle for any hour. We calculated STILT+VPRM concentrations at Argyle for all hours in two representative 15-day periods, one from June 1st to June 15th and one from August 1st to August 15th. We also determined concentrations for midday hours (1400 GMT to 2100 GMT) for the entire summer, May 15th to September 15th, 2004. EDAS fields do not accurately reflect the near-surface atmospheric environment at night, when the tower is influenced mainly by nearby sources. Hence we focused our model-data comparisons on daytime values.

3.3.7 Optimization Approach

In order to place large-scale constraints on the VPRM parameters using the link to atmospheric concentration data at Argyle, we performed a simplified Bayesian optimization approach (Rodgers, 2000) with two adjustable coefficients for each vegetation type, γ and ρ , one respectively for GEE and R . (Gerbig et al., 2003):

$$NEE = \gamma \times GEE + \rho \times R . \quad (3.8)$$

Here GEE and R are computed from Equations 3.3 and 3.7 respectively. The *a priori* model ($\gamma = \rho = 1$ for all vegetation classes) has assimilated a large volume of eddy covariance information through the calibration factors (λ, α, β), but no constraint from atmospheric concentration data had been applied. Thus deviations of Bayesian-optimized γ and ρ from 1 encapsulate the deviation between local-scale carbon fluxes calibrated against eddy covariance measurements and regional-scale carbon fluxes constrained against atmospheric CO₂ observations.

As outlined in Rodgers (2000) and Gerbig (2003b), the measurements at Argyle can be related to vegetation signal (ΔCO_2) from each vegetation class through

$$\mathbf{y} = \mathbf{K} \mathbf{\Gamma} + \boldsymbol{\varepsilon} \quad (3.9)$$

where \mathbf{y} is a vector of measurements, \mathbf{K} is the Jacobian matrix relating the measurement vector to the state vector, $\mathbf{\Gamma}$ is the state vector of scaling factors (γ 's and ρ 's), and $\boldsymbol{\varepsilon}$ is an error vector accounting for uncertainties in measurements and modeling framework. As applied here, the measurement vector \mathbf{y} has a single element for each hourly value at Argyle, calculated by subtracting from the Argyle observation the computed contributions advected from the boundary and associated with fossil fuel combustion. The Jacobian matrix \mathbf{K} computes the CO₂ signals for each vegetation class as determined by the STILT+VPRM from the surface flux model.

The optimum posterior estimates of the scaling factors γ and ρ for each vegetation class, based on atmospheric concentration information from Argyle, are obtained by minimizing the cost function \mathbf{J} using a standard least squares formulation

$$\mathbf{J}(\mathbf{\Gamma}) = (\mathbf{y} - \mathbf{K}\mathbf{\Gamma})^T \mathbf{S}_\varepsilon^{-1} (\mathbf{y} - \mathbf{K}\mathbf{\Gamma}) + (\mathbf{\Gamma} - \mathbf{\Gamma}_{\text{prior}})^T \mathbf{S}_{\text{prior}}^{-1} (\mathbf{\Gamma} - \mathbf{\Gamma}_{\text{prior}}). \quad (3.10)$$

In Equation 3.10, there are two error covariance matrices, one for the vegetation signals, \mathbf{S}_ε , and one for the prior scaling factors, $\mathbf{S}_{\text{prior}}$. $\mathbf{S}_{\text{prior}}$ comes from work extensively detailed in Pathmathevan et al. (2006) comparing observed eddy covariance fluxes to the initial calibration of the VPRM, resulting in standard deviations on the initial calibration factors that can be normalized and propagated for use as prior uncertainties for scaling factors γ and ρ . The off-diagonal elements of $\mathbf{S}_{\text{prior}}$ are assumed to be 0, since the calibration of the VPRM does not introduce covariance in errors between vegetation classes. The values of the diagonal elements in $\mathbf{S}_{\text{prior}}$ for the different vegetation classes are shown in Table 3.3. The formulation \mathbf{S}_ε of is detailed below.

Posterior estimates of $\mathbf{\Gamma}$, optimally consistent with both Argyle measurements and prior estimates of fluxes from the initial calibration of the VPRM, are obtained by minimizing \mathbf{J} . $\mathbf{\Gamma}_{\text{post}}$ can be calculated using Equation 3.11 (Rodgers, 2000).

$$\mathbf{\Gamma}_{\text{post}} = (\mathbf{K}^T \mathbf{S}_\varepsilon^{-1} \mathbf{K} + \mathbf{S}_{\text{prior}}^{-1})^{-1} (\mathbf{K}^T \mathbf{S}_\varepsilon^{-1} \mathbf{y} + \mathbf{S}_{\text{prior}}^{-1} \mathbf{\Gamma}_{\text{prior}}) \quad (3.11)$$

The uncertainty of $\mathbf{\Gamma}_{\text{post}}$ is expressed through a posterior error covariance matrix, \mathbf{S}_{post} , as shown in Equation 3.12.

$$\mathbf{S}_{\text{post}} = (\mathbf{K}^T \mathbf{S}_\varepsilon^{-1} \mathbf{K} + \mathbf{S}_{\text{prior}}^{-1})^{-1} \quad (3.12)$$

Following Gerbig et al. (2003b), the error covariance matrix \mathbf{S}_ε was assumed to be additive:

$$\mathbf{S}_\varepsilon = \mathbf{S}_{\text{veg}} + \mathbf{S}_{\text{part}} + \mathbf{S}_{\text{eddy}} + \mathbf{S}_{\text{transp}} + \mathbf{S}_{\text{aggr}} + \mathbf{S}_{\text{ocean}}. \quad (3.13)$$

\mathbf{S}_{veg} is the uncertainty in the vegetation signal (total ΔCO_2), as given by \mathbf{y} in Equation 3.9.

The associated error covariance matrix \mathbf{S}_{veg} is derived by propagating measurement uncertainty from the Argyle observations (variable between 0.1 and 0.3 ppm) with estimated uncertainties in the advected background and in the contributions from fossil

fuels. We used a value of 1.15 ppm as the standard deviation for normally distributed errors in the advected background, as calculated by Gerbig et al. (2003b). This value is supported by measured differences between calculated advected background values and corresponding free troposphere observations in the vicinity of Argyle during COBRA-Maine (Section 3.4.3) for which the standard deviation was 1.20 ppm. Uncertainty in the contribution due to fossil fuel combustion was assumed to be 30% of the signal (Gerbig et al., 2003b). We did not account for any influence biomass burning may have had on the Argyle measurements; 2004 was generally wet in the region and there were no large fires near Argyle.

S_{part} is the random error due to particle statistics, and is taken to be a diagonal matrix with value 13% of the Argyle signal, in accordance with the relative uncertainties for mixed layer receptor points derived in Gerbig et al. (2003a) for simulations with 100 particles. S_{eddy} is the error due to unresolved eddies, and is calculated from a statistical comparison of Argyle concentrations to mean concentrations within the mixed layer nearby as measured by the aircraft during COBRA-Maine (Section 3.4.3).

S_{transp} is the sum of two terms. 1) The influence of error in modeled height of the mixed layer is calculated from aircraft profiles done near Argyle during COBRA-Maine (Section 3.4.3). For profiles within 50 km of Argyle, the mean difference between EDAS-40 mixed layer height and manually observed height was 200 m, with standard deviation of 500 m. The first part of S_{transp} was calculated by taking the variance in relative differences between EDAS-40 and manual mixed layer height (mean = 0, standard deviation = 0.42) and multiplying by the vegetation signal for that each timestep. 2) Tracer transport error is computed using the method of Lin and Gerbig

(2005), in which direct comparison is made between EDAS assimilated winds and data and radiosonde observations. Statistics of transport errors from this comparison are propagated stochastically through STILT as an added error component reflecting uncertainty in the winds. Tracer transport uncertainty is defined for each hour as the associated variance in concentrations, as determined by Equation 3.1.

S_{aggr} represents the error due to aggregation of fluxes into large finite regions, with diagonal elements estimated as in Gerbig et al. (2003b) to be $(3 \text{ ppm})^2$. Similarly, the error due to neglecting oceanic fluxes, S_{ocean} , is taken directly from Gerbig et al. (2003b) as the upper limit of what those fluxes might have contributed, $0.1 \text{ } \mu\text{mol}/\text{m}^2/\text{s}$.

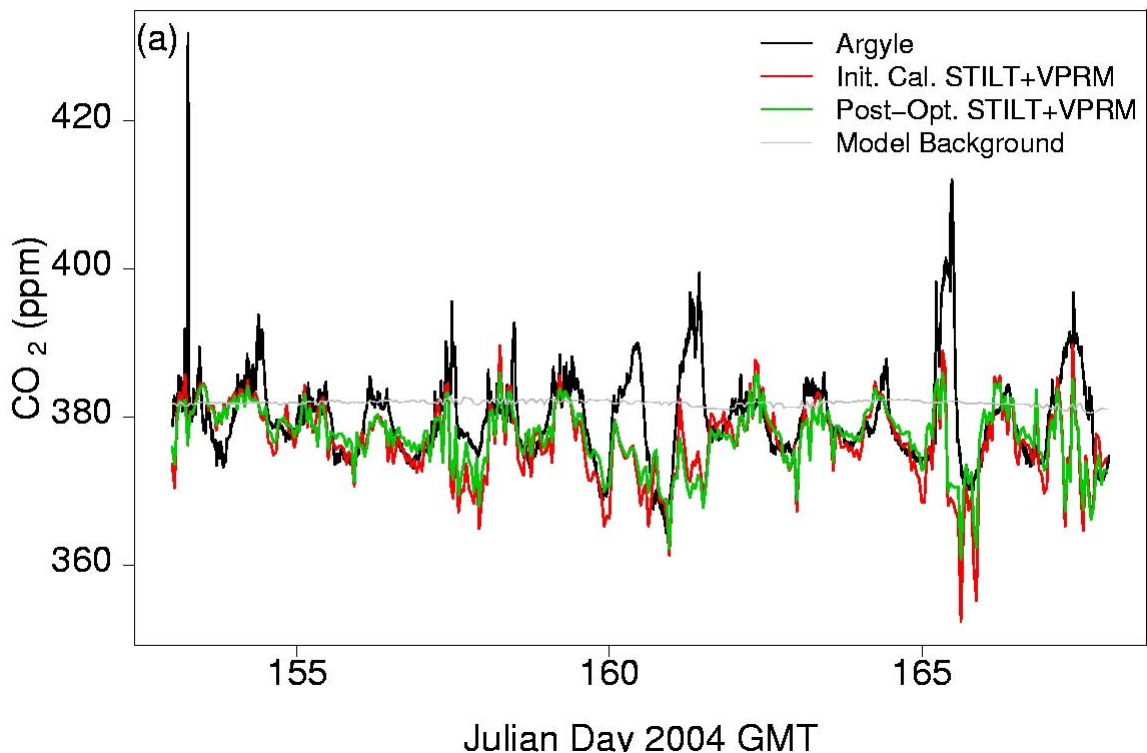
Errors in transport (S_{transp}) and aggregation (S_{aggr}) were assumed to have a temporal correlation that decreased exponentially with a decorrelation timescale of twelve hours. Consequently, there were off-diagonal elements in S_{transp} and S_{aggr} that were calculated by multiplying the diagonal elements with a matrix made from a simple exponential decay function. The twelve hour timescale is meant to capture the synoptic scale variation expected to affect S_{transp} and S_{aggr} . The other terms in Equation 3.13 were assumed to have negligible temporal correlation.

3.4 Results and Discussion

3.4.1 Comparison of Observations and Initially Calibrated STILT+VPRM Results

STILT+VPRM concentrations at Argyle are consistently very close to daytime observations during most periods using the coefficients derived from eddy flux data without adjustment ($\gamma = \rho = 1$ for all vegetation classes). Figure 3.2 shows modeled CO_2 concentrations and model background values calculated from the advected continental

boundary condition along with those measured at Argyle tower, for two 15-day periods, in June and in August 2004. STILT+VPRM also captures summertime seasonal trends of ambient concentrations observed at Argyle. Figure 3.3 (top) shows the STILT+VPRM estimates of CO_2^{veg} compared directly to with the Argyle data, from which we have subtracted the advected background and fossil fuel contributions. Note the drawdown that increases in early summer, then decreases later in the season, reflecting activity of forests in the region. Most synoptic variations are well simulated (e.g. Figure 3.3, bottom; days 230-233 and days 240-245). These reflect both large-scale changes in environmental drivers (sunlight, temperature), changes in advected background and fossil fuel influence, and changes in the particular regions influencing measurements at Argyle.



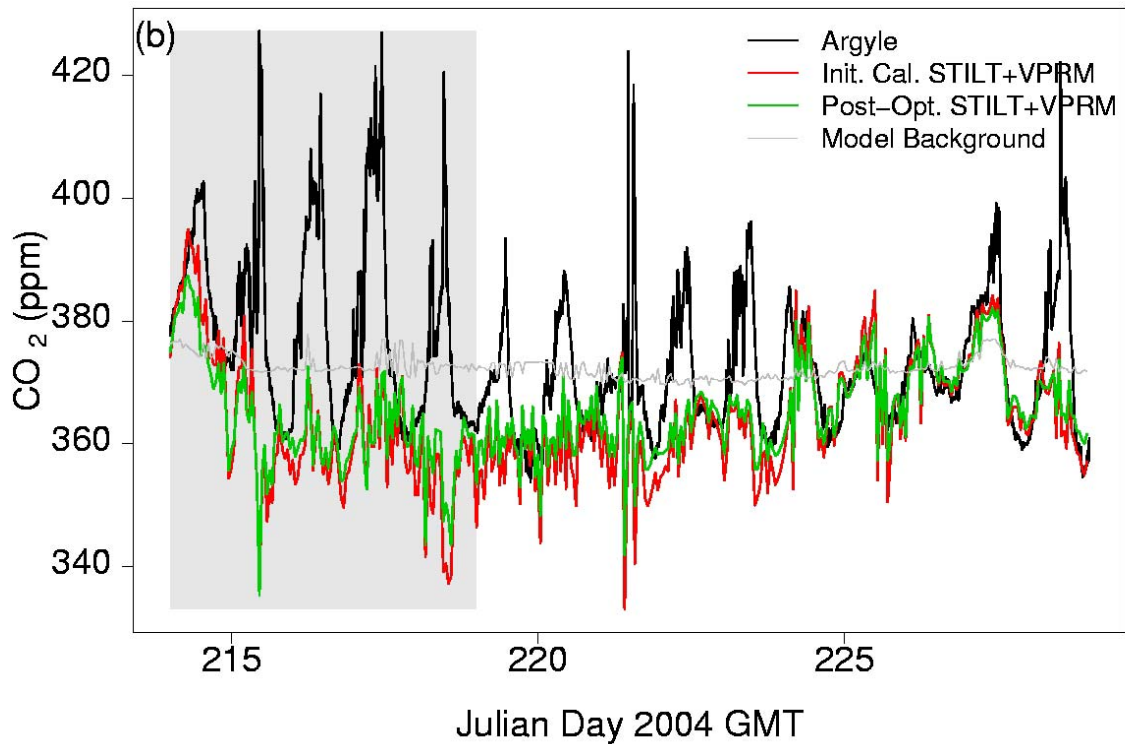


Figure 3.2 – Timeseries of observations from the NOAA CMDL tall tower site (black line) and STILT+VPRM derived hourly CO_2 concentration at the Argyle receptor (red and green lines) point, with advected model background (light grey line) for June 1-15, 2004 (a) and August 1-15, 2004 (b). STILT+VPRM results based on the initial calibration are in red; results with the a posteriori scaling factors from the Bayesian inversion (Section 3.4.4) are in green. Differences in modeled concentration from the background line are the product of VPRM fluxes and STILT-derived influence functions. Hurricane Alex influenced transport during August 1 – 6, 2004. This time period is shaded and not included in the Bayesian Inversion.

Due to limitations of the meteorological driver (EDAS), STILT has difficulty accurately reproducing transport on stable nights. This is manifest in the timeseries by the variable fidelity of STILT+VPRM predictions of the large positive CO_2 concentration excursions in the observations, associated with buildup of CO_2 in the stable nocturnal boundary layer. Significant systematic errors also accrue during periods of convection, when STILT may calculate erroneous transport and footprint fields because EDAS reanalysis fields do not represent convective mass transport. We see this effect as errors

in CO₂ concentration at the receptor point at times when frontal systems are near the receptor (Gerbig et al., 2003b). For example, during the period around 0000 GMT on June 10th, 2004 (Figure 3.2a, Julian day 161), NCEP surface charts and GOES satellite data show a distinct cold frontal passage at Argyle.

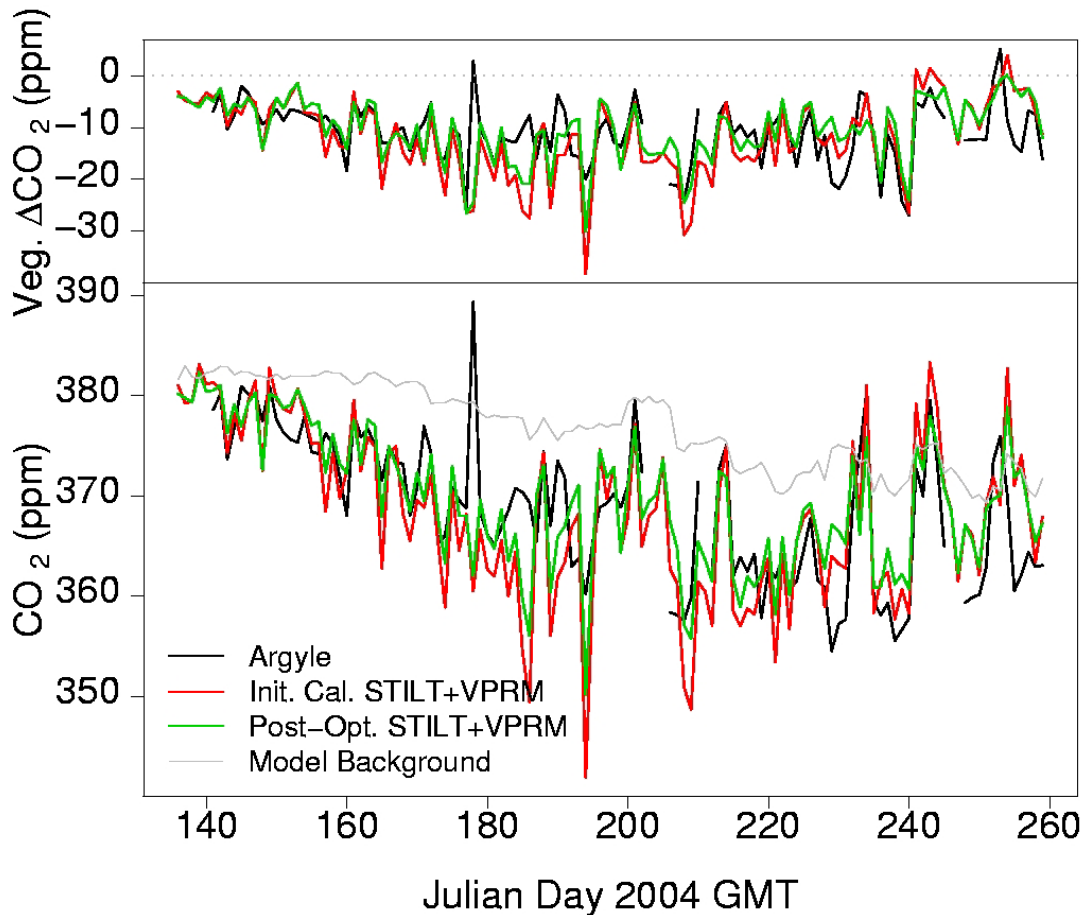


Figure 3.3 – (Top) Timeseries of daily afternoon mean CO_2^{veg} (i.e. ΔCO_2 sum from all vegetation classes) for May 15-June 15, 2004. There is one point per day along each line. STILT+VPRM results based on the initial calibration are in red; results with the a posteriori scaling factors from the Bayesian inversion (Section 3.4.4) are in green. The Argyle signal (black) is determined by subtracting from the observed concentrations the advected background (Section 3.3.2) and advected fossil fuel contribution (Section 3.3.3) determined by STILT+VPRM. (Bottom) Timeseries of mean afternoon observations from Argyle (black line) and corresponding mean STILT+VPRM-derived afternoon CO₂ concentration (red and green lines) point, along with advected model background (grey line) for May 15-June 15, 2004. The fossil fuel contribution is not explicitly shown, but included in the STILT+VPRM calculations of CO₂ concentration.

On seasonal timescales, a period of frequent stormy weather, such as June 19th to July 9th (Figure 3.3, Julian days 170 to 190), shows clear cut deviations from observations. We will in the future use a mass flux scheme (e.g. Grell and Devenyi, 2002) with transport fields from mesoscale models that can output convective mass fluxes (e.g. WRF, RAMS), in the hope of enhancing the power of STILT+VPRM to consistently link regional flux fields to observed concentration values including convective influence (Gerbig et al., 2005).

In Figure 3.2b, the STILT+VPRM does not match the observations during the period from August 1st to August 6th, 2004 (Julian Days 214-219, shown in grey). We attribute this to the inability of the transport model to capture atmospheric transport associated with Hurricane Alex. Alex tracked to the northeast staying a few hundred kilometers offshore, partly out of the EDAS domain. It strengthened to Category 3 as it moved through latitude 40° N on August 4th. This period has been removed from our Bayesian inversion (Section 3.4.4).

3.4.2 Footprint and Vegetation Influence

Two vegetation types dominate summertime influence at Argyle: mixed forest and deciduous forest. They contribute on average at least an order of magnitude greater ΔCO_2 at Argyle during summer 2004 than the other vegetation types (Table 3.1). Wet temperate evergreen forest (Eastern white pine) provides the greatest influence of the remaining classes.

Table 3.1 Mean ΔCO_2 contribution of each VPRM vegetation class to the modeled concentration at Argyle for daytime hours in June, July, and August 2004. The two primary contributors for each month are in boldface type

	Boreal ever- green	Wet temp. ever- green	Dry temp. ever- green	Sub- tropical ever- green	Decid- uous forest	Mixed Forest	Shrub	Savanna	Crop	Grass
Jun	-0.435	-0.512	-0.017	-0.065	-4.99	-5.95	+0.215	-0.046	-0.260	+0.357
Jul	-0.790	-1.06	-0.012	-0.034	-5.48	-9.31	+0.132	-0.029	-0.655	-0.171
Aug	-0.662	-0.475	-0.011	-0.010	-3.46	-7.29	+0.191	-0.049	-0.407	-0.253

Footprint calculations display the principal areas that influence Argyle CO_2 data, mostly located in Maine and Quebec. Figure 3.4 shows the 5-day time-integrated STILT footprint for Argyle averaged over each daytime hour during the period from May 15th to September 15th, 2004. The area coinciding with the average footprint is dominated by deciduous and mixed forest (Figure 3.1) as expected. These are among the ecosystem types for which the VPRM was most effective in capturing seasonal GEE and respiration variations, and where the model performed best in cross-validations (Pathmathevan et al. 2006). The signal from wet temperate evergreens comes from east of Argyle in Nova Scotia, New Brunswick, and easternmost Maine. Unfortunately there is not really a suitable eddy flux site for this biome, and the VPRM had to use Niwot Ridge, a montane forest, as the calibration site. Influence from this biome also coincides with unsettled weather in many cases.

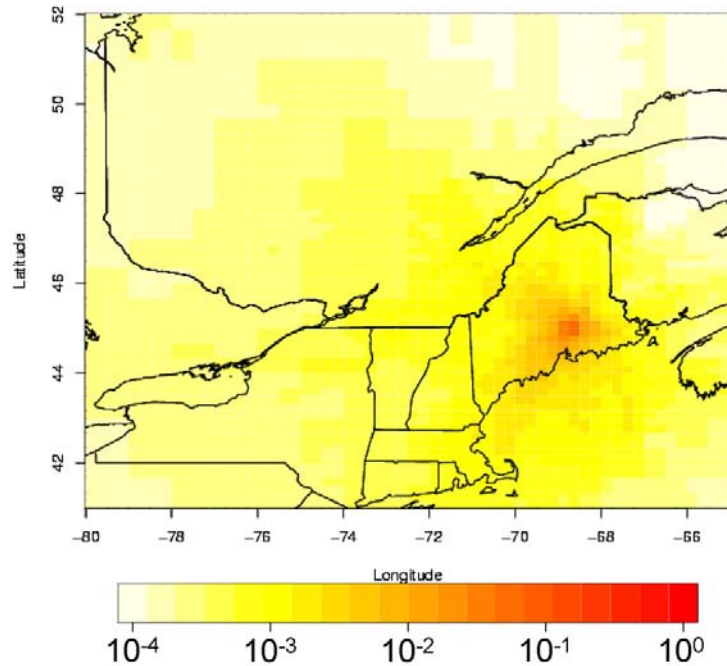


Figure 3.4 – Visualization of the average five-day footprint ($\langle\langle f \rangle\rangle$, see equation 3.2) for Argyle tower for daytime hours during the period May 15 to September 15, 2004. For each hour, $\langle\langle f \rangle\rangle$ is calculated by taking the footprint function and integrating over all areas and all times for five days upstream, and the mean result is shown. Values less than 10^{-5} are not colored.

Fossil fuel influence on Argyle was consistent across the summer. The monthly means for summer are shown in Table 3.2. Fossil fuel influence at Argyle on any given day can vary, depending on whether air arrived at Argyle from relatively rural southern Quebec or from the major cities of Eastern U.S. Aside from synoptic time-scale variability, fossil fuel influence is relatively constant reflecting very large-scale influences far from the site.

Table 3.2: Mean and standard deviation of monthly ΔCO_2 contribution from fossil fuels at Argyle, as calculated by STILT+VPRM

	Mean	Standard Deviation
Jun	2.5	3.1
Jul	3.5	2.9
Aug	3.5	2.7

Monthly average maps of net ecosystem exchange are shown in Figure 3.5, calculated using the VPRM to determine the mean of all the hourly values at each grid square for each month in summer, 2004. Within the region that influences concentration measurements at Argyle tower (see figure 3.4), there is a large increase in uptake from May to June, then a gradual decrease through July and August, corresponding to the seasonal pattern expected for a mid-latitude area dominated by deciduous and mixed forest. Overall, VPRM-derived fluxes appear to capture both the spatial heterogeneity and temporal variations needed to meaningfully assess patterns in regional terrestrial carbon exchange.

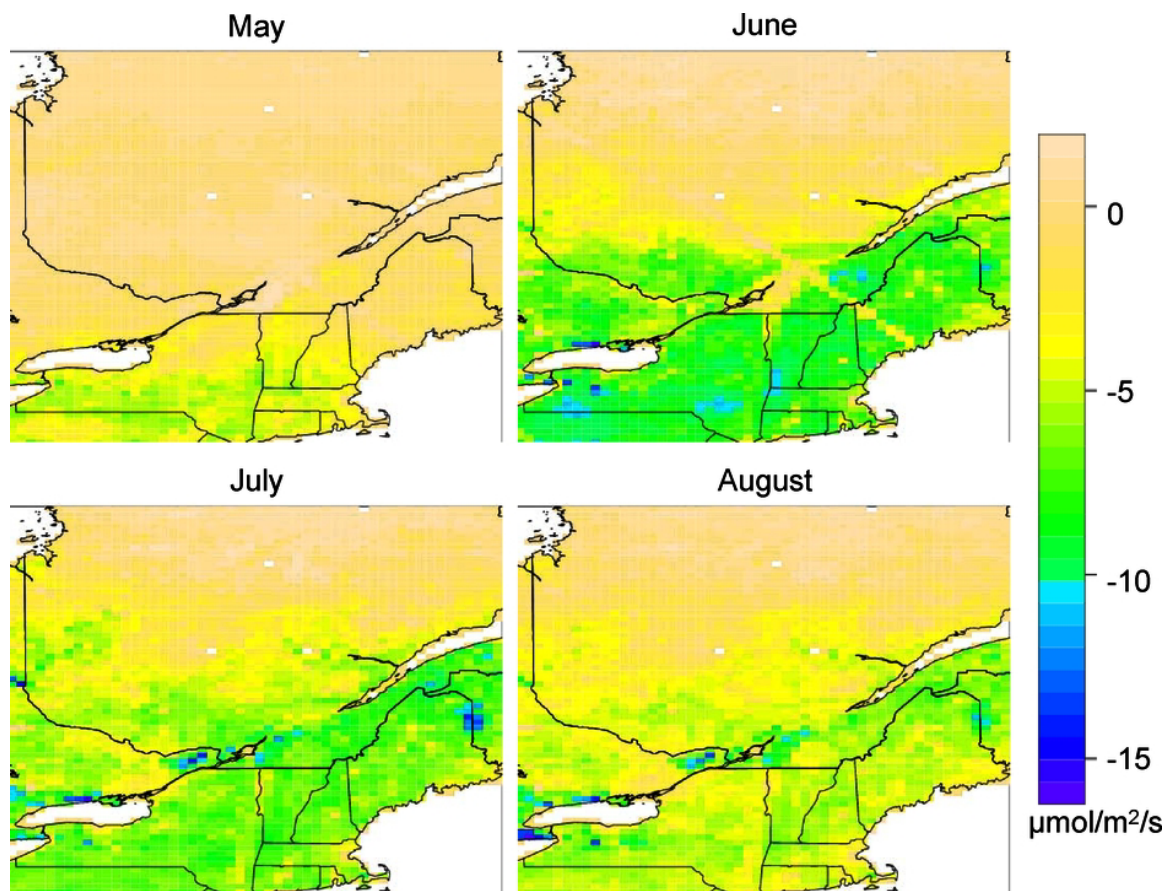


Figure 3.5 – Initially calibrated VPRM calculated mean monthly (all hours) fluxes for May (a), June (b), July (c), and August (d), 2004 in $\mu\text{mol}/\text{m}^2/\text{s}$, based on hourly calculations.

Using the daytime results calculated for the entire summer, we computed average morning concentration values (10am – 1pm Eastern Daylight Time; 1400 – 1700 GMT) and afternoon concentration values (2 pm – 5pm Eastern Daylight Time; 1800—2100 GMT) for each day. We removed from the Argyle data periods with low turbulent mixing (mean friction velocity, $u^* < 0.2$ m/s), to avoid times where the tower is not well coupled to the overlying atmosphere (Lin et al., 2003; Gerbig et al., 2003b). Figure 3.6 compares these averages to Argyle concentration data averaged over the same periods of the day. Averaging over several hours allows reduction of hour-to-hour noise in both measurements and model results, while preserving the signal contained in diurnal patterns that reflect the daily cycle of photosynthetic uptake.

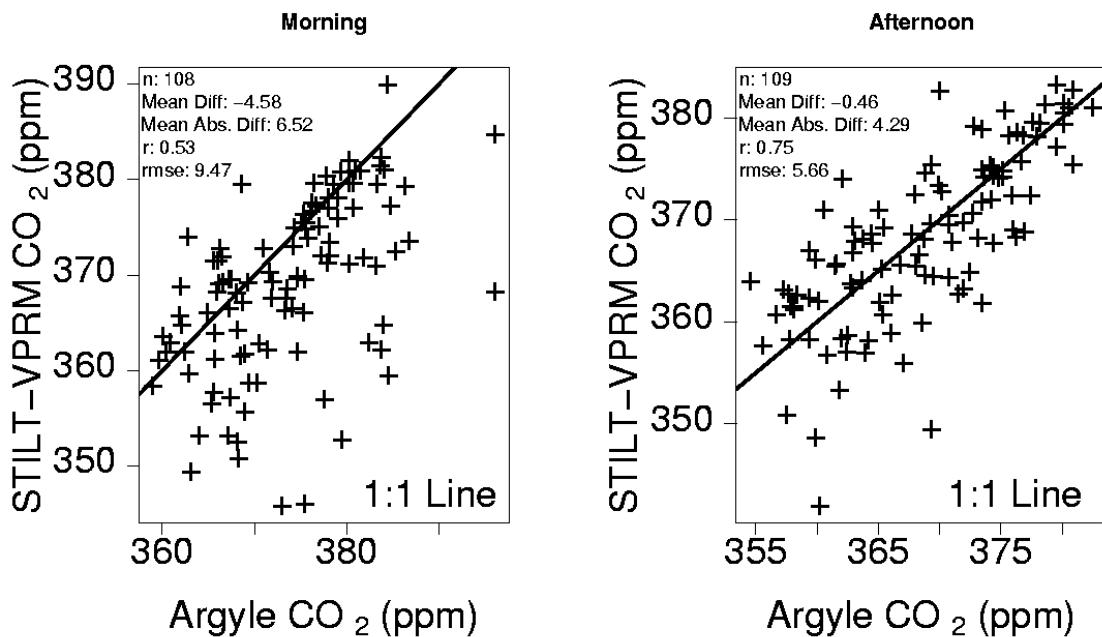


Figure 3.6 – Direct comparison of STILT+VPRM derived concentrations prior to Bayesian optimization vs. Argyle observations for averaged over morning [1400 GMT – 1700 GMT] (a) and afternoon [1800 GMT – 2100 GMT] (b). The performance of the model is best in afternoon, when conditions are most likely to be well-mixed. The 1:1 line is also shown. Periods with consistently low turbulent mixing, indicated by mean friction velocity, u^* , less than 0.2 m/s (seven points in each case) have been eliminated.

STILT+VPRM captures day-to-day variations in CO₂ concentration observed at Argyle somewhat better in the afternoon than in the morning, with root mean square error of 5.66 ppm vs. 9.53 ppm respectively. The mean difference and mean absolute difference in the morning are about the same as the root-mean-square, indicating systematic underestimation of CO₂. The distribution of residuals for the afternoon is more Gaussian with significantly smaller bias. Morning mean observations at Argyle are likely influenced in some cases by residual buildup of CO₂ from the previous night, a locally influenced effect that is insignificant most afternoons. The difference between morning and afternoon values might also indicate errors in the unadjusted VPRM respiration or uptake parameters, particularly in the mixed forest and deciduous forest vegetation surrounding Argyle. More likely, the morning bias reflects the inability of EDAS-40 to adequately capture growth of the planetary boundary layer.

3.4.3 Comparisons with COBRA-Maine Airborne Data

Aircraft data collected during the COBRA-Maine campaign give us valuable information through comparisons with Argyle observations and STILT+VPRM results. Comparisons with tower data allow direct quantification of error distributions (e.g. representation error) needed to perform a Bayesian optimization. Figure 3.7 shows the characteristic pattern during an afternoon cross-section observed traveling eastward across Maine to the coastal region. STILT+VPRM effectively captures the patterns along the cross-section, but the west-to-east gradient is overestimated within the boundary layer and there is a noticeable deviation of the mid-tropospheric values. These differences are a convolution of transport errors, including boundary layer height (especially in the coastal zone), and errors in the VPRM parameters, with a potential minor contribution from

misclassification of vegetation. Differences are also caused by processes not adequately captured within STILT+VPRM framework: global scale and far-field effects on the mid-troposphere, convective redistribution, and vegetation processes (e.g. nutrient cycling, disturbance, hydrological processes) not included in the VPRM. It is clear however that even perfect optimization of the surface flux model could not perfectly match observations due to the strong influence of transport error, e.g. due to errors in the boundary layer height.

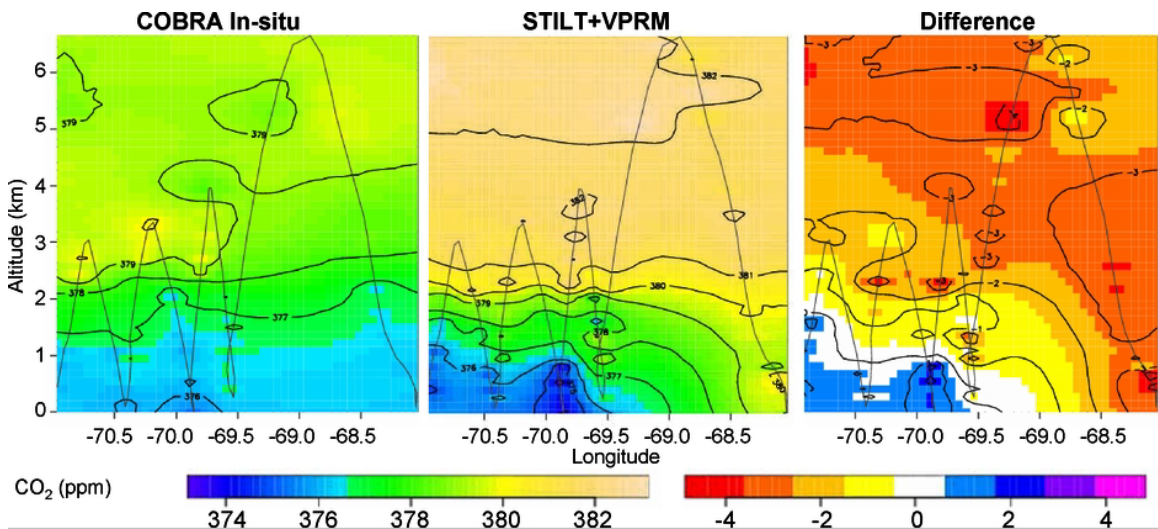


Figure 3.7 – Comparison of COBRA-Maine in-situ CO₂ (ppm) with STILT+VPRM derived CO₂ (ppm) along a flight track that traversed the state of Maine eastward on the afternoon of 11-June-2004. Longitude-altitude cross-sections using a distance-weighted interpolation, with the flight track line in light gray are shown for observations (left), the STILT+VPRM results (center), and the difference between the two (right). The points used in the interpolation were a subset of flight data, with a point for taken when positioned changed by 10km along the horizontal flight track or 20mb in the vertical.

Integration of concentrations to a fixed height may provide a better measure of regional fluxes in the model, since these are sensitive to regional surface fluxes but relatively insensitive to details of regional atmospheric dynamics (*see, for example*, Chou

et al., 2002). In COBRA-Maine, the observed and STILT+VPRM values were typically very close. For example, in Fig. 7, mean CO₂ observed above 2 km was 378.94 versus 381.0 from STILT+VPRM, and below 2 km, 376.4 ppm versus 376.3, respectively. The difference between CO₂ below and above 2 km, a key measure of model performance, was 2.5 ppm observed versus 3.7 ppm modeled, typical of the level of agreement we observed.

Aircraft data allow us to assess directly the representation error incurred by model treatment of measurements at Argyle as the mean in the regional planetary boundary layer, an important prior uncertainty for inclusion within a Bayesian optimization. We expect a small daytime gradient to develop in CO₂ concentration within the boundary layer due to biospheric uptake, potentially leading to a biased underestimation of mean PBL concentrations at the relatively low tower measurement height. Of the over 120 vertical profiles flown during COBRA-Maine within 50 km of Argyle, manual examination of individual profiles of water vapor, potential temperature, CO₂, ozone, and turbulence showed a clearly discernable inversion marking the top of the afternoon mixed layer in 42 cases. For each of those cases, we found the average CO₂ concentration measured in-situ by the aircraft as it vertically traversed the boundary layer and compared it to the value at Argyle tower. The Argyle observations at 107 m underestimated the mean boundary layer CO₂ by 0.89 ppm on average (Figure 3.8). Observations at 25 m underestimated the mean PBL concentration by much more, 1.49 ppm on average. Overall, this represents a relatively small potential source of uncertainty compared to others discussed in Gerbig et al. (2003b). However, to our knowledge, this is the most extensive systematic comparison of tower measurements to mean boundary layer values

obtained by aircraft to date, with many more data points than previous studies (Bakwin et al., 2003). It reinforces that tall towers are less prone to influence from local concentration gradients and more representative of a larger surrounding area than short ones, but systematic differences of order 1 ppm are likely even at tall towers.

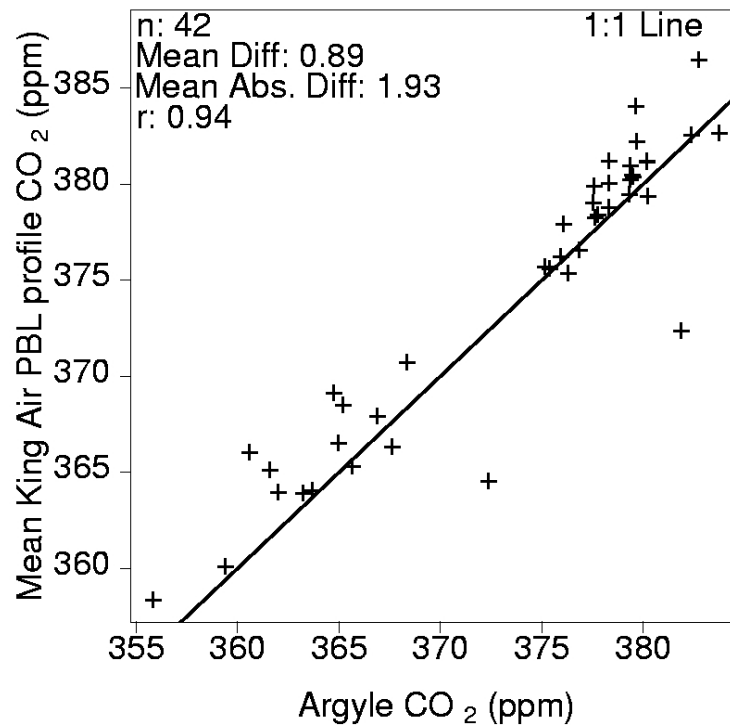


Figure 3.8 – Comparison of CO₂ concentration observed at 107m on the NOAA CMDL Argyle tall tower and mean boundary layer CO₂ concentration, determined from COBRA-Maine airborne data. Each point represents the mean concentration below the top of the mixed layer measured by the aircraft as it ascended or descended through the boundary layer within 50 km of Argyle vs. the mean tower concentration for the same time period. The top of the mixed layer was determined manually from vertical profiles of water vapor, potential temperature, ozone, and turbulence.

Airborne in-situ concentration measurements collected in the free troposphere above the top of the mixed layer are useful in evaluating the advected continental boundary condition value that provides the background upon which the concentration changes due to surface fluxes are imposed. In order to assess potential error in upstream

boundary condition, Gerbig et al. (2003b) evaluated the mean difference between the empirical boundary condition developed from vertical profiles in the Pacific and the accumulated library of corresponding Pacific airborne measurements, obtaining 0.22 ppm, with a standard deviation of 1.15 ppm. Latitudinal gradients in the Pacific boundary condition were not prominent with values around 3 to 4 ppm between 10° N and 72° N at most altitudes throughout 2004. In August and September, the potential bias in our treatment of the boundary condition was as large as 1 ppm.

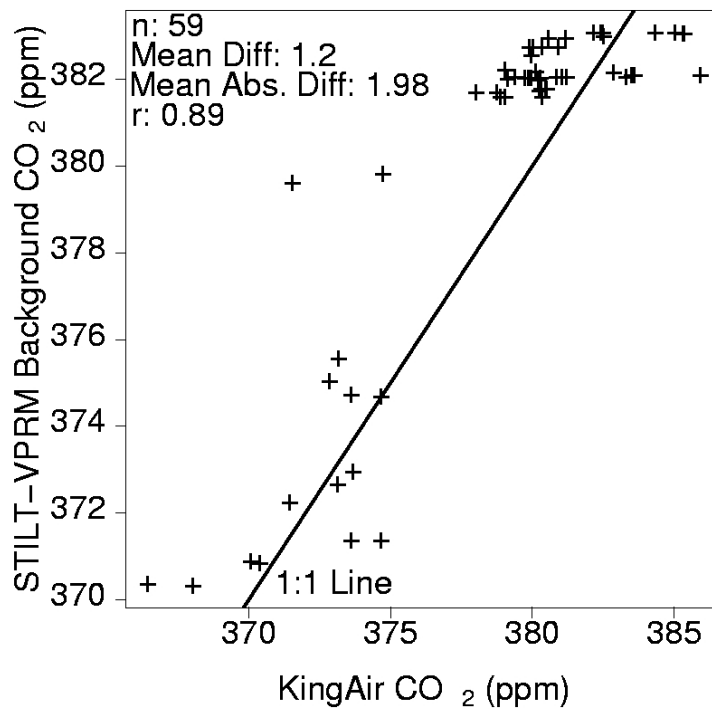


Figure 3.9 – Comparison of mean free troposphere CO₂ concentration determined from COBRA-Maine airborne observations and corresponding background value at Argyle tower, determined from the advected boundary condition in the receptor oriented model (Section 3.3.2). Each point represents one aircraft profile within 50 km of Argyle.

Figure 3.9 shows a comparison of the mean advected boundary condition at Argyle used in STILT+VPRM calculations to in-situ mean free tropospheric (> 3km) CO₂ measured

by the King Air for 59 profiles from COBRA-Maine. The mean difference is 1.2 ppm, which is of the same order as would be expected from the analysis in Gerbig et al. (2003b), and the same order as the tower-PBL gradient. These results are applied to S_{veg} (see Equation 3.13; Section 3.3.7) in Bayesian optimization below.

Two types of errors due to transport contribute most strongly to potential errors in the advected boundary condition. First, because we assume a boundary condition in the central Pacific, the small fraction of particles leaving the STILT domain to north (or south) are given values fit to north (or south) Pacific concentrations, where values in the Arctic or subtropics are needed. These are not available due to the scarcity of observations. Second, because EDAS-40 does not include convective transport, there is the potential for divergence between modeled background and observed free troposphere due to misrepresentation of convective influence.

3.4.4 Bayesian Optimization Incorporating Tower Concentration Observations

The Argyle data set provides a constraint for powerful inversion techniques, such as Bayesian inversion or Ensemble Kalman Filtering to further optimize the VPRM model. Since the VPRM already incorporates knowledge about the functional dependence of carbon exchange through the AmeriFlux eddy-covariance data, STILT+VPRM already goes beyond a straightforward top-down estimation of fluxes. The Bayesian optimization can extend bottom-up extrapolation of eddy correlation fluxes by imposing large-scale constraints from tall tower data. We therefore undertook an inverse analysis below, exploratory in nature, using the single tower data set from Argyle within the STILT+VPRM framework to assess the information available from eddy covariance and tall tower concentration data.

We performed a Bayesian optimization for scaling factors γ and ρ for each vegetation class (Table 3.3). This analysis used 863 daytime hours (excluding hours with missing Argyle data) during the growing season, May 15th to September 15th, 2004. The atmospheric data provide the most information for the mixed and deciduous forest vegetation classes as expected from the STILT footprint in Figure 3.4. In all cases, *a posteriori* scaling factors are relatively close to unity, consistent with the relatively good performance of the input VPRM. Prior to optimization, the root mean square error (RMSE) of STILT+VPRM CO₂ concentrations from the observed concentrations for all daytime hours was 7.31 ppm. Optimization improved the RMSE to 5.79 ppm, a 20% reduction.

Errors in computed concentrations reflect errors in the *a priori* values of γ and ρ for each class, which can in turn be interpreted as errors in the initial calibration factors used to fit the VPRM. These are mixed with errors in the footprint calculation and other model errors. Applying the γ and ρ factors to the STILT+VPRM results shown in Figures 3.2 and 3.3 increases correlation of model results to observations, but changes the overall patterns only slightly. This indicates the prior values (i.e. the initial calibrations to eddy covariance data) carry significant weight in the optimization. Further, deviations are mostly caused by processes not adequately captured within STILT+VPRM framework, especially transport error.

Table 3.3: Bayesian optimization of γ and ρ scalar multipliers for VPRM gross ecosystem exchange and respiration, respectively for 10 vegetation classes using Argyle tower concentration measurements. Constraints were hourly daytime (1400-2100 GMT) CO₂ concentration observations, over 114 days (N=863), computed from STILT-VRPM, May 15 to September 15, 2004. In the a priori case $\gamma=1$ and $\rho=1$

	a priori scaling factor	a posteriori scaling factor	a priori uncertainty	a posteriori uncertainty	% reduction in uncertainty
$\gamma_{\text{boreal evergreen}}$	1	0.96	0.018	0.015	16.7
$\rho_{\text{boreal evergreen}}$	1	0.96	0.112	0.073	34.8
$\gamma_{\text{wet temperate evergreen}}$	1	1.01	0.013	0.011	15.4
$\rho_{\text{wet temperate evergreen}}$	1	1.24	0.060	0.037	38.3
$\gamma_{\text{dry temperate evergreen}}$	1	1.02	0.022	0.022	0.0
$\rho_{\text{dry temperate evergreen}}$	1	0.94	0.072	0.069	4.2
$\gamma_{\text{subtropical evergreen}}$	1	0.96	0.014	0.012	14.3
$\rho_{\text{subtropical evergreen}}$	1	1.21	0.045	0.036	20.0
$\gamma_{\text{deciduous}}$	1	0.71	0.023	0.009	60.9
$\rho_{\text{deciduous}}$	1	0.42	0.344	0.017	95.0
$\gamma_{\text{mixed forest}}$	1	0.67	0.016	0.007	56.3
$\rho_{\text{mixed forest}}$	1	0.79	0.148	0.020	86.5
$\gamma_{\text{shrubland}}$	1	1.00	0.015	0.015	0.0
$\rho_{\text{shrubland}}$	1	0.89	0.068	0.063	7.4
γ_{savanna}	1	0.99	0.015	0.015	0.0
ρ_{savanna}	1	1.02	0.076	0.076	0.0
γ_{cropland}	1	0.86	0.030	0.020	33.3
ρ_{cropland}	1	0.50	0.170	0.052	69.4
$\gamma_{\text{grassland}}$	1	0.92	0.027	0.025	7.4
$\rho_{\text{grassland}}$	1	0.08	0.212	0.148	30.2

Atmospheric concentration data do not provide significant constraints for scaling factors from either dry temperate evergreen or wet temperate evergreen vegetation classes, those that Table 3.1 shows have the next strongest influence on Argyle, after deciduous forest and mixed forest. Within the mixed forest and deciduous forest, atmospheric concentration data provides strong constraints on two scaling factors and only moderate constraints on the other two. Hence, Argyle data alone are insufficient to fully constrain the VPRM model, even where only two vegetation classes have major

influence. In order to fully optimize the VPRM for New England and southern Quebec, additional tower sites and/or inclusion of aircraft data will be needed.

3.5 Conclusions

We have used STILT+VPRM, a model-data assimilation framework with a minimum number of parameters, to estimate terrestrial carbon flux with high temporal resolution on regional to continental scales. Results from the VPRM, using parameters derived from AmeriFlux eddy covariance data, showed good agreement with CO₂ concentrations at Argyle tall tower and in COBRA-Maine aircraft surveys, for simulations in which there was no adjustment of parameters to fit atmospheric concentration data. This result shows that STILT+VPRM is fully representative of the regional-scale, rather than just the local scale. The framework successfully takes eddy flux data from local scales, and derives the emergent functional dependence of flux on environmental conditions to capture surface heterogeneity and to interpret data for carbon fluxes at scales previously inaccessible from global inversions or local-scale eddy covariance measurements. Success of STILT+VPRM hinges on the capability for STILT to link regionally representative point concentration data to upwind sources with high spatiotemporal resolution, plus the capability for the VPRM to capture the rich spatial and temporal complexity of CO₂ fluxes using remote sensing and eddy flux data.

The extremely simple mathematical structure of the VPRM enables efficient optimization of scaling parameters using tall tower or aircraft concentration data. An exploratory Bayesian optimization demonstrated the large amount of information

necessary to reasonably constrain even a relatively simple biosphere model such as the VPRM, as well as the critical importance of transport errors.

Our results imply a conservative approach to estimating the amount of information any single tower within a network can provide for carbon accounting. A network may need a denser distribution of towers than footprint calculations might suggest in order to properly attribute CO₂ changes to different vegetation, because the influences of various vegetation types are commingled by atmospheric transport and thus are not readily separated in an inverse analysis. The Bayesian analysis gives a complete set of constraints, but there is significant weight for the *a priori* fluxes. We do not believe that the need for a dense tower network is an artifact of the STILT analysis, because our Lagrangian framework has very high resolution and low artificial numerical dispersion (Lin et al., 2003), and we can reproduce reasonably well the available data set even from aircraft (see above); it appears to be a basic limitation of inversions based on data from tall towers, even parameter inversions. Aircraft data and/or towers with overlapping footprints in space and vegetation class will be needed to provide reliable regional CO₂ budgets.

Proper quantification of the uncertainty within the model-data fusion framework is as important as the flux estimation itself (Raupach et al., 2005). There are limits on how many parameters any single set of atmospheric data might constrain and there are unavoidable covariances between CO₂ fluxes, weather, and tower footprints. Hence, effective inversion requires an accurate and reliable *a priori* flux models that capture the functional dependence of CO₂ exchange on environmental conditions, such as the calibrated VPRM model presented here.

Chapter 4: Assimilation of regional surface and airborne network observations for CO₂ flux estimates from a receptor oriented modeling framework

4.1 Abstract

We present a counterexample to the current working paradigm of terrestrial CO₂ data assimilation studies, demonstrating a series of cases where a reasonable surface source function is insensitive to optimization because modeled atmospheric transport and boundary conditions introduce errors which the assimilation cannot address, even with a large set of data. The STILT+VPRM framework (Matross et al., 2006) is applied to New England/Southern Quebec region for summer 2004, using atmospheric CO₂ concentration observations from multiple platforms, including aircraft, tall tower, permanent forest sites, air quality monitoring sites and temporary monitoring locations throughout the region. This dense set of observations is used to define an observational tracer boundary condition and determine correlations within the data set, then used in a Bayesian optimization. There is a high amount of redundancy due to spatial and temporal correlation in the observations, which drastically reduces the degrees of freedom in the optimization, emphasizing the need for large amounts of diverse and independent data to constrain even a limited number of parameters. Irreducible representation errors in the source function and in the characterization of the atmosphere render *a posteriori* optimization results which do not appreciably enhance the model's ability to reproduce observed CO₂ concentrations, despite a moderate reduction of the optimization cost function. The altitude gradient in inversion results using boundary layer airborne data

suggests the unexplained variance of CO₂ concentration near the surface caused by unrepresented boundary layer dynamics prevents assimilation of surface based atmospheric CO₂ data from constraining surface fluxes.

4.2 Introduction

Recent work to understand terrestrial carbon budgets has led to the emergence and continuing progression of regional atmospheric CO₂ data assimilation techniques, creating a need evaluate the current paradigm and better characterize what information various observations can provide to optimization methods. There is a rich literature calculating distributions of sources and sinks of CO₂ based on global inverse modeling of CO₂ concentration data from remote stations within the global monitoring network (e.g. Tans et al., 1990 Gurney et al., 2002; Gurney et al., 2004). Oceanic station observations, primarily free from the day-to-day variation inherent in terrestrial continental measurements have proven most robust in inversion for large scale monthly to yearly flux variations (Patra et al., 2006). In parallel with global inversions of remote station data, there have been efforts to link biophysical flux models to eddy covariance measurements (Law et al., 2002), designed to capitalize on the information such observations provide on temporal variability and environmental controls of CO₂ exchange between the atmosphere and terrestrial ecosystems (Rastetter et al., 2003; Baldocchi, 2003). It has proven difficult to reliably scale up eddy-flux observations from their localized footprints or to test regional flux models developed using micrometeorological measurements (Medlyn et al., 2005; Hollinger and Richardson, 2005).

Data assimilation techniques have sought to fulfill the need to quantify regional CO₂ fluxes by taking full advantage of the continental atmospheric concentration signal largely disregarded in global inversions and using it as a constraint to optimize parameters in biophysical flux models of varying complexity (Matross et al. 2006; Gerbig et al., 2003b; Nicholls et al., 2004). Attention has necessarily been focused on developing biophysical models and coupled biosphere-atmosphere frameworks capable of simulating diurnal, synoptic, and seasonal timescale variations inherent in terrestrial CO₂ observations (Denning et al., 2003; Pathmathevan et al., 2006). Further efforts have been directed towards developing a set of rigorous optimization techniques in the context of CO₂ data assimilation, including Bayesian inversion (Gerbig et al., 2003; Michalak et al., 2005), geostatistical approaches (Michalak et al., 2004), Kalman smoothers (Bruhwiler et al., 2005), and ensemble approaches (Peters et al., 2005). Data assimilation methodology in the context of terrestrial CO₂ fluxes has steadily improved enough to consider limitations imposed not by the computational techniques themselves, but by the properties of the inversion structure and by the information contained within observations being assimilated.

Much of the recent work employing CO₂ model-data fusion has focused on interpreting modeled surface flux source functions using available atmospheric concentration data from tall tower observations (e.g. Matross et al., 2006, Nicholls et al., 2004). This paper presents a Bayesian inversion study using a data assimilation framework typical of the ones currently being developed and incorporating a large amount of different types of data from a regional “network” of surface and airborne observations taken during summer 2004 in the Northeast United States and central

Quebec. We take advantage of the large number of measurements during this period to include a detailed analysis of correlation within the data, create an observation-based boundary condition, and define diagonal and off-diagonal elements of the error covariance matrix. By using a diverse set of observations, we are able to quantify the relative constraint added to a source function by assimilation of different combinations of atmospheric concentration data. More importantly, combining airborne observations with data from multiple surface sites creates an integrated context in which to fully evaluate limitations of the assimilation framework which might be impossible to discern using only a single tower.

Our inversion results provide a counter-example to usual paradigm of terrestrial CO₂ data assimilation. Despite using an a priori surface flux model which can reliably simulate the observations and a large amount of input data with high signal-to-noise ratio, the optimization cost function is insensitive to the source function due to strong errors introduced by atmospheric transport, about which an input set of CO₂ data can provide minimal information. Attempts to assimilate tower observations are shown to be limited in large part by errors at the boundary of the transport fields and tracer concentration boundary fields. Although fitting a new set of boundary conditions may help ameliorate such errors, the persistent altitude gradient in model error is not improved through assimilation boundary layer data airborne concentration data. Large variances in near surface CO₂ concentration remain unexplained by the combined transport and surface flux model, suggesting that the inability of the model to properly represent both dynamical transport and boundary layer processes prevents improvement of model

performance through optimization of surface flux parameters using tower CO₂ concentration observations.

4.3 Data and Methods

4.3.1 Data for assimilation

The observations to be assimilated in this study come from COBRA-Maine, an intensive field study which took place primarily in New England and southern Quebec from May to August, 2004 (Lin et al., 2006; Matross et al., 2006). The focal point of the COBRA-Maine campaign dataset is 200 hours of 1-Hz in-situ airborne data collected with the University of Wyoming King Air and coordinated around a regional set (Figure 4.1) of surface concentration measurement sites. Surface observations centered on the NOAA Earth Systems Research Laboratory Global Monitoring Division Argyle Tall Tower, set up in late 2003 as part of COBRA-Maine (Matross et al., 2006). Airborne data include 1-Hz CO₂, CO, and O₃ concentrations and a full suite of meteorological variables. Only airborne data from the second COBRA-Maine deployment, spanning July 14th to August 16th, 2004 are utilized here. The airborne data have been partitioned between observations taken in the boundary layer and observations taken in the free troposphere. It is assumed the vegetation signal is significantly stronger in the boundary layer, so only those values are used to constrain the surface flux model; free troposphere values can be used to help constrain the boundary condition.

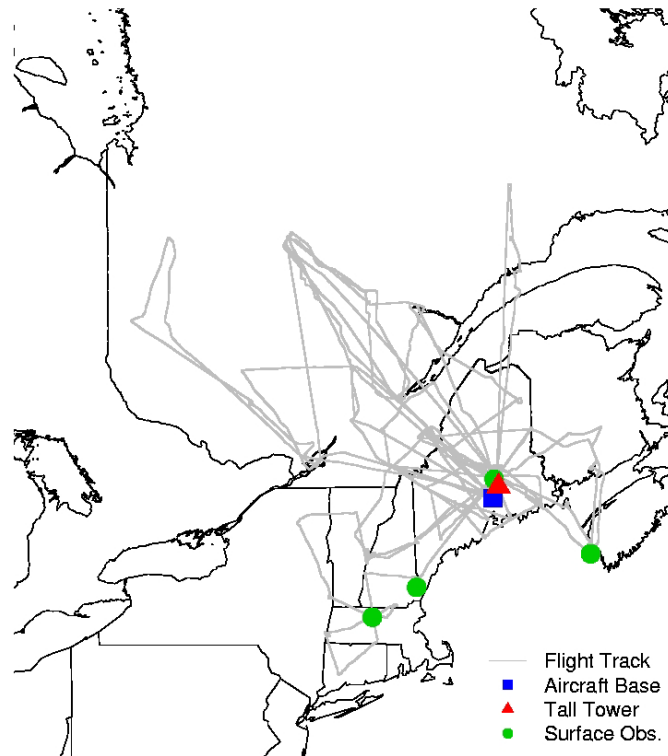


Figure 4.1 – Loose “network” of CO₂ observations available from surface and airborne locations during the COBRA-Maine deployment in July and August, 2004.

In addition to Argyle (45.03°N, 68.68° W, 107 m), CO₂ concentration observations have been assembled from continuous monitoring locations throughout the region including Harvard Forest (42.53°N, 72.17° W, 30 m), Howland Forest (45.20°N, 68.74° W, 27 m) (D. Hollinger, personal communication), and the University of New Hampshire Airmap Thompson Farm site (43.11°N, 70.95° W, 30 m) (<http://airmap.unh.edu/DownloadData>; P. Beckman, personal communication), as well as a temporary station set up by University of California, Berkeley at Chebogue Point, Nova Scotia (43.75°N, 66.12° W, ~10 m) for the Intercontinental Chemical Transport Experiment - North America (A. Goldstein, personal communication). One goal of the airborne flights was to fly by Argyle and Howland Forest as many times as possible, and make occasional visits to Harvard Forest and Chebogue Point, creating nodes in the flight

tracks. Taken together the airborne and surface data comprise a regional network of concentration observations with extensive horizontal and vertical coverage across New England and Southern Quebec during summer 2004. The WLEF tall tower (45.95° N, 90.27° W; multiple levels to 396m) (Bakwin et al. 1998) in central Wisconsin was an additional surface point frequented by COBRA-Maine flights transiting back and forth between the aircraft home base in Wyoming and the operational base in Maine. Hourly average values were calculated for all surface locations.

4.3.2 STILT+VPRM Receptor Oriented Modeling Framework

We utilize the STILT + VPRM receptor-oriented modeling framework developed by Matross et al. (2006), which couples an atmospheric transport model with high spatio-temporal resolution, the Stochastic Time Inverted Lagrangian Transport (STILT) model (Lin et al., 2003), to a diagnostic CO₂ flux model with a minimum number of parameters (1-3 per vegetation class) driven by remote sensing and weather data, the Vegetation Photosynthesis and Respiration Model (VPRM) (Pathmathevan et al., 2006).

4.3.2.1 STILT Adjoint Transport Model

STILT is analogous to the adjoint of an Eulerian transport model, designed to calculate footprints representing the sensitivity of the mixing ratio at a receptor location to a given surface flux (Errico, 1997). A footprint is defined as the influence of upstream surface sources on the composition air at a particular measurement point and comes from computing transport of an ensemble of particles representing air parcels backward in time using winds and turbulence statistics from a high-resolution meteorological assimilation.

STILT links the local concentration $C(\mathbf{x}_r, t_r)$ of a conserved tracer, measured at a receptor location \mathbf{x}_r at time t_r , to the surface sources S for the tracer emitted at upstream locations \mathbf{x} at prior time t , by computing the influence function $I(\mathbf{x}_r, t_r | \mathbf{x}, t)$ (Lin et al., 2003) through Equation 4.1.

$$C(\mathbf{x}_r, t_r) = \int_{t_0}^{t_r} dt \int_V d^3x I(\mathbf{x}_r, t_r | \mathbf{x}, t) S(\mathbf{x}, t) + \int_V d^3x I(\mathbf{x}_r, t_r | \mathbf{x}, t_0) C(\mathbf{x}, t_0) \quad (4.1)$$

The first term in Equation 4.1 represents ΔCO_2 at the receptor due to surface sources in domain V between time t_0 and t_r . The second term in Equation 4.1 is the advected contribution from a boundary tracer field. STILT represents surface fluxes as volume sources distributed from the surface through a mixing height h . Particles are used to define the influence function $I(\mathbf{x}_r, t_r | \mathbf{x}, t)$ through Equation 4.2 where $\rho(\mathbf{x}_r, t_r | \mathbf{x}, t)$ is the density of particles at (\mathbf{x}, t) which were transported backward in time from the receptor (\mathbf{x}_r, t_r) , and influence is normalized by the total number of particles, N_{tot} ,

$$I(\mathbf{x}_r, t_r | \mathbf{x}, t) = \frac{\rho(\mathbf{x}_r, t_r | \mathbf{x}, t)}{N_{\text{tot}}} = \frac{1}{N_{\text{tot}}} \sum_{p=1}^{N_{\text{tot}}} \delta(\mathbf{x}_p(t) - \mathbf{x}) \quad (4.2)$$

The delta function in Equation 4.2 denotes the presence or absence of particle p at location \mathbf{x} . The time- and volume-integrated influence function for a receptor point is most readily calculated using Equation 4.3, which tallies the total amount of time each particle p spends in a volume element v over time step m ,

$$\int_t^{t+\Delta t} dt \int_V dV I(\mathbf{x}_r, t_r | \mathbf{x}, t) = \int_t^{t+\Delta t} dt \int_V dV \frac{\rho(\mathbf{x}_r, t_r | \mathbf{x}, t)}{N_{\text{tot}}} = \frac{1}{N_{\text{tot}}} \sum_{p=1}^{N_{\text{tot}}} \Delta t_{p,m,v} \quad (4.3)$$

Equation 4.3 creates a source-receptor matrix to directly link upstream sources and receptor concentrations through Equation 4.1.

Lin et al. (2003) recast the first term in Equation 4.1 using Equation 4.4, which incorporates a surface flux $F(\mathbf{x},t)$ and a footprint element f , which is mathematically defined in Equation 4.5.

$$\Delta C(\mathbf{x}_r, t_r) = \int_{t_0}^{t_r} dt \int_A d^2x f(\mathbf{x}_r, t_r | \mathbf{x}, t) F(\mathbf{x}, t) \quad (4.4)$$

The footprint f is derived from the local density of particles by counting the number in surface-influenced boxes and determining the amount of time each particle spends in each surface volume element during each time step.

$$f = \int_0^h dz I(\mathbf{x}_r, t_r | \mathbf{x}, t) \times m_{\text{air}} / (h \rho_{\text{air}}) \quad (4.5)$$

The value of the footprint calculation depends on the initial column height, h , below which turbulent mixing is strong enough to mix the surface signal. STILT calculates the height of the planetary boundary layer based on a modified Richardson number method (Lin et. al., 2003) and h is determined as a fraction of that value. Gerbig et al. (2003b) showed that f is largely independent of h across a wide range of fractions; $h = 1/2$ is used here.

As currently implemented, the transport fields to drive STILT can come from operational global forecast or reanalysis products (e.g. Eta Data Assimilation System (EDAS), Nested Grid Model (NGM), European Center for Medium-range Weather Forecast (ECMWF) reanalysis) or from mesoscale models run specifically for periods and domains of interest (e.g. Regional Atmospheric Modeling System (RAMS), Weather Research and Forecasting model (WRF)). A stochastic Markov chain is used to represent

sub-gridscale turbulence. STILT can explicitly model convection, e.g. in convective storms, if the driver provides convective mass fluxes.

4.3.2.2 Fossil Fuel Inventory

For CO₂, the surface flux function $F(\mathbf{x},t)$ in Equation 4.4 is the sum of fossil fuel emissions from an inventory and fluxes derived from the VPRM. The fossil fuel inventory is unchanged from Gerbig et al. (2003b). Emissions of CO₂ from fossil fuel, cement production, and gas flaring come from the 1° x 1° database compiled by Marland et al. (1997), with methodology described by Andres et al. (1996). A linear extrapolation is applied, propagating the trend between 1992 and 1996, and resulting in a 10% total increase in emissions since 1996. Time-of-day and day-of-week scaling factors are applied to account for time-dependence of emission fluxes following Ebel et al. (1997), as described in Gerbig et al. (2003b) and Matross et al. (2006).

4.3.2.3 VPRM CO₂ surface flux model

The VPRM is a data-driven diagnostic biosphere flux model fully described in Pathmathevan et al. (2006). It conceptually partitions sunlight between photosynthetically active vegetation and non-photosynthetic components within the leaf and canopy. Satellite data provide independent information on the spatial and phenological variations of gross primary production using the Enhanced Vegetation Index (EVI) and Land Surface Water Index (LSWI), both from MODIS-Terra. Model parameters are initially determined through fitting to eddy covariance data from AmeriFlux sites. The model uses temperature and incident solar radiation from retrievals based on data from the North

American Land Data Assimilation System (NLDAS; <http://ldas.gsfc.nasa.gov/>, Mitchell, et al., 2003). Net flux is computed every hour on a grid of $1/4^\circ$ longitude by $1/6^\circ$ latitude.

The VPRM bins the GLCC 2.0 1-km resolution vegetation inventory (Loveland et al., 2000; <http://edcns17.cr.usgs.gov/glcc/>) into twelve classes (eleven vegetation + one flux neutral class) and calculates net ecosystem exchange (NEE) of CO_2 for each vegetation class in each grid square separately, scaled by vegetation fraction. NEE is the sum of two model terms: a light-dependent term, identified with canopy photosynthesis (GEE), and a temperature-dependent term identified with ecosystem respiration (R). GEE, as calculated in Equation 4.6, is assumed to be a function of shortwave incident flux (SW) and the observed Enhanced Vegetation Index (EVI; Huete et al., 1997).

$$\text{GEE} = \lambda \times S_c \times \text{SW} \times \text{EVI}, \quad (4.6)$$

S_c in Equation 4.6 is the product of several scalar functions described fully in Pathmathevan et al. (2006) and Matross et al. (2006). These functions are defined as needed for individual vegetation classes and scale GEE based on variations of light, temperature and water in order to accommodate the large range of light- and water-utilization strategies observed in nature using as inputs MODIS reflectances and NLDAS fields. In the initial calibration of the VPRM to eddy covariance data, GEE is multiplied by an adjustable parameter (λ) for each vegetation type, representing the overall light use efficiency of the ecosystem.

The VPRM utilizes a linear formulation for respiration (R), as calculated in Equation 4.7. R is a function of a second calibration factor (α) that captures the

dependence of respiration on air temperature, when temperatures are above a minimum temperature T_{rmin} , and an additional calibration parameter (β) represents the basal respiration rate (e.g. during winter when $T < T_{\text{rmin}}$) for a given vegetation type.

$$\begin{aligned}
 R &= \alpha \times T + \beta && \{T > T_{\text{rmin}}\} \\
 R &= \alpha \times T_{\text{rmin}} + \beta && \{T \leq T_{\text{rmin}}\}
 \end{aligned}
 \tag{4.7}$$

The sets of three scaling parameters $\{\lambda, \alpha, \beta\}$ of the VPRM were calibrated for each of eleven vegetation classes with eddy covariance data, using all valid hourly NEE measurements for 1-4 years, at eleven AmeriFlux sites. The parameters were *not* initially adjusted to fit atmospheric concentration constraints, and model results with these 33 calibration parameters (dependent on vegetation class, invariant with time, determined using eddy covariance data) accounted for a large portion (60-80%) of the variance in hourly flux values at each calibration site (Pathmathevan et al., 2006).

4.3.3 Lateral tracer boundary condition

The final component of the receptor-oriented modeling framework is a lateral tracer boundary condition to connect regional simulations to the global background distribution. Gerbig et al. (2003b) utilized a statistical approach based on available long term observations in the Pacific to characterize spatial and temporal dependence of tracer variations, which was updated by Matross et al. (2006) to encompass the year 2004. The boundary condition for North America is imposed at 145° W, representing tracer concentrations over the mid-Pacific ocean before air parcels enter the dominant westerly

flow over North America. It was calculated by using 20 years of airborne observations from various campaigns in the Pacific to fit a set of Green's functions which propagate surface observations upward in space, then using the long term Pacific station observations as the input to the fitted Green's functions to create a timeseries of latitude-altitude cross-sections over time. STILT particles are given value from the time-latitude-altitude bin where they cross 145° W, usually after being transported back for roughly six days from receptor points in the eastern U.S. (Gerbig et al., 2003b).

COBRA-Maine airborne observations from the free troposphere represent a natural way to test and re-align the statistical boundary condition, hereafter referred to as the "Gerbig boundary condition." Unlike observations in the planetary boundary layer, measurements in free troposphere can reasonably be assumed to have minimal surface influence, representing a ready test of model boundary conditions for a chemically passive tracer such as CO_2 . To verify and realign the STILT+VPRM boundary condition, free troposphere (> 3 km) flight locations from COBRA-Maine regional and transit flights were sampled every 10 km horizontally, and 20-second average values taken around those 893 points. STILT was run to determine the boundary location for particles from each receptor point and the observation values were aggregated into the same 2.5° latitude by 500 m altitude bins as the Gerbig boundary condition, and initially assumed to have no surface influence. Particles exiting the domain east of 130° W were deemed not have reached the western boundary condition and not included in the comparison. Unfortunately flights were not frequent enough to reliably create weekly temporal resolution, and instead were aggregated for the entire 5-week period of COBRA-Maine observations.

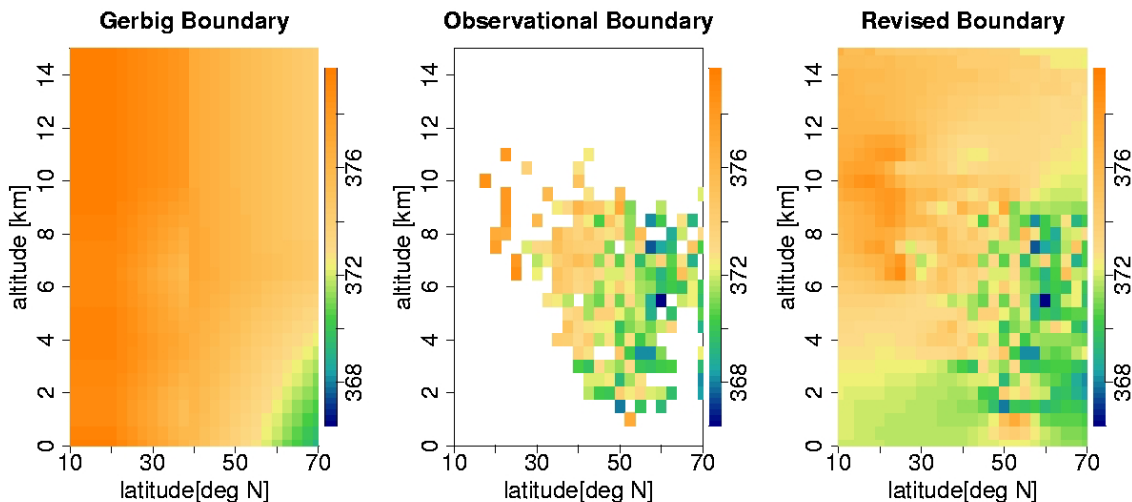


Figure 4.2 – Comparison of the 5-week mean Gerbig boundary condition for July 15th to August 18th, 2004 (left), the COBRA-Maine observational boundary based on free troposphere observations for receptor locations with particles exiting the STILT+VPRM domain west of 130° W (center), and the inverse-distance weighted fit to those values (right).

Figure 4.2 shows cross-sections of western boundary values derived from COBRA-Maine observations (center) compared with the corresponding 5-week mean Gerbig boundary condition (left), and showing the Gerbig boundary condition to generally be a few ppm too high in the lower to middle troposphere over northern midlatitudes where the boundary is most applied. In order to create a revised observation-based western boundary condition applicable to STILT+VPRM calculations for boundary layer receptor points to be used in the data assimilation, we applied an inverse-distance weighted interpolation to the free troposphere observational boundary values to fit the same latitude-altitude cross-section as the Gerbig boundary condition, also shown in Figure 4.2 (right). To account for the seasonal variation in CO₂ concentrations across the summer months, the fitted western boundary condition was extrapolated in time using the daily slope calculated from the 30-year mean June-September CO₂ difference at the

NOAA Global Monitoring Division Mauna Loa observatory

(<http://www.cmdl.noaa.gov/infodata/ftpdata.html>).

In the Gerbig boundary condition, if a particle does not cross 145° W, the time-latitude-altitude condition from 145° W is imposed on it regardless of whether it left the domain to west or not, or even if it stayed inside the domain, a necessary circumstance because surface data and airborne data are far too sparse to create a realistic long-term continuous statistical boundary condition for North America outside of the Pacific. For post-frontal conditions in Maine and southern Quebec, flow is often northerly or northwesterly, resulting in a significant number of particles that exit the STILT+VPRM domain to the north (65° N) rather than to the west. Errors introduced by particles exiting to the north are further compounded by the higher peak-to-trough seasonal differences at in the boundary condition at higher latitudes, which may impose a boundary with temporal amplitude larger than appropriate.

COBRA-Maine flights were more frequent in fair-weather post-frontal conditions, creating a disproportionately large set of free troposphere receptors influenced by northerly or northwesterly flow. We used this large subset of points to create a northern observational boundary condition using the same methodology as the western boundary condition, except aggregating particles exiting the domain north of 55° N into bins of 10° longitude by 1000 m altitude, using larger bins to account for a smaller overall sample set. Figure 4.3 shows the northern observational boundary condition.

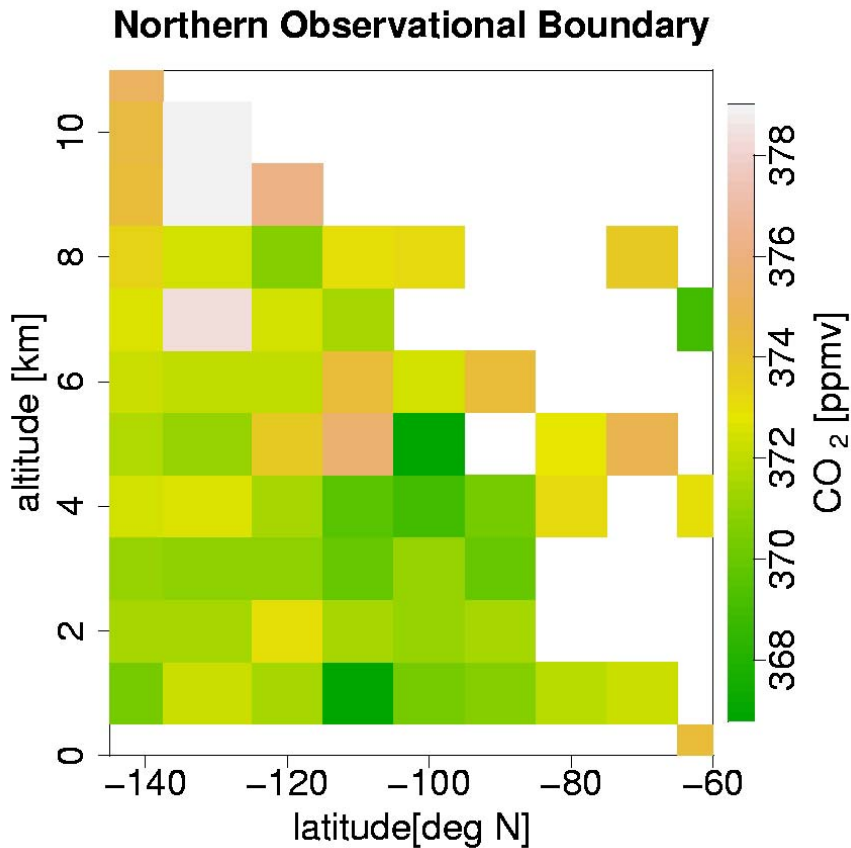


Figure 4.3 – COBRA-Maine observational boundary based on free troposphere observations for receptor locations with particles exiting the STILT+VPRM domain north of 55° N.

Again an inverse-distance weighted interpolation was applied to create a continuous boundary suitable for STILT+VPRM calculations of boundary layer receptor points. The daily slope calculated from the 30-year mean June-September CO₂ difference at Barrow, Alaska was used to extrapolate the fitted boundary condition in time.

Taken together, the fitted observational northern boundary and fitted observational western boundary comprise a new boundary condition, hereafter referred to as the “revised boundary condition.” In the revised boundary condition, particles exiting the domain east of 130° W and north of 50° N are given the northern boundary value corresponding to where and when they leave the domain, and particles exiting the domain

west of 130° W are given the western boundary value corresponding to where and when they leave the domain.

Uncertainty in the revised boundary condition was propagated from a measure of spread within bins, errors associated with neglecting surface influence, and the uncertainty of the extrapolation in time. The average standard deviation (2.01 ppm) was taken as a measure of uncertainty within a given bin of the observational boundary. To account for neglecting surface influences, the fossil fuel inventory and VPRM-calculated surface influence were determined for all receptor points. Because there were some extreme outliers and the median absolute deviation (0.30 ppm) was taken as representing the error associated with not including surface influence for receptor points at altitudes greater than 3 km. The standard deviation of 30-year June-September differences at Mauna Loa (0.62) was used as a measure of error associated with extrapolation in time. Together these aggregate to a total propagated uncertainty of 2.1 ppm in the boundary condition to be applied to STILT+VPRM mixing ratio calculations.

4.3.4 Optimization Setup

4.3.4.1 Receptor a priori concentration

For the STILT + VPRM receptor oriented framework, Equation 4.6 can be split into eleven VPRM vegetation classes to give a fractional footprint as in Equation 4.8, with ω_k representing the fractional coverage of vegetation k ($\omega_{\text{water}} + \sum \omega_k = 1$).

$$f_k = \int_0^h dz I(\mathbf{x}_r, t_r | \mathbf{x}, t) \times m_{\text{air}} / (h \rho_{\text{air}}) \times \omega_k \quad (4.8)$$

Equation 4.9 is used to calculate STILT+VPRM CO₂ atmospheric mixing ratio (χ) for any given receptor time and location, where k indexes the eleven vegetation classes

$$\chi(a\ priori) = \sum_k \int_{t_0}^{t_r} dt \int_A d^2x f_k(\mathbf{x}_r, t_r | \mathbf{x}, t) (GEE_k^{VPRM} + R_k^{VPRM}) + \int_{t_0}^{t_r} dt \int_A d^2x f(\mathbf{x}_r, t_r | \mathbf{x}, t) [FF^{INV}] + BG(\mathbf{x}_r, t_r) \quad (4.9)$$

The first term represents the contribution of VPRM photosynthesis and respiration to the mixing ratio with GEE and R as defined in Equations 4.6 and 4.7 respectively; the second term represents fossil fuel inventory convolved with the total footprint; and the final term is the boundary value advected to the receptor. The first term on the right hand side of Equation 4.9 reiterates the fact that atmospheric concentrations are affected only by net ecosystem exchange, NEE, the sum of GEE and R, rather than the individual components themselves. The boundary term should vary slowly over time and the fossil fuel contribution is on average relatively small for sites away from urban areas (Matross et al., 2006), so most fluctuations are the result of the VPRM surface flux source function which we seek to optimize using atmospheric concentration observations.

Airborne receptor points were sampled from a subset of boundary layer (< 2km) flight locations separated by 20 mb vertically and 20 km horizontally, so that there were about 40 points for each of the flights in the region. At each sample location 20-second average values were determined for data to be used in the inversion. To maximize vertical sampling, COBRA-Maine flights consisted almost entirely of climbs or descents. Assuming a usual climb and descent rate of 5 m/s, a 20-second average will usually cover around 100 m vertically, 40% of the vertical decorrelation length determined in Section 4.3.4.6.

For each surface location, daytime hourly mean values of CO₂ were determined for July 1st to August 31st, 2004. The transport fields used to drive STILT have trouble representing the stable nocturnal boundary layer and the transitions from nighttime to daytime boundary layer regimes, so nighttime hours were excluded from the inversion. With ten hours per day (1300 GMT to 2200 EDT), there were potentially 620 receptor points at each of the five towers. Very stable daytime hours, indicated by values of friction velocity (u^*) less than 0.20 m/s, were also excluded due to the very strong near-surface CO₂ gradients which can sometimes develop under such conditions. Finally, the period from August 2nd to August 6th was excluded from the inversion due to the passing of Hurricane Alex, a category 3 storm which followed a northeastward track a few hundred kilometers offshore the U.S. eastern seaboard. Transport associated with the hurricane is poorly represented in the large-scale global models used at the boundary of the EDAS-40 model, which has a North American domain. Additionally, neither the Gerbig tracer boundary condition nor the revised trace boundary condition adequately characterize the subsiding tropical air entering Maine and Southern Quebec as a result of the hurricane circulation and no reliable way exists to quantify the error associated with such misrepresentation.

A priori concentrations for all receptor points were determined using Equation 4.9. Both the Gerbig boundary condition and the revised boundary condition were utilized in separate cases and model results from either case could be used in the inversion. STILT was driven by EDAS-40 transport fields, while the VPRM was driven by NLDAS temperature and radiation fields in addition to MODIS EVI and LSWI. Additionally, a short run for comparison of a priori results from different meteorological

drivers was conducted for July 1st to July 27th with Argyle tower as the receptor point using the mesoscale Regional Atmospheric Modeling System – Brazilian version (BRAMS) (Camargo and Silva Dias, 2000; Sánchez-Ccoyllo and Andrade, 2002) to drive STILT. BRAMS represents an alternative mesoscale meteorological driver with the added capability to include convective mass fluxes in STILT calculations.

4.3.4.2 Additive optimization factor

In order to constrain the VPRM fluxes using the link to COBRA-Maine airborne and surface atmospheric concentration data, we performed a Bayesian optimization (Rodgers, 2000) with a single adjustable parameter d for each vegetation class, which is additive to GEE and R in calculating net ecosystem exchange.

$$NEE = GEE + R + d \quad (4.10)$$

In this case GEE and R are computed from Equations 4.6 and 4.7 respectively. Because the *a priori* model ($d = 0$ for all vegetation classes) has assimilated a large volume of eddy covariance information through the VPRM calibration factors (λ , α , β) but no atmospheric concentration information, non-zero *a posteriori* values of d encapsulate the deviation between local-scale carbon fluxes calibrated against eddy covariance measurements and regional-scale carbon fluxes constrained against atmospheric CO₂ observations. The factor is then added as a term in Equation 4.9 to complete the calculation of *a posteriori* receptor concentration calculation,

$$\begin{aligned}
\chi(a\text{ posteriori}) = & \sum_k \int_{t_0}^{t_r} dt \int_A d^2x f_k(\mathbf{x}_r, t_r | \mathbf{x}, t) (\text{GEE}_k^{\text{VPRM}} + \text{R}_k^{\text{VPRM}}) + \\
& \sum_k \int_{t_0}^{t_r} dt \int_A d^2x f_k(\mathbf{x}_r, t_r | \mathbf{x}, t) d_k + \int_{t_0}^{t_r} dt \int_A d^2x f(\mathbf{x}_r, t_r | \mathbf{x}, t) \text{FF}^{\text{INV}} \\
& + \text{BG}(\mathbf{x}_r, t_r)
\end{aligned} \tag{4.11}$$

Using a set of additive, rather than multiplicative, parameters is necessitated by the by the lack of independent information about GEE and R in the observations due to strong correlation between the two. Gerbig et al. (2003b) successfully utilized multiplicative factors for GEE and R in a greatly simplified precursor to the VPRM, but the source function is too simple to be realistic for hourly fluxes. Matross et al. (2006) utilized multiplicative factors for GEE and R in the VPRM in an exploratory optimization, but the result was characteristic of an overfit case. Many of the processes that drive variation in photosynthetic uptake (GEE) and respiration (R) at the landscape scale are either the same (e.g. temperature) or are highly correlated with one another (e.g. temperature and radiation; vegetation stature). Therefore, it is extremely difficult to separate signatures of GEE and R from daytime concentration observations.

A number of studies have determined R from nighttime flux observations and extrapolated to the daytime to separate GEE (e.g. Falge et al., 2001). However the stable nocturnal boundary layer gives nighttime tower measurements an especially localized footprint, whereas the daytime observations needed for data assimilation must have a regionally integrated signal. Even in a modeling framework with high enough resolution to reliably represent nighttime concentration observations, the unique information in them about R is not regionally representative. Strong correlation between GEE and R suggests a multiplicative factor on their sum, NEE, or a straightforward principal

component analysis may yield a well-constrained result. However, if GEE and R are very close to balance ($NEE \approx 0$), a not uncommon physiological situation, then a multiplicative factor can become unstable in a linear optimization.

4.3.4.3 Bayesian framework

As outlined in Rodgers (2000), the COBRA-Maine atmospheric measurements can be related to the VPRM vegetation signal (ΔCO_2) from each vegetation class through

$$\mathbf{y} = \mathbf{K} \mathbf{\Gamma} + \boldsymbol{\varepsilon} \quad (4.12)$$

where \mathbf{y} ($m \times 1$) is a vector of m measurements, \mathbf{K} ($m \times 11$) is the Jacobian matrix relating the measurement vector to the state vector, $\mathbf{\Gamma}$ (11×1) is the state vector of additive factors (d's), and $\boldsymbol{\varepsilon}$ ($m \times 1$) is an error vector accounting for uncertainties in measurements and modeling framework. As applied here, the measurement vector \mathbf{y} has a single element for each atmospheric measurement, either an hourly tower value or a 20-second average airborne value. Each element in \mathbf{y} is calculated by subtracting from the individual observation the computed contributions at the corresponding model receptor time and location from the advected boundary condition, fossil fuel combustion, and the a priori VPRM signal. The Jacobian matrix \mathbf{K} consists of the summed total influence value from each vegetation class for each measurement.

The optimum posterior estimate of the additive factor d for each vegetation class, based on atmospheric concentration information from airborne or tower observations, is obtained by minimizing the cost function \mathbf{J} using a standard least squares formulation

$$\mathbf{J}(\mathbf{\Gamma}) = (\mathbf{y} - \mathbf{K}\mathbf{\Gamma})^T \mathbf{S}_e^{-1} (\mathbf{y} - \mathbf{K}\mathbf{\Gamma}) + (\mathbf{\Gamma} - \mathbf{\Gamma}_{\text{prior}})^T \mathbf{S}_{\text{prior}}^{-1} (\mathbf{\Gamma} - \mathbf{\Gamma}_{\text{prior}}). \quad (4.13)$$

In Equation 4.13, there are two error covariance matrices, one for the vegetation signals, \mathbf{S}_ε , and one for the prior additive factors, $\mathbf{S}_{\text{prior}}$. The formulations of \mathbf{S}_ε and $\mathbf{S}_{\text{prior}}$ are critical to defining the nature of the inversion and are detailed below.

Posterior estimates of $\mathbf{\Gamma}$, optimally consistent with both atmospheric observations and prior estimates of fluxes from the initial calibration of the VPRM, are obtained by minimizing \mathbf{J} . $\mathbf{\Gamma}_{\text{post}}$ can be calculated using equation 4.14 (Rodgers, 2000).

$$\mathbf{\Gamma}_{\text{post}} = (\mathbf{K}^T \mathbf{S}_\varepsilon^{-1} \mathbf{K} + \mathbf{S}_{\text{prior}}^{-1})^{-1} (\mathbf{K}^T \mathbf{S}_\varepsilon^{-1} \mathbf{y} + \mathbf{S}_{\text{prior}}^{-1} \mathbf{\Gamma}_{\text{prior}}) \quad (4.14)$$

The uncertainty of $\mathbf{\Gamma}_{\text{post}}$ is expressed through a posterior error covariance matrix, \mathbf{S}_{post} , as shown in Equation 4.15.

$$\mathbf{S}_{\text{post}} = (\mathbf{K}^T \mathbf{S}_\varepsilon^{-1} \mathbf{K} + \mathbf{S}_{\text{prior}}^{-1})^{-1} \quad (4.15)$$

Another quantity of significant interest describes of how many useful independent quantities attributable to the state vector $\mathbf{\Gamma}$ there are in a set of measurements – the degrees of freedom for the signal (df_s) – and the number of independent quantities attributed to noise or other factors not explained by the state vector – the degrees of freedom for noise (df_n). As developed here, the expected value at the minimum of the least squares cost function \mathbf{J} is equal to the total degrees of freedom, in turn equal to the number of parameters (Rodgers, 2000). By using Equation 4.13, additive properties of the expected value operator, and the matrix trace operator (\mathbf{Tr}), which takes the sum of diagonal elements of a matrix, explicit definitions for df_s and df_n can be derived using Equations 4.16 and 4.17.

$$df_s = \mathbf{Tr}([\mathbf{K}^T \mathbf{S}_\varepsilon^{-1} \mathbf{K} + \mathbf{S}_{\text{prior}}^{-1}]^{-1} \mathbf{K}^T \mathbf{S}_\varepsilon^{-1} \mathbf{K}) \quad (4.16)$$

$$df_n = \mathbf{Tr}([\mathbf{K}^T \mathbf{S}_\varepsilon^{-1} \mathbf{K} + \mathbf{S}_{\text{prior}}^{-1}]^{-1} \mathbf{S}_{\text{prior}}^{-1}) \quad (4.17)$$

The reader is referred to Rodgers (2000) for complete derivations and further linear transformations to enable more efficient numerical algorithms.

4.3.4.4 Definition of prior parameter uncertainty

S_{prior} (11×11) is the matrix of prior uncertainties in the additive flux factors. The off-diagonal elements of S_{prior} are assumed to be 0, since the calibration of the VPRM does not introduce covariance in errors between vegetation classes. The values of the diagonal elements in S_{prior} for the different vegetation determined through a bootstrap analysis.

For the bootstrap analysis, the additive flux optimization factor d_k can be recast as a deviation from an average value of NEE, D_k , over a representative time period τ ,

$$1/\tau \times \int_{\tau} d\tau (\text{GEE}_k^{\text{VPRM}} + \text{R}_k^{\text{VPRM}}) = D_k + d_k \quad (4.18)$$

We use daily values for D_k ($\tau = 1$ day) to eliminate including the diurnal cycle of NEE, yet still maintain the ability to quantify synoptic variability in the VPRM. To set up the bootstrap, eddy covariance data from the original VPRM vegetation calibration sites were broken into thirty-day bins, and the VPRM parameters ($\lambda_k, \alpha_k, \beta_k$, for 11 vegetation classes) were fit using the same non-linear least squares procedure used by Pathmathevan et al. (2006). The distribution of fit values for each parameter to the various thirty-day data bins quantifies a representation error reflecting the model's inability to perfectly represent the day to day flux variability over a given one or two month span and marks a departure from Pathmathevan et al. (2006). The mean and standard deviation of fitted values for each parameter defines a Gaussian distribution for the bootstrap. The bootstrap analysis consisted of 500 realizations. For each realization, an hourly timeseries of

VPRM fluxes was calculated using MODIS and NLDAS driver inputs at each calibration site by sampling each parameter from its respective Gaussian distribution and used to determine a single long term mean daily value, D_k . The standard deviation of D_k across all 500 realizations is used as an *a priori* uncertainty for d_k in the Bayesian inversion.

Table 4.1 – Bootstrap analysis to determine a priori uncertainty in the additive optimization parameter, d_k , which is assumed to have a priori value of zero for all vegetation classes. The standard deviation of D_k quantifies the spread in the VPRM resulting from representation and calibration error.

Vegetation Class	Length of single-realization timeseries (days)	Mean D_k ($\mu\text{mol}/\text{m}^2/\text{s}$) from all realizations	Standard deviation D_k ($\mu\text{mol}/\text{m}^2/\text{s}$) from all realizations
Boreal evergreen	1599	-0.44	1.05
Wet temperate evergreen	1396	-0.075	1.87
Dry temperate evergreen	1082	1.7	2.86
Sub-tropical evergreen	722	4.2	4.58
Deciduous forest	1400	2.5	3.07
Mixed forest	1392	2.7	2.55
Shrub	1278	-4.7	12.5
Savanna	1090	-0.74	6.18
Croplands	360	1.5	2.89
Grasslands	1085	-6.2	13.2
Peatlands	357	1.1	1.40

4.3.4.5 Definition of the error covariance matrix for measurements

The vegetation error covariance matrix, S_ϵ ($m \times m$) is defined to be the sum of uncertainties in the measurement and various parts of the model and these uncertainties are used as weighting factors within the optimization (Gerbig et al., 2003b),

$$S_\epsilon = S_{\text{veg}} + S_{\text{part}} + S_{\text{aggr}} + S_{\text{ocean}} + S_{\text{eddy}} + S_{\text{transp}}. \quad (4.19)$$

Summation is not the only way to combine the various elements of \mathbf{S}_ϵ , but unlike other simple ways to aggregate several uncertainties together (e.g. multiplication), it maintains the character of off-diagonal elements when they arise in only some of the terms.

$\mathbf{S}_{\text{veg}} (m \times m)$ is the error covariance in the vegetation signal \mathbf{y} in Equation 4.12 (difference of χ_{observed} and χ_{modeled} calculated in Equation 4.9). It is itself the sum of measurement variances from the concentration observations, $\mathbf{S}_{\text{meas}} (m \times m)$, estimated variance in the advected boundary condition, $\mathbf{S}_{\text{boundary}} (m \times m)$, and uncertainty arising from the fossil fuel inventories, $\mathbf{S}_{\text{fossil fuel}} (m \times m)$,

$$\mathbf{S}_{\text{veg}} = \mathbf{S}_{\text{meas}} + \mathbf{S}_{\text{boundary}} + \mathbf{S}_{\text{fossil fuel}}. \quad (4.20)$$

Measurement uncertainty varied by site and is listed in Table 4.2. Uncertainty associated with the boundary condition depended on whether the Gerbig boundary or the revised boundary was applied. For the Gerbig boundary, we used a variance of $(1.15 \text{ ppm})^2$ for errors in the advected boundary condition, as calculated by Gerbig et al. (2003b) and confirmed by Matross et al. (2006). For the revised boundary, we used the total propagated variance of $(2.1 \text{ ppm})^2$ calculated in section 4.3.3. The contribution from fossil fuel combustion was assumed to have an uncertainty of 30% of the signal (Gerbig et al., 2003b). Because 2004 was generally wet in the region and without large fires in the vicinity of any measuring locations, we did not account for any influence biomass burning may have had on observations.

Table 4.2 – Measurement uncertainty in CO₂ concentration observations collected during COBRA-Maine

Site	Measurement Uncertainty (ppm)	Reference
Argyle	0.3	Matross et al. (2006)
Harvard Forest	0.5	J. W. Munger, personal communication
Howland Forest	1	D. Hollinger, personal communication
Chebogue Point	1	A. Goldstein, personal communication
Thompson Farm	4	P. Beckman, personal communication
COBRA-Maine airborne	0.1	Daube et al., (2002)

S_{part} ($m \times m$) represents random error due to particle statistics. All STILT runs for this study were done with 100 particles, so the relative uncertainties for STILT simulations for mixed layer receptor points derived by Gerbig et al. (2003a) can be used. Diagonal elements of S_{part} were determined by finding 13% of the modeled *a priori* vegetation signal for each receptor and squaring it.

S_{aggr} ($m \times m$) represents the error due to aggregation of fluxes into large finite regions, with diagonal elements estimated as in Gerbig et al. (2003b) to be $(3 \text{ ppm})^2$. Similarly, the error due to neglecting oceanic fluxes, S_{ocean} ($m \times m$), is taken directly from Gerbig et al. (2003b) as a reasonable upper limit of what those fluxes might have contributed. The upper limit of oceanic CO₂ fluxes is assumed to be $0.1 \mu\text{mol}/\text{m}^2/\text{s}$ and diagonal elements of S_{ocean} are the square of oceanic influence for each receptor times multiplied by that value.

S_{eddy} ($m \times m$) is the error due to unresolved eddies and is treated differently for airborne points, tall tower points, and other surface points. For airborne data, the methodology of Gerbig et al. (2003b) is used. Flights are broken down into a series of ascending and descending profiles and the variance from boundary layer observations within each profile computed. The variance for the profile corresponding to the receptor

point is inserted into S_{eddy} at the appropriate diagonal location. Analogous methodology from Matross et al. (2006) is used for all the surface sites, relying on a comparison between concentration measurements at Argyle and simultaneous boundary layer profiles taken in the immediate vicinity during COBRA-Maine. The difference between Argyle concentrations and mean concentrations within the mixed layer nearby are determined for each profile, and the variance across all the profiles used for the diagonal elements for S_{eddy} . At receptor points associated with the tall tower variance from the 107 m measurement level $(1.6 \text{ ppm})^2$ is used, while the variance from the 25 m measurement level $(1.9 \text{ ppm})^2$ is used for the other towers.

S_{transp} represents the influence of error in modeled height of the mixed layer (Gerbig et al., 2003b). The COBRA-Maine airborne dataset consists of over 900 vertical profiles. We created profile plots of temperature, potential temperature, turbulence, CO_2 , CO , O_3 , and water vapor for each ascent and descent and were able to manually discern a boundary layer mixing height in 600 cases. To translate this to an uncertainty value, we determined the variance in relative differences between height of the mixed layer in the EDAS-40 reanalysis fields used to drive STILT particles and manual mixed layer height (mean = 0, standard deviation = 0.47). This variance in the relative differences was multiplied by the *a priori* modeled vegetation signal (Equation 4.9) to create the diagonal elements of S_{transp} .

4.3.4.6 Spatial and temporal correlation within the dataset

Simple forms of the error covariance matrixes are often used in applying the Bayesian formalism, consisting of just the diagonal elements given above. But this

approach neglects spatial and temporal correlations that may be very important. Because \mathbf{S}_ϵ serves as a weighting function, a more rigorous treatment requires that temporal and/or spatial correlations within the dataset be included with off-diagonal elements, de-weighting observations that give redundant information. Rigorously including off-diagonal elements to the error covariance matrix is especially important when assimilating a combination of airborne and multi-site surface data. We assume that errors in the advected boundary condition ($\mathbf{S}_{\text{boundary}}$), the modeled mixed layer height ($\mathbf{S}_{\text{transp}}$) and aggregation errors (\mathbf{S}_{aggr}) will exhibit temporal and spatial correlations. Uncertainties due to unresolved eddies (\mathbf{S}_{eddy}), STILT particle motions (\mathbf{S}_{part}), measurement variance (\mathbf{S}_{meas}) and fossil fuel combustion ($\mathbf{S}_{\text{fossil fuel}}$) are assumed to be random and uncorrelated between observation points and contain no non-zero off-diagonal elements. Error from not including ocean CO_2 ($\mathbf{S}_{\text{ocean}}$) fluxes might be correlated between points, but in practice, the contribution of this term to the error covariance matrix is small enough in magnitude to render off-diagonal elements negligible.

Tower data were assumed to have exponentially decaying covariances with increasing time lags, with decorrelation timescale determined based on tower height. Because the towers are at different heights, the CO_2 signal each one sees is affected in differently from the overall synoptic pattern (3-6 day turnover) vs. vegetation (diurnal cycle). In order to determine the time constant for exponential decay, we applied a first order auto-regressive model (Box et al., 1994) to the longest continuous timeseries of CO_2 concentrations at each observation height on WLEF (Table 4.3), the only tall tower with enough different vertical CO_2 measurement levels to construct a profile. Autocorrelation in the lowest heights is dominated by the diurnal cycle ($\tau \approx 12$ hours) but

the upper heights see a synoptic correlation timescale as well. A similar analysis using Argyle 25m and 107 m timeseries produced correlation timescales of 13 hours and 2.1 days respectively.

To include temporal covariances in $\mathbf{S}_{\text{transp}}$, \mathbf{S}_{aggr} and $\mathbf{S}_{\text{boundary}}$, we used a simple exponential decay function with time constant τ ,

$$S_{ij} = \exp\left(\frac{-\Delta t_{ij}}{\tau}\right) \times \sigma_{ii} \quad (4.21)$$

In equation 4.21, Δt_{ij} refers to the separation in time between two elements of the matrix. For all points, $\mathbf{S}_{\text{boundary}}$ was assumed to have a time constant of 30 days, which encapsulates seasonally changing hemispheric background conditions. In accordance with the decorrelation scales determined above, we employed a time constant of 12 hours for $\mathbf{S}_{\text{transp}}$ and \mathbf{S}_{aggr} at towers other than Argyle. For Argyle, we used a 48 hour time constant.

Table 4.3 – CO₂ correlation timescales from a first-order autoregressive model fit to different heights at the WLE tall tower using data from summer 2004. The first column is based on hourly average concentration data, the second on afternoon average (16-19 GMT, 1 point per day) concentration data. Afternoon averages are used to eliminate effects of the diurnal cycle to determine if a synoptic correlation timescale exists at a given height

Height	CO ₂ correlation timescale from hourly data	CO ₂ correlation timescale from afternoon average data (days)
11 m	0.54	0.399
30 m	0.53	1.20
76 m	0.53	2.15
122 m	0.70	2.41
244 m	1.20	2.57
396 m	1.43	2.94

The airborne data uses a correlation function for $\mathbf{S}_{\text{transp}}$, \mathbf{S}_{aggr} and $\mathbf{S}_{\text{boundary}}$ which includes a horizontal spatial component with decorrelation lengthscale $\ell_{\text{horizontal}}$, a vertical spatial component with decorrelation lengthscale ℓ_{vertical} , and temporal component with decorrelation timescale τ ,

$$\mathbf{S}_{ij} = \exp\left(\frac{-\Delta t_{ij}}{\tau} + \frac{-\Delta x_{ij}^{\text{horizontal}}}{\ell_{\text{horizontal}}} + \frac{-\Delta x_{ij}^{\text{vertical}}}{\ell_{\text{vertical}}}\right) \times \sigma_{ii} \quad (4.22)$$

In Equation 4.22 $\Delta x_{ij}^{\text{horizontal}}$ is the horizontal distance between points, and $\Delta x_{ij}^{\text{vertical}}$ is the vertical separation. For the temporal component, we assumed a time constant of 5 days, representing typical synoptic turnover times for the atmosphere and consistent with the decay times observed at the top level at WLEF. To determine the decorrelation lengthscales in the horizontal and vertical, we fit the airborne data to an exponential variogram model (Kitanidis, 1997), in each case. In this model, the spatial variogram γ is the variance of the difference δ between two CO_2 concentration observations separated by a distance h , either vertical or horizontal,

$$\gamma(h) = \sigma^2(\delta) \left(1 - \exp\left(-\frac{h}{\ell}\right)\right) \quad (4.23)$$

where ℓ refers to the correlation lengthscale. Results of the fitting procedure indicate the horizontal correlation scale is 170 km and the vertical correlation scale is 250 m in the boundary layer.

Because we utilize multiple surface sites, there is spatial correlation between surface sites, in addition to the temporal correlation within the observations from a single site. This is especially true for Howland Forest and Argyle concentrations because the two towers are only 19 km apart. In cases where we included data from multiple towers,

we modified Equation 4.21 to apply covariances *between* surface sites with the same 170 km horizontal correlation scale determined from the airborne data,

$$S_{ij} = \exp\left(\frac{-\Delta t_{ij}}{\tau} + \frac{-\Delta x_{pq}^{\text{horizontal}}}{\ell_{\text{horizontal}}}\right) \times \sigma_{ii} \quad (4.24)$$

In Equation 4.24, p and q index the tower sites. We neglected the correlation between airborne data and surface data because of the wide vertical separation between most of the airborne points and the surface sites.

4.4 A priori model comparisons

4.4.1 Effects of meteorological driver fields

The choice of meteorological driver fields for STILT is very important. The dynamics of the meteorological drivers impact the geographic distribution of the footprint function, the timing of vegetation influence, convective redistribution, and height of the planetary boundary layer. Errors in how the driver fields represent any one of these can have a large impact on modeled CO₂ mixing ratios. Lin et al. (2003) also shows that mass violation within the driving meteorology caused by nudging, coordinate transformations, or interpolation can lead to significant errors in the driving meteorology.

Employing STILT within the receptor oriented modeling framework of Gerbig et al. (2003b) to simulate CO mixing ratios at Argyle illustrates how meteorological drivers can affect modeled concentrations. The surface flux function for CO is simply the fossil fuel contribution and a climatological background similar to the one discussed in Section 4.3.3 is used. Figure 4.3 shows a sample set of results from September, 2004. Although major influxes of air from populated regions are captured quantitatively in many cases, there are some times when the model misses the timing or magnitude of pollution events.

In the longest period of with clean background air at Argyle, it is evident the boundary condition is not accurate. The other periods of model-data mismatch are likely related to dynamical errors. For instance, on September 12th urban pollution was trapped by a sea-breeze-type circulation and advected up the coast, but this circulation was not dynamically represented within EDAS-40 driver fields, as shown by the time- and area-integrated STILT footprint in Figure 4.4

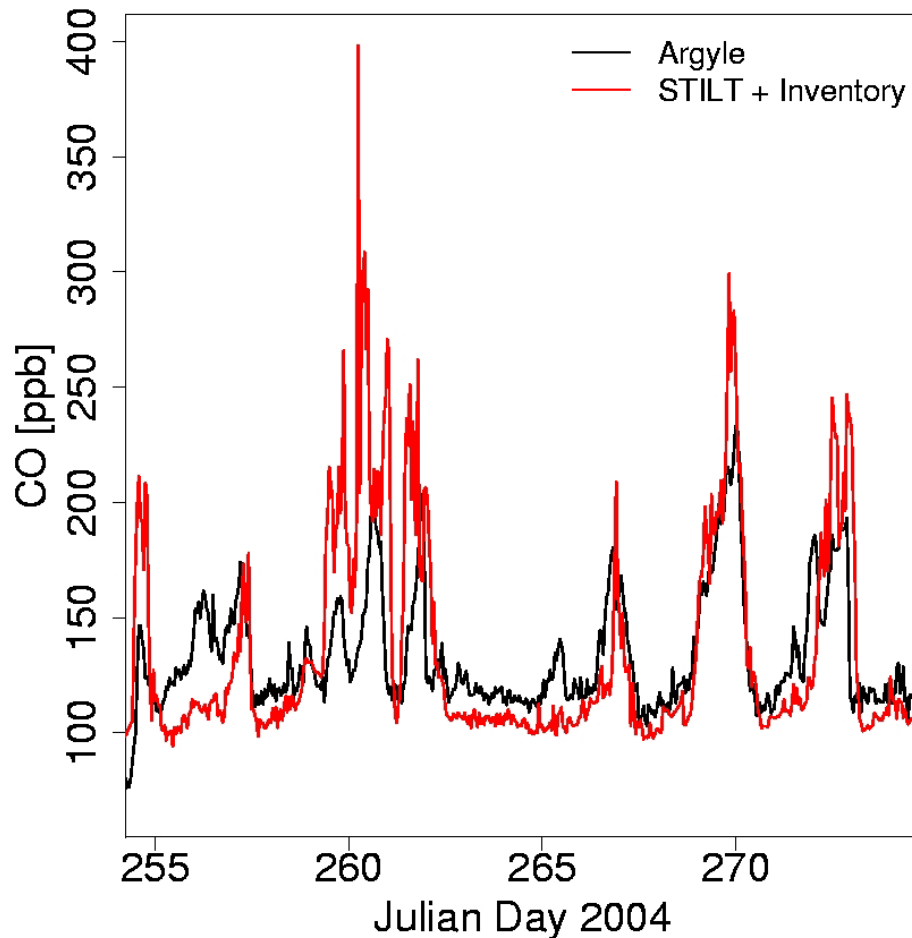


Figure 4.3– CO simulation for Argyle tower (black) and observations (red) using STILT with a fossil fuel inventory and climatological background. Points in time where the model does not observations are mostly are due to the transport parameterization used to drive STILT (Plot courtesy Scot Miller, Harvard University).

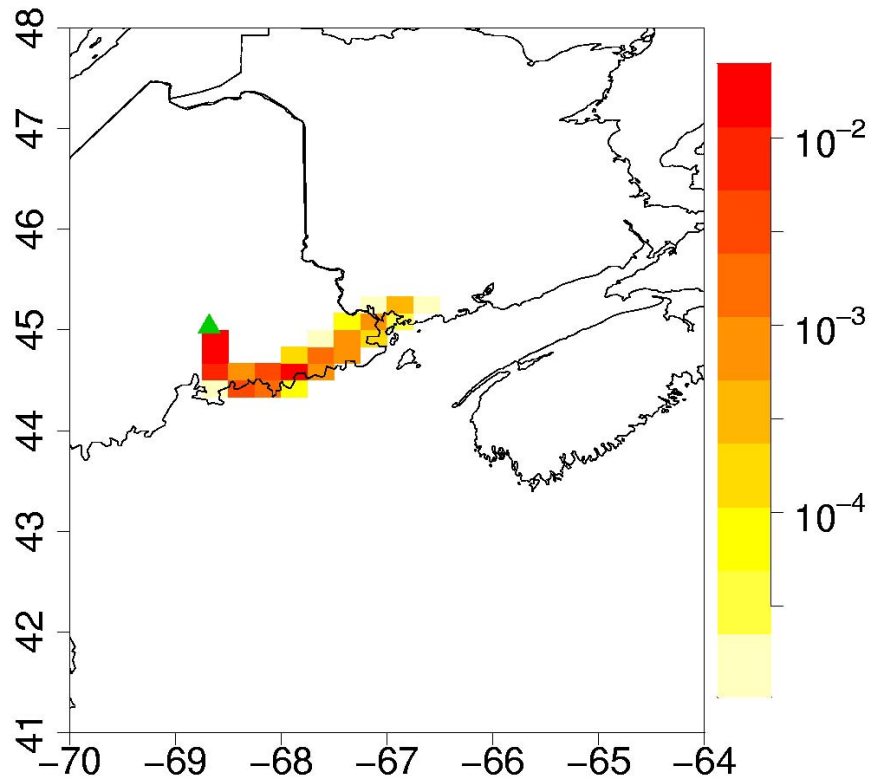


Figure 4.4 – Time and area integrated STILT footprint ($\text{ppm}/\mu\text{mol}/\text{m}^2/\text{s}$) for Argyle tower on the evening of September 12th, 2004. The footprint f is calculated as in Equation 4.5 and the plot shows $\int dt \int dx dy f$, for 16 hours upstream of the receptor point. Note the log color scale.

For this analysis, we relied on the meteorological driver fields from EDAS-40, which are archived regularly (Rolph, 1997) and readily available from 2004 onwards. STILT runs using EDAS-40 exhibit minimal mass violation, correctable as outlined in Lin et al. (2003), but cannot simulate convection because convective mass fluxes are not archived. BRAMS represents the next-generation meteorological driver for STILT, characterized by the ability to explicitly model convection, almost negligible mass violation effects and capability to nest multiple spatial resolutions.

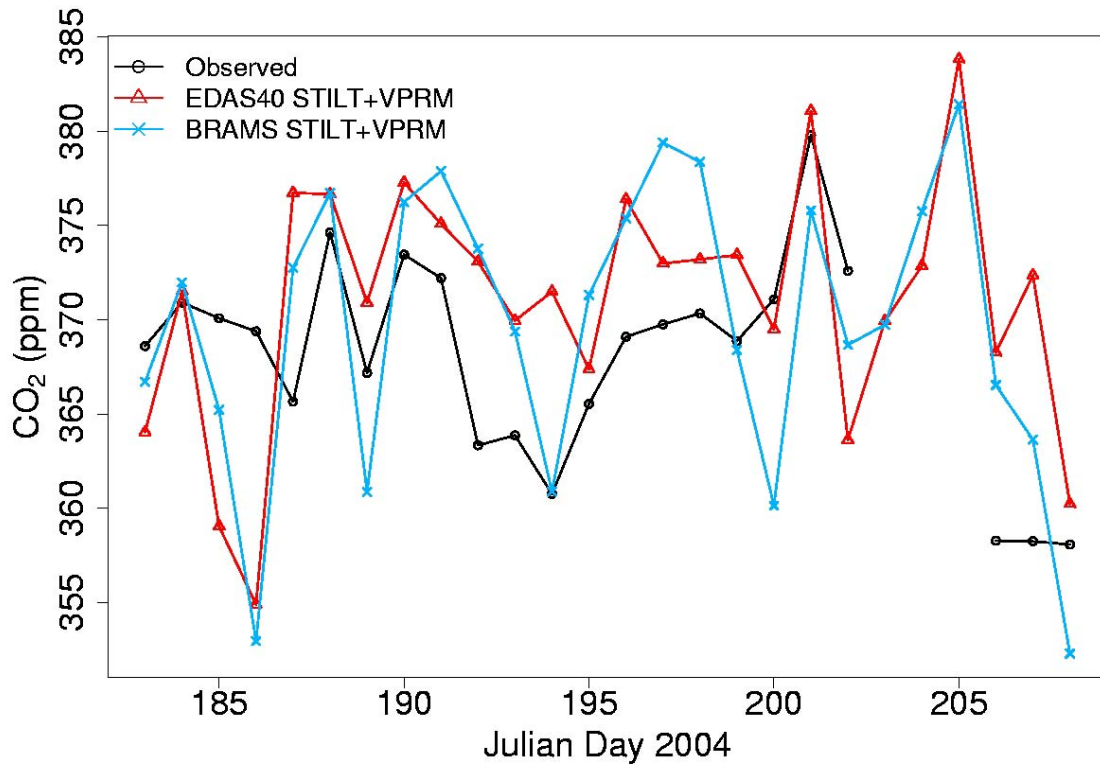


Figure 4.5 – Timeseries of afternoon average concentrations at Argyle tower from observations and STILT+VPRM with two different meteorological drivers. The Gerbig boundary condition is used.

Table 4.4 – BRAMS and EDAS-40 afternoon average comparison

	N	Mean Residual (model – obs) [ppm]	R ²	RMSE
EDAS-40 vs. Observations	23	2.5	0.10	7.4
BRAMS vs. Observations	23	1.0	0.25	6.9
BRAMS vs. EDAS-40	26	-1.3	0.58	5.2

Figure 4.5 and Table 4.4 show comparison of observed and a priori STILT+VPRM afternoon average concentrations for 4 weeks in July 2004 at Argyle tower using EDAS-40 and BRAMS meteorological drivers. Compared with STILT+VPRM driven by EDAS-40, STILT+VPRM driven by BRAMS marginally improves correlation and reduces the root mean square error to the observations, but the differences are difficult to discern from the timeseries. Results driven by BRAMS and

EDAS-40 are far more correlated with each other than either one is correlated with the observations. We attribute this strong correlation to the global meteorological drivers used to set the boundary values at the edge of the each models domain; both BRAMS and EDAS-40 were initialized from the National Center for Environmental Prediction Global Data Assimilation System (NCEP GDAS) global reanalysis product. The comparison demonstrates the importance of the global driver used to initialize the mesoscale models that drive STILT; errors in the large-scale boundary fields can propagate into STILT footprint calculations regardless of the mesoscale model chosen. Further, it confirms that EDAS-40 is a reasonable meteorological driver for this study.

4.4.2 Application of the revised boundary condition

In order to take full advantage of the two potential CO₂ tracer boundary conditions we have available to evaluate a priori STILT+VPRM calculations, both tower and layer airborne data are needed. Airborne data provide a set of spatial snapshots to complement the temporally continuous information from the tower. Figure 4.6 and Table 4.5 show a comparison of a priori STILT+VPRM mixing ratios at Argyle to observations using both the Gerbig boundary condition and the revised boundary condition. In calculating the statistics, July 1st, 2nd, and 4th (days 183, 184, 186) were excluded because they each had a residual more than 3 standard deviations from the mean for both boundary condition cases, indicating some factor other than the boundary condition was responsible for the large deviation of model results from the observations. Overall, the revised boundary condition provides better performance, with a nearly 20% reduction in RMSE between model results and observations for afternoon averages across the two

months. However, most of the difference is attributable to the positive bias in the Gerbig boundary condition in July. In August, both the Gerbig boundary condition and the revised boundary condition perform quite similarly.

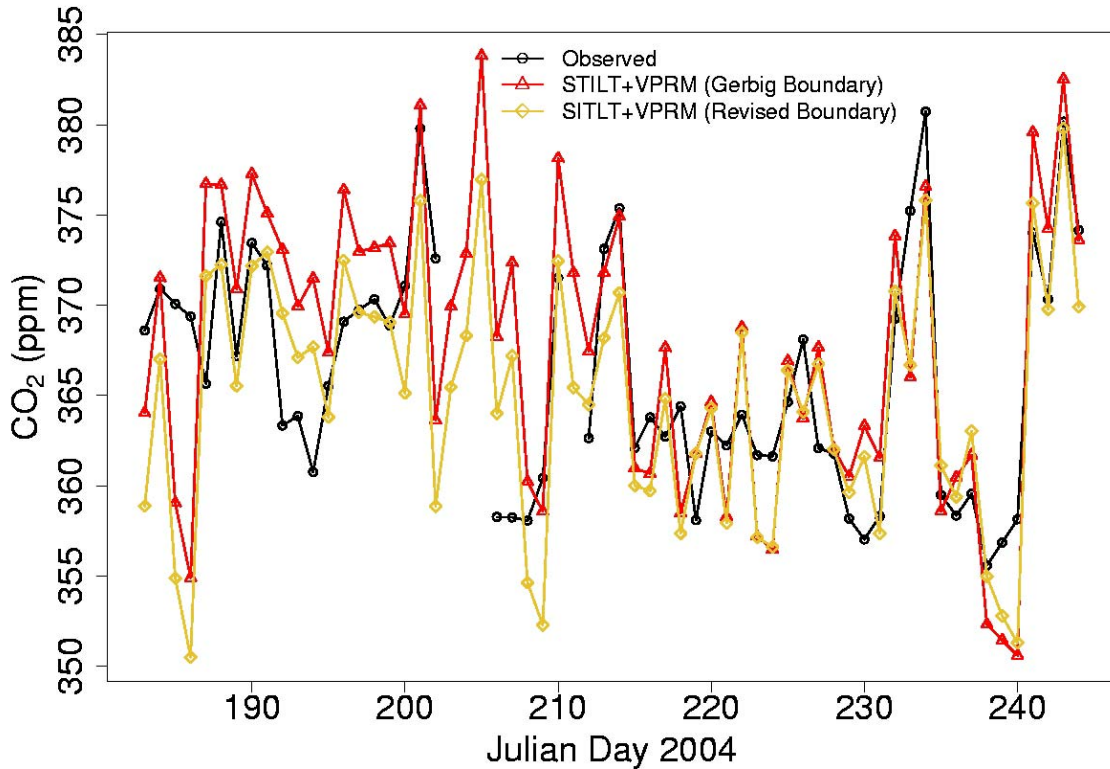


Figure 4.6 – Timeseries of STILT+VPRM afternoon mean CO₂ concentrations at Argyle with observations for July 1st to August 31st, 2004 using two different tracer boundary conditions. EDAS-40 is used to drive transport.

Table 4.5 – Statistical comparison of afternoon average CO₂ concentration observations at Argyle using Gerbig and Revised boundary conditions (July 1st, 3rd, and 4th excluded)

	N	Mean Residual (model –obs) [ppm]	R ²	RMSE [ppm]
Gerbig Boundary (July and August)	54	1.7	0.59	5.3
Revised Boundary (July and August)	54	-0.69	0.61	4.5
Gerbig Boundary (July)	23	4.1	0.37	6.5
Revised Boundary (July)	23	-0.18	0.35	5.2
Gerbig Boundary (August)	31	-0.13	0.71	4.3
Revised Boundary (August)	31	-1.1	0.72	3.9

It is difficult to discern the reason Argyle model results in July have a positive bias with the Gerbig boundary condition, but one possibility is that northerly transport was more frequent during July and better characterized by the incorporation of northern observations in the revised boundary condition. Alternatively, the Pacific station data used to propagate the Gerbig boundary condition in time may have experienced a period of anomalously high CO₂ concentrations, due to for instance due to an Asian pollution plume, during July 2004 not representative of the Pacific atmosphere as a whole. Because the revised boundary condition averages over a longer period and uses climatological propagation in time it is both buffered from such short term anomalies if they are problematic and unable to incorporate them if they are important.

4.4.3 Airborne cross-section case study

The Argyle results suggest the Gerbig boundary condition is biased too high in July while the revised boundary condition is more accurate for that time period, creating a new constraint on model comparisons with airborne data. Differences in model fidelity in space can indicate situations where transport or surface sources are poorly represented. Figure 4.7 shows a latitude-altitude cross section of CO₂ observations for a flight in the mid to late afternoon of July 17th, 2004, which traveled south-southwest from rural central Quebec to Bangor, Maine. The grey line shows the flight track, with grey points showing a subset of 255 points evenly spaced in time to be used as receptor points for STILT+VPRM calculations. Periods along the flight track without observations are from periods where the CO₂ instrument was doing its usual in-flight calibrations. The cross-section shows the signature of moderate vegetative CO₂ uptake in the between latitudes

48 and 49, with a gradient through the boundary layer, but minimal uptake in the far north and very little uptake on the profile of final descent at the south end (left side) of the flight.

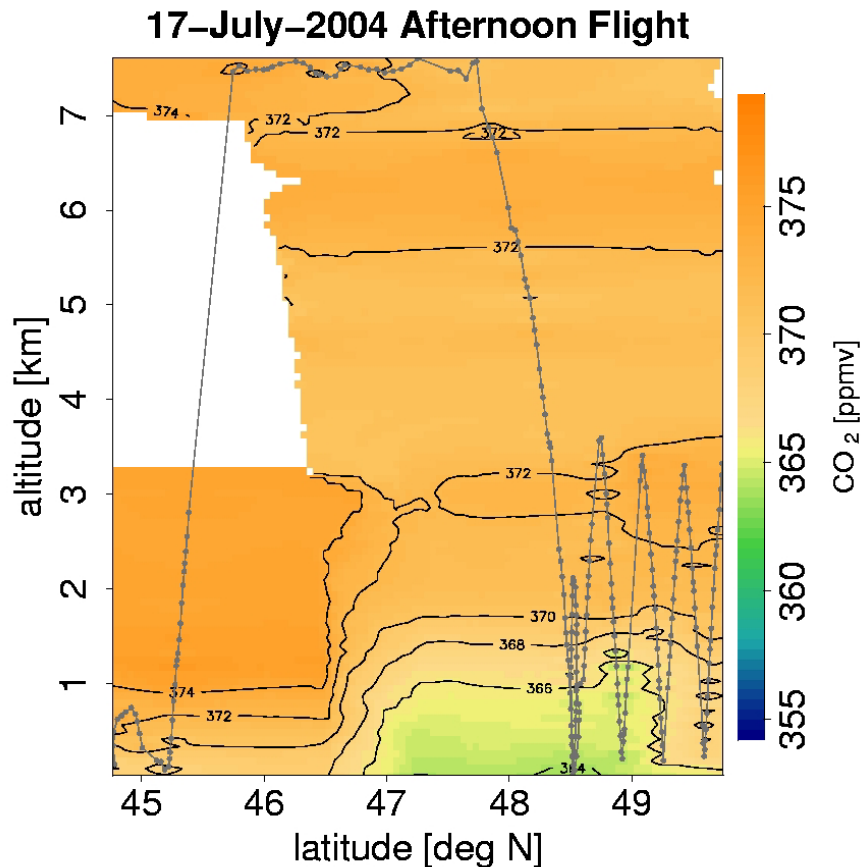


Figure 4.7– Latitude altitude CO₂ cross-section from the COBRA-Maine flight of July 17th, 2004, which traveled north to south (right to left) from central Quebec to Bangor, ME. The grey line indicates the flight track, with points showing the locations of evenly spaced receptor points, where 20-second averages to be used for model comparison were calculated. Periods without points correspond to periods of instrument calibration. An inverse distance weighted interpolation was used to create the contours.

STILT+VPRM modeled mixing ratios corresponding to the observations, along with the residuals, are shown for both the Gerbig boundary condition and revised boundary condition in Figure 4.8. Note the difference in STILT+VPRM concentrations using different boundary conditions, but keeping all other aspects identical, is about 6 ppm for the bulk of the cross-section.

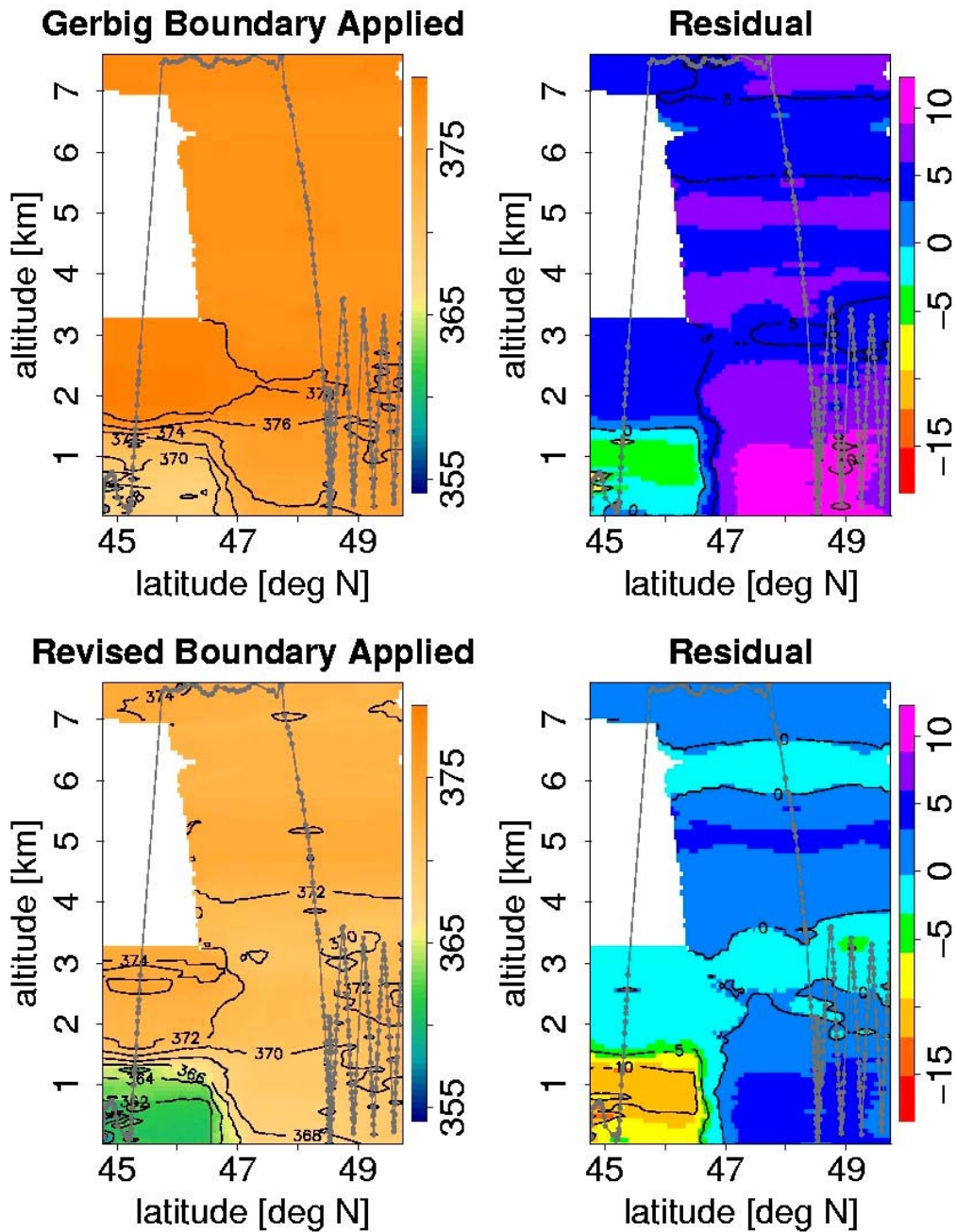


Figure 4.8 – STILT+VPRM latitude altitude CO_2 cross-sections corresponding to the observations in Figure 4.7, along with the residuals, using both potential boundary conditions. The symbols and colorscheme for the left panels are the same as in Figure 4.7.

However, there are spatial differences in the ability of the model to reproduce the observations—the Gerbig boundary is much closer to the observations in the single southern descending profile while the revised boundary is much closer to the observations in the north. We suggest using the revised boundary condition is a better indicator of STILT+VPRM performance in this cross-section because the Gerbig boundary condition has a known general positive bias in July as indicated by results at Argyle; the agreement for multiple profiles in the north is excellent, but there is only one profile in the south; and the flow during this flight was from the north northwest across Hudson Bay, meaning a northern boundary is applicable.

Using the revised boundary condition indicates that the model is either getting the transport, including dynamics of the boundary layer, incorrect or the surface flux model is too vigorously taking up CO₂ or a combination of both. There is qualitative evidence to suggest it is a combination, with an ambiguous level of contribution from each. The meteorological situation over central Maine was untidy, with weak surface high pressure a few hundred kilometers to the northeast, weak surface low pressure a few hundred kilometers to the west, northwest flow, and shallow afternoon convection. It is a challenge for the transport model to effectively represent the atmosphere in such a situation. Furthermore, the southern profile was the final flight descent of the day, occurring around 22 GMT (1800 EDT), about the onset time of the evening breakdown of the mixed layer and a difficult period for transport models.

Surface uptake of CO₂ appears to be too vigorous, but is very likely to be the result of a driver problem rather than a problem with the VPRM parameters themselves. CO₂ uptake in the VPRM is linearly dependent on incoming shortwave radiation (Equation 4.6),

therefore any error in the parameterization of incoming shortwave radiation input will translate directly into errors in GEE. July 17th was clear but hazy over central Quebec and partially cloudy, hazy, with multiple cloud layers over Maine. The variable cloudiness can be seen in the timeseries of observations of photosynthetic photon flux density (PPFD) at Howland Forest, shown in Figure 4.9. In addition to Howland PPFD, a satellite-based shortwave radiation product from the University of Wisconsin calculated from GOES observations (Diak et al., 2004) is shown, along with the NLDAS downward shortwave radiation input used in STILT+VPRM for the grid box containing both Howland and Argyle towers, and the EDAS-40 radiation field for the same location.

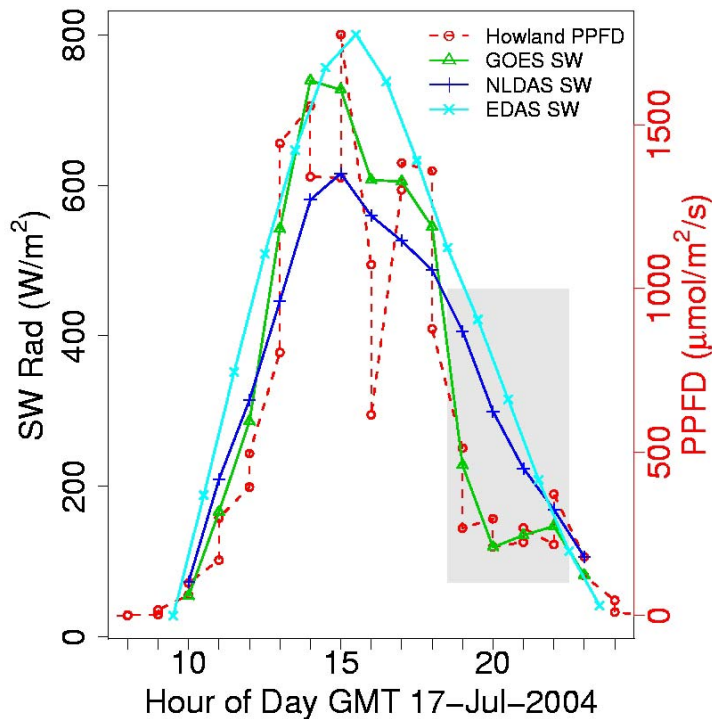


Figure 4.9 – July 17th, 2004 hourly values of photosynthetic photon flux density (PPFD) observed at Howland forest and the GOES-derived hourly shortwave radiation product for the grid box containing Howland and Argyle towers, the EDAS-40 Shortwave Radiation field for the grid box containing Howland tower, and the NLDAS shortwave radiation value used as input for STILT+VPRM, for the grid box containing Howland tower. The gray box is the time of the afternoon COBRA-Maine on this day which observed the profile shown in Figure 4.7.

The sharp downward spikes seen in Howland PPFD but not in the GOES shortwave radiation are indicative of clouds passing the tower which are smaller than the $1/5^\circ$ latitude \times $1/5^\circ$ longitude grid box of the GOES product. The NLDAS product, which has a resolution of $1/8^\circ$ latitude \times $1/8^\circ$ longitude, smoothes the radiation variations over the course of this partly cloudy day, resulting in a product that matches the observations on a daily average—the area under the GOES curve and the NLDAS curve is about the same—but doesn't match the satellite observations at any point after 1200 GMT (0800 EDT). The NLDAS radiation is too low in the late morning and early afternoon, and too high in the late afternoon. The time of the afternoon flight is shown by the gray box, neatly matching the period of time when the NLDAS overestimates the observed radiation. The NLDAS radiation product smoothes in space, as well as time, as is evident from Figure 4.10.

It is tempting to seek to utilize only the GOES radiation observations to drive the VPRM, but the radiation retrieval algorithm fails during periods with a low sun angle. The NLDAS represents the best available compromise, combining a GOES-radiation product similar to one shown in Figures 4.9 and 4.10 with the EDAS-40 radiation fields. The overestimate in Figure 4.9 is typical of EDAS-40 radiation fields, which have a consistently high bias, especially in partly cloudy conditions. This consistent bias is a major disadvantage to using EDAS-40 radiation fields to drive VPRM fluxes. Although NLDAS is the best available radiation product to drive the VPRM, partly cloudy days are still sometimes poorly represented.

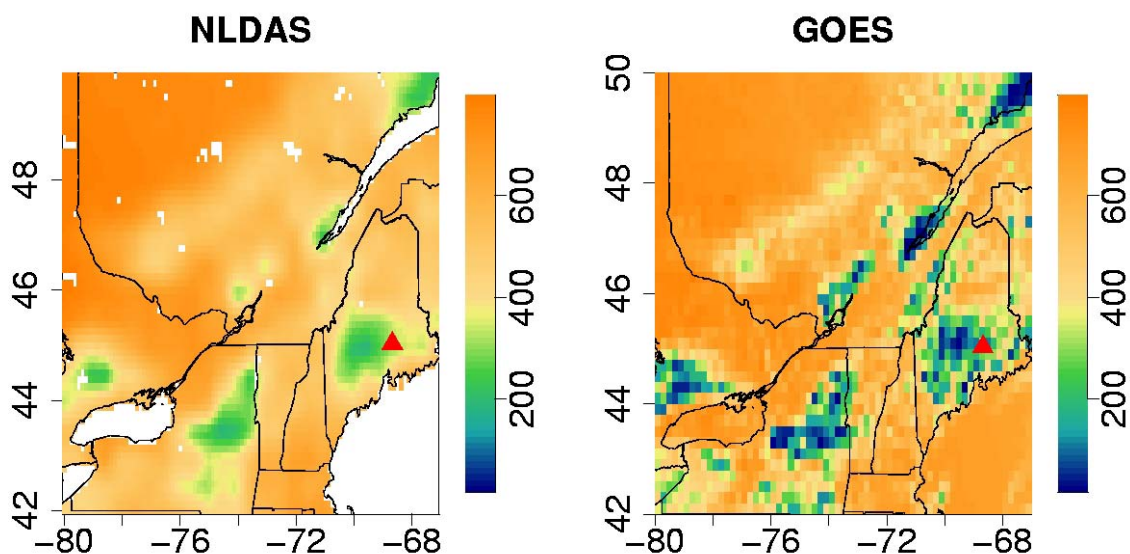


Figure 4.10 – Comparison of shortwave radiation over New England and southern Quebec for 2000 GMT (1600 EDT) on July 17th, 2004 from the NLDAS and University of Wisconsin GOES-radiation products. The location of Argyle tower is shown with a red triangle.

A final constraint from for this case study comes from the Argyle afternoon a priori STILT+VPRM average value for July 17th, calculated using the revised boundary condition (Figure 4.6, yellow line, day 199). The STILT+VPRM mixing ratio matches the observation closely for that day. Since the afternoon average (1700-2000 GMT) balances the apparent positive and negative errors in NLDAS radiation (Figure 4.9), it appears that the EDAS-40 overall dynamics are reasonable. Interestingly, the residual southernmost aircraft profile from that day is lowest in the surface layer (Figure 4.8, bottom right panel, 45.2° latitude, directly over Howland tower). This line of reasoning suggests that in addition to driver problems in the VPRM, the breakdown of the mixed layer in early evening might be poorly represented in the transport calculations.

Differences between observations and modeled results caused by incorrect driver data in the VPRM and by inadequately represented boundary layer dynamics in the

transport fields driving STILT are both present in addition to effects of using non-optimal parameters in the source function. A model with perfectly represented parameters in the source function will still not match the observations if there are errors in the driver data or transport dynamics are present. As a corollary, if the model errors caused by such effects are greater than the errors caused by misadjusted parameters, an optimization of those parameters will not necessarily enhance the agreement of the model to the observations.

4.4.4 Regionally specific representation error in the source function

Errors in the source function associated with misrepresentation of the type of vegetation can have dramatic effects on STILT+VPRM calculated mixing ratios. Figure 4.11 shows an example where a single vegetation class is poorly represented. WLEF tower is located in northern Wisconsin, near the northern edge of an area spanning most of southwestern Wisconsin which the VPRM classifies as grasslands, as shown in Figure 4.12. Much of this area is pasture used for dairy farming, but the VPRM grassland parameters are calibrated at the Vaira Grassland AmeriFlux site (Baldocchi et al., 2004), a semi-arid oak/grass savanna ecosystem located in California which bears little physical or ecological similarity to southwestern Wisconsin pasture. When environmental drivers typical of southern Wisconsin are applied using parameters calibrated to semi-arid grasslands, the result is large overestimation of CO₂ uptake, visible in Figure 4.11 (red line) as large negative excursions in CO₂ concentration when the WLEF footprint is dominated by the misrepresented grasslands, as in Figure 4.13 for example. The

representation error is not unique to Wisconsin; similar pasture areas, also classified as grasslands, can be found in southeastern Quebec.

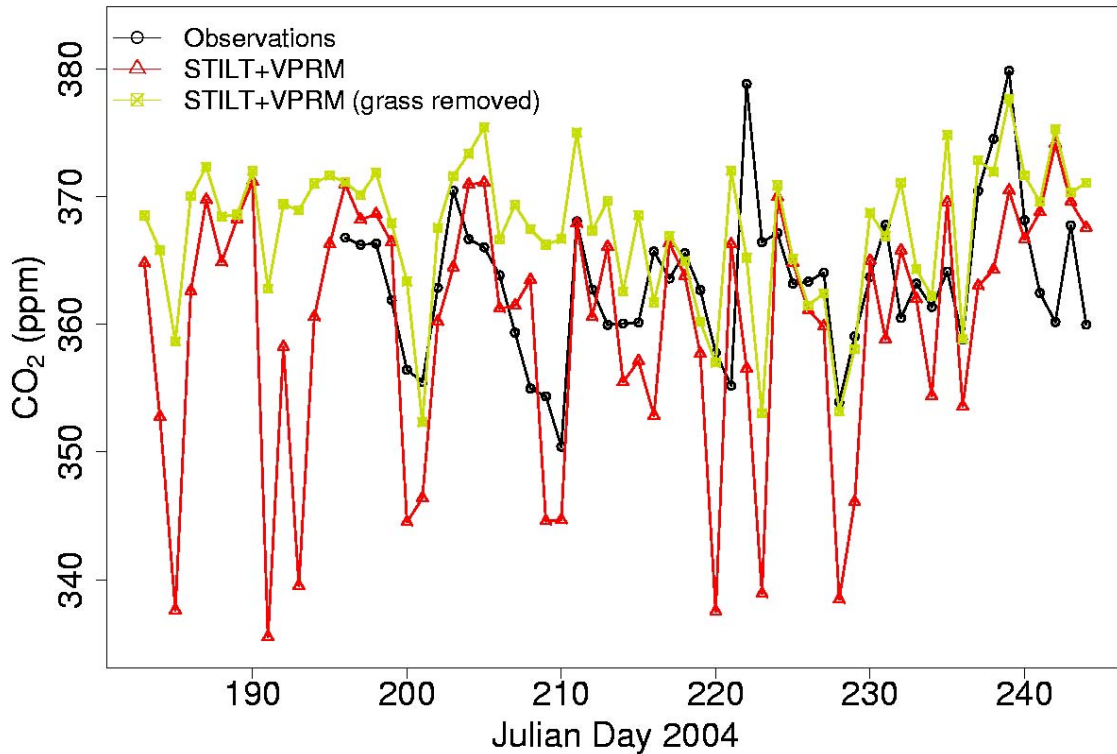


Figure 4.11 – STILT+VPRM timeseries of afternoon averages for July and August, 2004 at WLEF tower in central Wisconsin. The series of large downward excursions (e.g. days 185, 191, 193, 220, 223, 229) in the a priori model (red line) are the result of model overestimation of grass uptake. Forcing grass to be flux neutral ($NEE = 0$; light green line) eliminates the large excursions.

An informative ad-hoc experiment can be conducted by forcing grasslands to be flux neutral ($NEE_{\text{grass}} = 0$) in the STILT+VPRM framework, removing a major contributor to the mean time- and space-integrated influence (mean across all hours is 2.26 ppm/ $\mu\text{mol}/\text{m}^2/\text{s}$ for grasslands and 7.30 ppm/ $\mu\text{mol}/\text{m}^2/\text{s}$ for total vegetation). This has the effect of removing all the large negative CO_2 concentration excursions, reducing root mean square error to the observations from 8.9 ppm to 7.3 ppm, and greatly

increasing the fidelity of the model to observations for certain time periods (e.g. Figure 4.11, days 225 to 240), but also greatly decreasing fidelity of the model during other time periods (e.g. days 207 to 212). These results suggest that if transport is correct and there are no driver VPRM environmental problems which differentially affect vegetation classes, the grasslands of southern Wisconsin might be close to flux neutral for much of time, but are periodically active. In such a situation, a Bayesian parameter optimization as developed here will fail because the needed optimization parameter is time-dependent. The *a posteriori* concentrations will be closer on average to the observations, but periods of time when the *a priori* model closely matches observations will have larger residuals. A Kalman filter may be a more appropriate optimization technique to handle parameters requiring time-dependence.

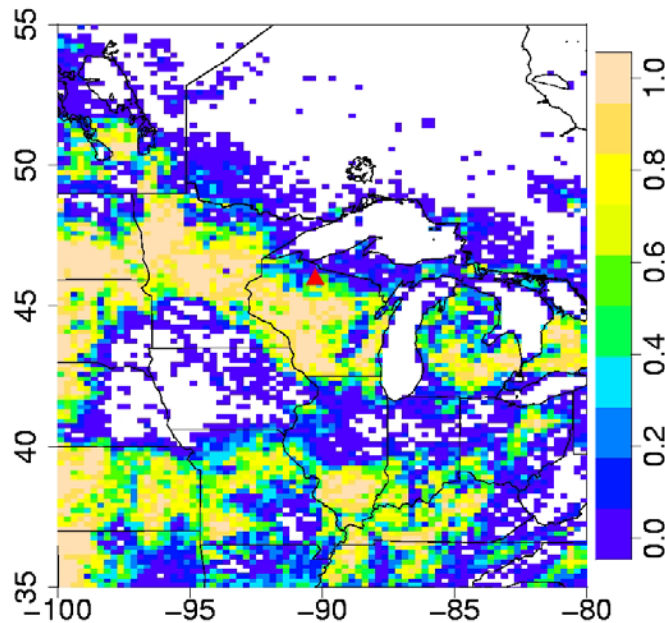


Figure 4.12 – Fractional coverage of grassland in the region of the WLEF tall tower. The tower location is noted with a red triangle. The grassland in southwestern Wisconsin is mostly pasture and is significantly different from the semi-arid grassland in western Kansas, Nebraska, and South Dakota.

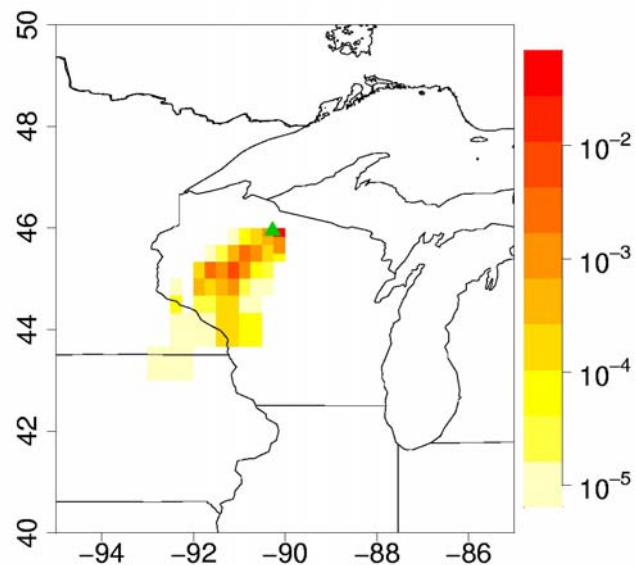


Figure 4.13– 3-day integrated STILT influence footprint from WLEF on August 7th (day 220) 19 GMT, corresponding to a large downward excursion in STILT+VPRM concentration not seen in the observations. The footprint is dominated by grasslands.

Although atmospheric data assimilation can provide a constraint to correct fluxes for grasslands at WLEF, the results would have to be interpreted with caution. First, the *a priori* model for grasslands is a very poor representation of the pasture ecosystem near WLEF, so although a Bayesian optimization could significantly reduce uncertainty in the grassland parameter, the *a posteriori* parameter value will be partially weighted by the erroneous *a priori* model state. Second, the optimized parameter value would be regionally specific to the area in the near-field of WLEF. The change in concentration associated grasslands in the far field (e.g. western Nebraska, Kansas, South Dakota in Figure 4.13) will be incorrectly calculated, creating a different and presumably—but not assuredly—smaller representation error. The best correction would be to add a separate vegetation class for the type of pasture so common in southern Wisconsin, but to our knowledge there is no dairy farm pasture flux dataset available with which to calibrate the VPRM.

4.5 Optimization results

We applied the Bayesian optimization framework individually to each of the available tower timeseries, the subsetted boundary layer airborne data, and various combinations of these datasets. Table 4.6 illustrates the constraint placed on the inversion by including all receptor points. The number of degrees of freedom associated with the signal can be interpreted as an estimate of the number of independent parameters known to better than parameter uncertainty, or put another way the number of independent pieces of information provided about the parameters from a given dataset. The total degrees of freedom will equal the total number of parameters, in the case eleven, so the rest are associated with noise in parameter space. Degrees of freedom from noise should not be confused with measurement noise. A tower with a footprint with extremely homogeneous vegetation, for instance, might likely have a low number of degrees of freedom for the signal because there is mostly information about a single vegetation class available for such a tower. When viewed in this context, it is expected that Argyle would have the highest number of degrees of freedom for the signal because the tall tower would see a larger footprint than the smaller towers. Perhaps more surprising is the amount of constraint provided by observations at Chebogue Point—which despite a much smaller footprint that is dominated by marine conditions, apparently receives a very diverse set of vegetative influences. The relatively low number of degrees of freedom for the signal at Harvard Forest is probably due to its location in the middle of a large, fairly contiguous region of deciduous forest; which likely dominates its footprint.

Table 4.6 – Constraints placed by various network data inputs on the VPRM through Bayesian inversion

Data Input	N	df _{signal}	df _{noise}	% change in cost function (J)	% reduction in RMSE to observations
Argyle	401	6.9	4.1	-19	-4
Howland	268	6.0	5.0	-12	-0
Harvard	257	5.2	5.8	-9	-4
Chebogue Point	371	6.8	4.2	-19	-9
Thompson Farm	397	5.5	5.5	-13	-14
Argyle + Harvard	658	7.3	3.7	-16	-4
All Surface	1694	8.5	2.5	-12	-2
Bulk Airborne	657	6.4	4.6	-24	-3
Argyle + Airborne	1058	8.1	2.9	-19	-4
All Surface + Airborne	2351	9.0	2.0	-13	-1

The trends in degrees of freedom between various combinations of inputs are informative. First, the marginal amount of data needed to add degrees of freedom to the signal is extremely high. One tower provides a certain amount of information to the inversion; but a second observation tower within the region adds a much smaller amount of information. This is in part because much of the information is redundant—the decorrelation lengthscale is important. However, even for towers separated by distances significantly greater than the decorrelation lengthscale (e.g. Argyle and Harvard are separated by ~3 times the decorrelation distance) the trend applies, with an increase in degrees of freedom for the signal of 0.4 over the Argyle solo case. Even using the entire surface network to increase the number of observations available to the inversion by an order of magnitude only increases the number of degrees of freedom by about 3, or about 50% more than the number of degrees of freedom provided by a single tower.

The ensemble airborne data by itself provides a constraint similar to that of a single tower, but the airborne data provides a much higher *marginal* constraint when combined with a single tower. The number of degrees of freedom provided by Argyle +

airborne data is about the same as for the entire surface network, a result that reiterates the fact that in the context of regional inversion, the continuous temporal coverage provided by a tower is greatly complemented by the spatial coverage provided by aircraft and vice versa. This intuitive notion has been recognized for a long time and built into the design of the COBRA airborne campaigns (Lin et al., 2006), but has not been quantitatively demonstrated until this study.

A striking feature of Table 4.6 is the disjunction between the reduction of the standard least squares cost function and change in root mean square error between the model and the observations. Despite moderately significant reductions in the cost function, there is only marginal improvement in the model fidelity to the observations. Steadily increasing the amount of data input to the inversion neither decreases the relative cost function nor the RMSE despite increasing parameter constraint. Evidently model errors are not associated with surface flux source function being optimized, but instead with other aspects of the modeling framework, such as those discussed in Section 4.3.

Figure 4.14 shows the *a priori* and *a posteriori* values parameter values for the inversion case with the maximum amount of data, using all the surface and airborne data together. As seen in Table 4.6, this case provides degrees of freedom from the signal of 9.0, suggesting that this data can constrain about 9 vegetation classes. Inspection of Figure 4.14 shows that dry temperate evergreen forests are very weakly constrained in the inversion, while savannas and peatlands are partially constrained, and the other vegetation classes are well constrained by the inversion. Within Maine and southern Quebec, there are virtually no areas of dry temperate evergreen forests, very few savannas, and peatlands primarily exist in the far field to the north of the study area, so

the case utilizing all surface and airborne data is likely approaching the limit on the total number of parameters that data from this region can constrain.

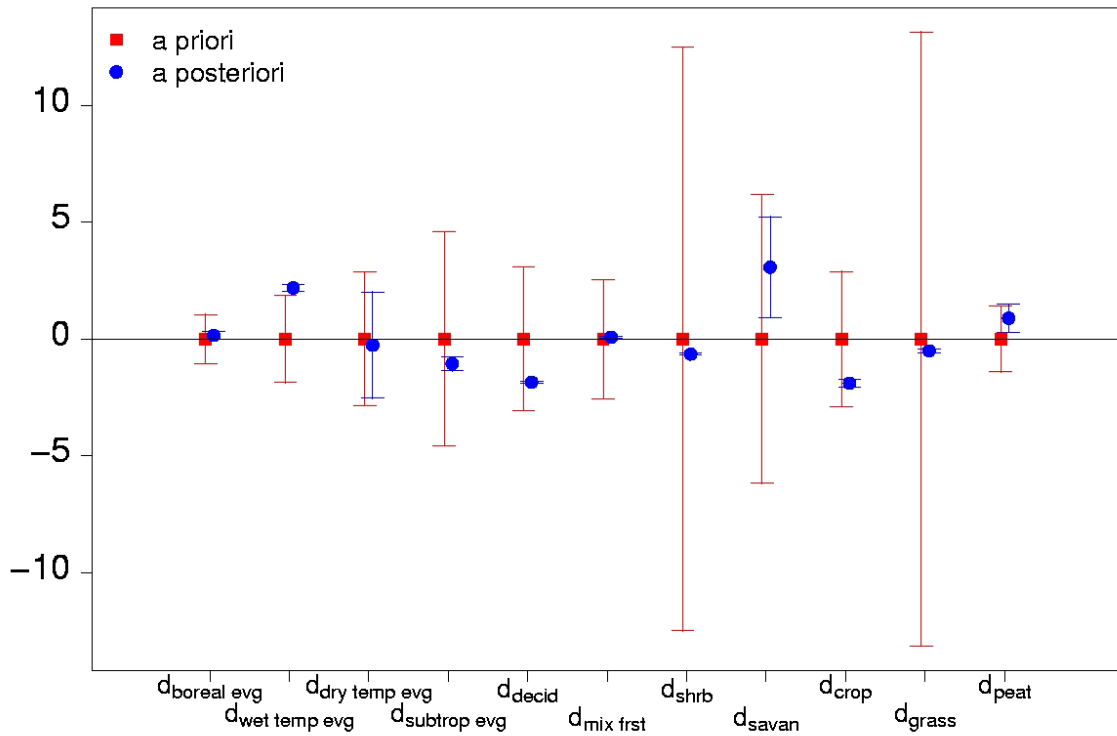


Figure 4.14 – A priori and a posteriori parameter values and uncertainties for the eleven vegetation classes from the Bayesian inversion case using all airborne and daytime surface data together. These results are based on the revised boundary condition, but using the Gerbig boundary condition gives comparable results.

Table 4.7 shows the *a posteriori* parameters and associated uncertainties are generally insensitive to the selection of the tracer boundary condition, an important result which is further indication that the major source of error lies with atmospheric dynamics.

Table 4.7 – Optimization parameter values and their associated uncertainty using all data

Vegetation Class	<i>a priori</i> d_k ($\mu\text{mol}/\text{m}^2/\text{s}$)	<i>a posteriori</i> d_k [Gerbig boundary] ($\mu\text{mol}/\text{m}^2/\text{s}$)	<i>a posteriori</i> d_k [revised boundary] ($\mu\text{mol}/\text{m}^2/\text{s}$)	<i>a priori</i> uncertainty	<i>a posteriori</i> uncertainty [Gerbig boundary]	<i>a posteriori</i> uncertainty [revised boundary]
Boreal evergreen	0	0.21	0.11	1.1	0.18	0.18
Wet temp. evergreen	0	2.1	2.2	1.9	0.14	0.14
Dry temp. evergreen	0	-0.50	-0.26	2.9	2.3	2.3
Sub-trop. evergreen	0	-1.6	-1.0	4.6	0.30	0.30
Deciduous forest	0	-2.0	-1.9	3.1	0.026	0.026
Mixed forest	0	0.28	0.10	2.5	0.027	0.027
Shrub	0	-0.53	-0.64	12.5	0.036	0.036
Savanna	0	1.2	3.0	6.2	2.2	2.2
Croplands	0	-2.1	-1.9	2.9	0.18	0.18
Grasslands	0	-0.44	-0.54	13.2	0.072	0.072
Peatlands	0	0.79	0.84	1.4	0.59	0.59

Timeseries of afternoon average CO_2 concentration observations, *a priori* and *a posteriori* STILT+VPRM of afternoon average concentration values are shown in Figure 4.15, with comparison statistics in Table 4.8. The *a priori* model captures variation in CO_2 concentration most effectively at Argyle with the lowest RMSE of prediction and highest correlation value, which is expected because Argyle is a tall (107 m) tower, presumably less affected by surface gradients from local vegetation and with a more regionally integrated signal. The *a priori* model performs worst at Chebogue Point, located on the coast of Nova Scotia where the ability of the model to calculate accurate atmospheric CO_2 concentrations is entirely dependent on how well it simulates the marine boundary layer. Dynamics of the marine boundary layer usually are poorly

represented in the model, as evidenced by complete lack of correlation between the *a priori* model and the observations at Chebogue Point. The difference in model performance between Argyle and Howland, towers of differing heights separated by 19 km, indicate that the model may have trouble simulating the terrestrial boundary layer as well. There is a stronger negative bias in the afternoon average observations at the shorter towers, suggesting the model is not mixed enough and maintains a too strong a gradient in the surface layer. The airborne data discussed below suggest this is a general result, but there is no way to confirm at the other towers because each only has a single level.

For the most part, large excursions in model results remain after optimization, suggesting that they are not caused by errors in the source function or that the data provides very little information to constrain the causes. There is little improvement at Argyle, where the difference between *a priori* and *a posteriori* results in model-data comparison statistics is minimal. The most improvement is seen at Chebogue, where the *a priori* model did the worst, and at Thompson Farm, where the optimization greatly reduces an apparent bias in the model results. Overall, the optimization does not provide robust improvement in the ability to capture the variations in CO₂ at surface locations. We interpret this result as an indication that the errors in the model are dominated not by source flux source function, but instead by a combination of errors in the driver values, tracer boundary conditions, or transport fields, either global boundary fields or the EDAS-40 fields which drive the STILT particles.

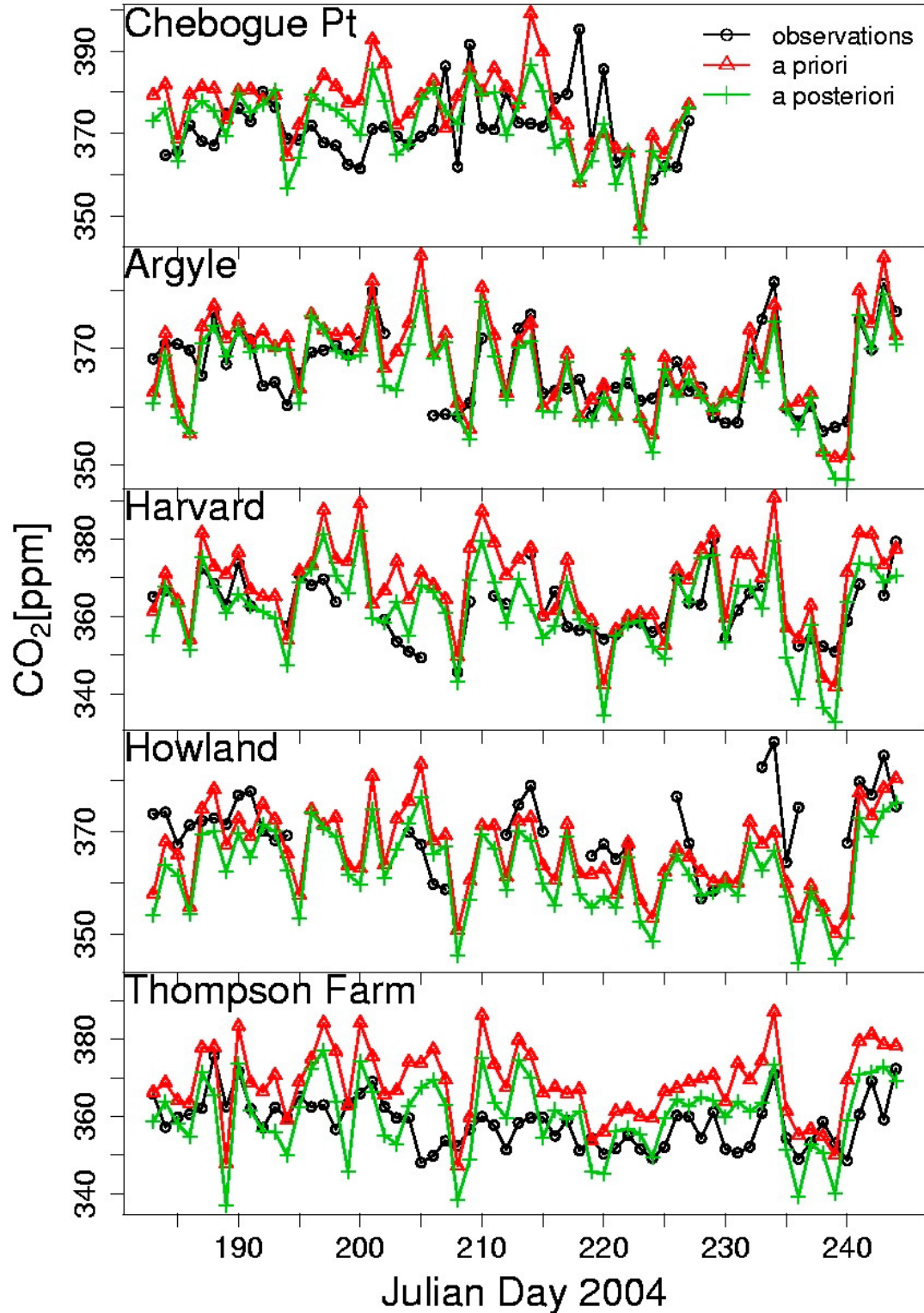


Figure 4.15 – Time series of afternoon average (1700-2000 GMT; one point per day) a priori and a posteriori STILT+VPRM concentration values at each of the surface sites, along with corresponding observations. Results utilizing the Gerbig boundary condition are shown.

Table 4.8 – Comparison statistics for afternoon average inversion results at individual surface stations. Results applying both the Gerbig boundary condition and the revised boundary condition are shown. The revised boundary condition results are shown in blue. Filtering removes points associated with very stable conditions ($u^* < 0.20$ m/s) and from the time period associated with Hurricane Alex.

	Argyle	Howland	Harvard	Chebogue Point	Thompson Farm
N (Filtered afternoon hours; 1700 to 2000 GMT)	174	95	116	149	165
mean residual <i>a priori</i> [ppm] (Gerbig Boundary)	1.3	-2.3	5.2	6.4	9.2
mean residual <i>a priori</i> [ppm] (Revised Boundary)	-1.3	-5.4	2.1	2.3	6.2
mean residual <i>a posteriori</i> [ppm] (Gerbig Boundary)	-0.75	-6.1	-0.53	2.8	1.1
mean residual <i>a posteriori</i> [ppm] (Revised Boundary)	-3.3	-8.0	-2.4	-1.2	-0.34
RMSE <i>a priori</i> [ppm] (Gerbig Boundary)	7.4	10.0	9.0	10.0	11.0
RMSE <i>a priori</i> [ppm] (Revised Boundary)	7.2	10.0	8.4	9.8	11.0
RMSE <i>a posteriori</i> [ppm] (Gerbig Boundary)	7.2	9.8	8.9	8.8	12.0
RMSE <i>a posteriori</i> [ppm] (Revised Boundary)	7.1	9.7	8.4	8.5	11.0
R <i>a priori</i> (Gerbig Boundary)	0.61	0.27	0.62	0.17	0.44
R <i>a priori</i> (Revised Boundary)	0.57	0.21	0.60	0.11	0.39
R <i>a posteriori</i> (Gerbig Boundary)	0.61	0.29	0.62	0.39	0.38
R <i>a posteriori</i> (Revised Boundary)	0.57	0.23	0.60	0.37	0.35

The statistics of *a priori* and *a posteriori* STILT+VPRM results compared to observations of boundary layer airborne data show structure when aggregated by altitude, as shown in Figure 4.16. The left panel shows that the altitude structure is the same in *a priori* and *a posteriori* results, with more negative bias in model results closer to the surface. This indicates that the surface vegetation model is taking up too much CO₂, either due to persistently biased environmental drivers or an incorrect parameter value. The optimization reduces total bias, but the gradient in mean residuals is not corrected through optimization. A partial explanation is provided by the right panel, which shows a gradient in variance of the model with increasing model variance near the surface. The model most closely matches the observations in the well-mixed part of the boundary layer least affected by surface gradients.

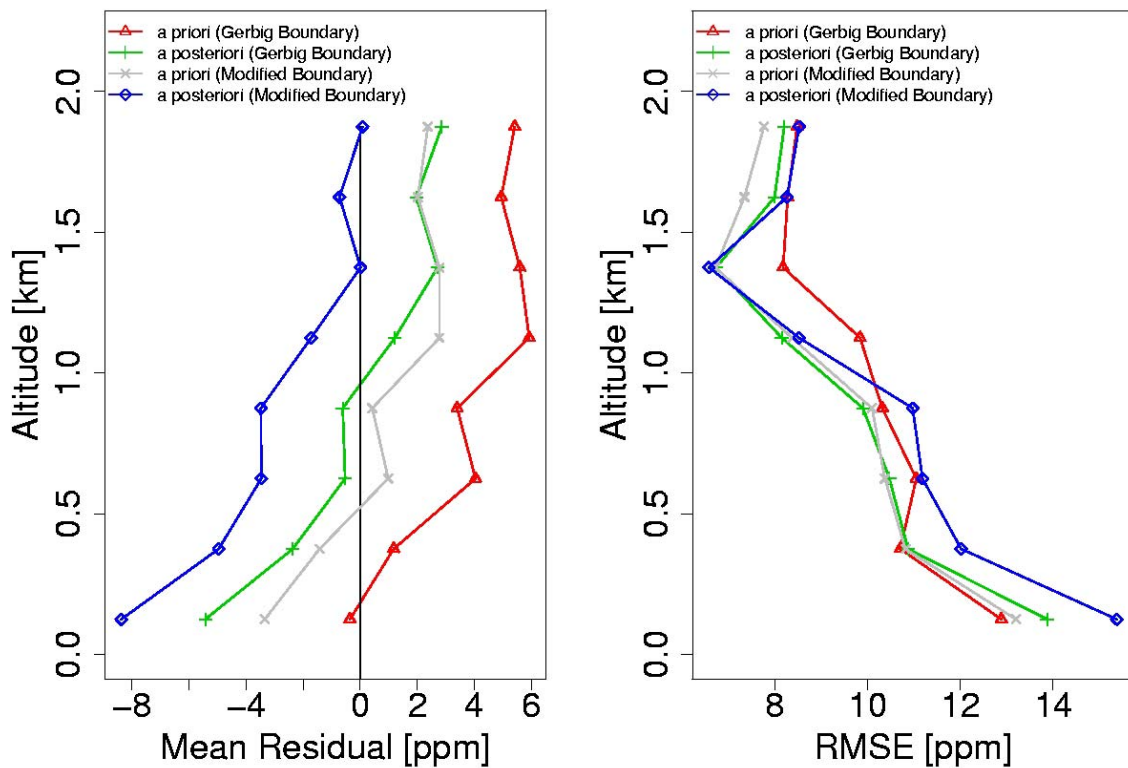


Figure 4.16 – Comparison of boundary layer STILT+VPRM results to observations, aggregated by 250-m altitude bins. A priori and a posteriori results are shown for inversions using both potential boundary conditions.

There are two potential reasons for the gradients seen in Figure 4.16 and the distinction between them is indefinite, if only the airborne results are considered. First, there may be too much CO₂ uptake near the surface, but wide variance in the near-surface modeled mixing ratios is greater than the uptake error, preventing the inversion from providing any constraint. Second, STILT+VPRM cannot effectively capture the covariance between the daily growth of the atmospheric boundary layer and the daily cycle of carbon uptake. Both explanations ultimately revolve around the inability of the transport model to adequately characterize boundary layer dynamics. In both cases, the misrepresentation of boundary layer dynamics in the model actually prevents an optimization of CO₂ observations from constraining surface flux parameters.

4.6 Conclusion

The regional “network” of observations assembled from New England and southern Quebec in July-August 2004 is an especially dense set of atmospheric CO₂ concentration data to constrain a surface exchange model, one with enough spatial and temporal coverage to be fully representative of the region. It might be considered a short term prototype for the structured, coordinated observational networks envisioned to better capture terrestrial variations of atmospheric CO₂ concentrations in the future. We have shown that a dataset that is dense both temporally and spatially is not only advantageous, but necessary to fully characterize regional CO₂ exchange because spatial and temporal correlations are strong, and have to be characterized to obtain meaningful fluxes from an inversion. Continuous surface tower data are nicely complemented by airborne data with region-wide spatial coverage and vice versa.

In parallel with continuing development of observational networks, data assimilation methods have been developed to utilize the surface flux signature contained in terrestrial CO₂ concentration to better constrain vegetation parameterizations. The STILT+VPRM receptor oriented modeling framework is comparable to such efforts in complexity, but has a number of distinct advantages – it transparently incorporates information from eddy covariance data through the initial calibration of VPRM parameters, it has a limited total number parameters, it is computationally efficient, and has explicitly defined boundary conditions. The *a priori* model reasonably captures both the day-to-day and seasonal variations in CO₂ concentration observations in many different environments, most effectively in the deciduous and mixed forest ecosystems that make up New England and southern Quebec.

It is therefore somewhat unexpected that Bayesian inversion of such a dense dataset to constrain a relatively small number of parameters in the surface source function provides minimal added constraint to the surface parameters. Whereas the current paradigm of data assimilation posits that the most correctable source of error when modeling terrestrial CO₂ observations lies in the representation of biosphere exchange, our results show that in some cases model errors not associated with surface source function can provide a limitation on how much data assimilation can improve model performance. Careful attention must be paid to local atmospheric transport, large scale transport boundary conditions, boundary layer dynamics, environmental drivers for surface fluxes (e.g. radiation), and tracer boundary fields because any one, or some combination, can make optimization of surface flux parameters ineffectual.

In the present study, optimization of the boundary layer airborne data provides important conclusions about the dynamics of the STILT+VPRM framework. The strong altitude gradient towards decreased model fidelity to observations near the surface coupled to the altitude gradient towards a more negative concentration bias, associated with stronger surface uptake, indicates that the surface flux model is taking up carbon too vigorously, but either the variance near the surface is too great for a parameter optimization to correct it or the model cannot adequately capture the covariance between the daily increase in surface uptake and growth of the boundary layer. Because most other data assimilation methods rely on similar atmospheric transport models and the VPRM has been shown to reliably capture forest surface fluxes (Pathmathevan et al., 2006), there is no reason to assume the STILT+VPRM framework is more or less prone such errors than other schemes, and the boundary layer data assimilation presented here is cautionary for future studies.

Nearly all the data used in this study is currently available on the web, much of it from the COBRA-Maine website (<http://www.deas.harvard.edu/cobra/>). Future work should test whether other data assimilation schemes utilizing COBRA-Maine airborne data obtain similar results and if they are also limited by model errors not incorporated into the surface flux parameters. STILT+VPRM can be further developed to utilize different transport drivers (e.g. BRAMS) with different large scale transport boundary conditions (e.g. ECMWF rather than GDAS). There are also a number of airborne observations over North America, including for instance from the NASA DC-8 in INTEX-NA, which might be used to better constrain the remote boundary conditions upwind. These represent important stepwise improvements necessary before a fully

coupled land-atmosphere exchange model will be able to fully assimilate the information from terrestrial CO₂ concentration observations.

Chapter 5: Summary and Conclusions

This thesis has presented a complete model-data fusion study aimed at deriving regional-scale ($\sim 10^4 \text{ km}^2$) CO_2 flux estimates for summer 2004 in the northeast United States and southern Quebec. The observational strategy for the COBRA-Maine airborne campaign centered on conducting a series of Lagrangian influence-following experiments and maximizing the amount of vertical coverage throughout the target region. Most of the studies to date, including this one, have utilized the observations as an ensemble and left the Lagrangian experiments and a rich list of ancillary analysis opportunities for later. Assimilating the observations to constrain regional scale CO_2 fluxes is an important part of achieving the stated goals of COBRA-Maine and development of the VPRM as a data-driven diagnostic surface flux model is a major step forward. It provides a surface flux function for inverse analyses with a minimum number of parameters that already incorporates the rich information contained in eddy covariance measurements.

Linking the VPRM to STILT in the receptor oriented modeling framework creates a tool capable of realistically simulating atmospheric concentration observations in the *a priori* case and the potential for inversion of COBRA-Maine surface and airborne observations to create tight *a posteriori* constraints. From the carefully structured Bayesian optimization, which must include calculation of spatial and temporal correlations and the uncertainties associated with as many terms as possible, the combination of tall tower and airborne data can be inferred to place the most constraint on the source function. However, the surface source function is not necessarily sensitive to optimization. Unsystematic errors at the boundary, in characterization of the boundary

layer, or in environmental drivers can be consistently large enough in magnitude to prevent the observations from constraining the flux parameters. Although such errors have been noted separately elsewhere (Denning et al., 2003; Nicholls et al., 2004), focus has remained on the errors in the vegetation flux parameterization. Overall, the optimization presented provides an important counterexample to the usual CO₂ terrestrial data assimilation archetype, which is guided by the idea that the largest errors in a given coupled biosphere-atmosphere model arise from the inability to represent complex ecological processes rather than complex atmospheric ones.

Few studies to date have been able to assess the difficulties in model-data fusion presented here because prior surface flux models have been too simplified to provide realistic hourly gridded fluxes (e.g. Gerbig et al., 2003b) or the input data has been limited in scope (e.g. Nicholls et al., 2004). When combined with the expansive COBRA-Maine dataset, STILT+VPRM is well-suited to expose errors at the model-data interface because it is a reliable, data-driven surface model with a minimum number of parameters to optimize. The overall framework is sophisticated enough to simulate hourly variations in CO₂ concentration, but simple enough not to obscure the fundamental underlying connection between input data and model with a large number of tunable parameters. While STILT+VPRM may be unique in its ability to elucidate certain obstacles to using data assimilation to quantify regional scale CO₂ fluxes, it is not uniquely prone to those obstacles. Other optimization studies are likely to encounter similar difficulties. Nonetheless, creating innovative ways to structure the optimization may circumvent many of the difficulties encountered here.

Although important as a counter-example to the current data assimilation paradigm, avenues already exist to improve the STILT+VPRM framework. The correlation between BRAMS driven and EDAS-40 driven STILT+VPRM concentrations at Argyle points to potential problems in the NCEP-GDAS meteorological fields at the boundary of the North American domain. BRAMS still represents a next-generation STILT-driver due its ability to simulate convection and excellent mass closure, but future efforts might seek to initialize it with fields from the European Center for Medium-Range Weather Forecasts (ECMWF) reanalysis product, rather than GDAS. The observational CO₂ tracer boundary condition for the north and west could be expanded and much better constrained by including additional aircraft observations from the free troposphere during the time of the experiment, for example NASA DC-8 CO₂ observations collected during INTEX-NA. For daytime analyses, the University of Wisconsin GOES-derived radiation product can help diagnose and correct errors in the radiation driver fields. Other drivers, including temperature, are much less prone to error and have a far less substantial impact on VPRM surface flux calculations than radiation errors, so emphasis should center on improving radiation inputs.

The observational strategy for COBRA-Maine can be considered very successful, providing a dataset dense enough and sufficiently detailed to fully engage the data assimilation framework. Many of the results presented depend heavily on airborne observations in the atmospheric boundary layer, further reaffirming the overall value of airborne measurements to CO₂ budget investigations and validating efforts to include as much vertical profiling as possible over the widest possible range of altitudes. Further, the parameter constraints calculated confirm the expected value created by closely

linking airborne observations to a surface anchor point. Further opportunities for comparison to surface data still exist. For instance, concentration information has been directly employed in the STILT+VPRM framework, but no efforts have yet attempted to incorporate eddy covariance information from EOBS, Howland Forest, Harvard Forest directly into the analysis.

Lagrangian influence-following experiments lie at the heart of COBRA-Maine but remain mostly unexplored, suggesting that the ensemble data analyses done so far have mined only a fraction of the information from the COBRA-Maine data. Each Lagrangian experiment provides a new constraint for surface flux models through a detailed spatial snapshot, allowing direct calculation of fluxes from the influence region without need for a surface flux model. Extrapolation of Lagrangian analyses will be aided by the number cases available; 14 total single- or multi-day Lagrangian experiments were conducted in COBRA-Maine. Each experiment is analogous to a single controlled case study, limited in scope, and requires individualized analysis, but no COBRA-Maine influence following experiments have been examined to date except superficially. The potential to gain insight from detailed consideration of controlled experiments is enormous but so too are the analysis requirements. It will take a substantial investment of time and effort to fully realize the potential from the Lagrangian experiments. Explicit linkage to the surface sites, both flux and concentration measurement stations, is needed to generalize Lagrangian results beyond limited cases. Future flight planners should also take great care to choose target regions and suitable receptors closely associated with surface anchors, avoiding anomalous and meteorologically complex situations such as the

COBRA-Maine flights in areas synoptically influenced by Hurricane Alex on August 4th and 5th, 2004.

The scale of COBRA-Maine inversion studies can be expanded from regional to continental by analyzing the transit flights in a manner similar to Gerbig et al. (2003b), but instead utilizing the STILT+VPRM data assimilation framework. COBRA-2003 is a natural complement in this regard. The choice to first examine regional scale CO₂ fluxes in Maine and Southern Quebec using COBRA-Maine data, rather than continental scale fluxes using COBRA-2003 data revolved simply around the availability of EDAS-40 meteorological drivers in 2004, but not 2003. The implementation of BRAMS mitigates this problem and full continental scale analyses should now be possible. With the addition of four trans-continental legs from COBRA-Maine, the COBRA-2003 dataset takes on further value.

COBRA-Maine was a successful observation program in part simply due to the generous allocation of flight hours. Data assimilation for terrestrial CO₂ fluxes requires large amounts of data, more than is commonly recognized. Not all airborne programs are fortunate to have so many flight hours or to target an area with such an extensive array of surface observations. With limited resources, comprehensive characterization of the atmosphere in the region likely adds more value for model-data fusion studies than a short series of Lagrangian flights, especially if regional survey flights can repeatedly fly-by as many surface observations as exist in a given region. Lagrangian experiments can serve as controlled experiments to independently verify or counter results obtained from other analyses, but are likely difficult to extrapolate without the large number of replicates in COBRA-Maine. In any case, as many climbs and descents as possible

should be included, because the vertical coverage afforded by the COBRA-Maine airborne data is one of its greatest assets.

Adequate temporal coverage is also important. Anchoring airborne studies to towers is important, but so is flying regularly enough avoid undersampling the synoptic variability of the boundary layer in any given region. The decorrelation timescale in the boundary layer, an important consideration for designing observation programs with a regular airborne component, depends on vegetation fluxes and atmospheric turnover and the covariance between the two. COBRA-Maine data might in the future be used to rigorously determine the timescale needed to successfully capture synoptic variability in the boundary layer, although the sense provided here by the combination of tower and flight data indicates a 3-5 day timescale is needed. Bi-weekly or even weekly aircraft sampling programs may not fully capture variations in boundary layer CO₂ concentrations.

In the larger sense, STILT+VPRM is an important intermediate step towards fully coupled biosphere-atmosphere data assimilation frameworks which can utilize a wide spectrum of ecological and atmospheric data inputs and can predict regional and continental scale CO₂ fluxes. The COBRA-Maine dataset provides a dense input to develop improved model-data fusion methods and serves an important role as one in a series of exploratory efforts to determine how more permanent observing networks should be designed. If CO₂ data assimilation methods are to be built around improved permanent terrestrial observation networks and vice versa, as is currently envisioned, data collection and modeling techniques both must continue to be informed from their common interface.

References

- Andres R. J., G. Marland, I. Fung, and E. Matthews, A 1° x 1° distribution of carbon dioxide emissions from fossil fuel consumption and cement manufacture, 1950-1990. *Global Biogeochemical Cycles*, 10, 419-429, 1996.
- Bakwin, P. S., P.P. Tans, D. F. Hurst, and C. Zhao, Measurements of carbon dioxide on very tall towers: results of the NOAA/CMDL program. *Tellus*, 50B, 410-415, 1998.
- Bakwin, P. S., P. P. Tans, B. B. Stephens, S. C. Wofsy, C. Gerbig, and A. Grainger, Strategies for measurement of atmospheric column means of carbon dioxide from aircraft using discrete sampling. *J. Geophys. Res*, 108, D4514, doi:10.1029/2002JD003306, 2003.
- Bakwin, P. S., K. J. Davis, C. Yi, S. C. Wofsy, J. W. Munger, L. Haszpra, and Z. Barcza, Regional carbon dioxide fluxes from mixing ratio data. *Tellus*, 56B, 301-311, 2004.
- Baldocchi, D.D., Assessing the eddy covariance technique for evaluating carbon dioxide exchange rates of ecosystems: past, present and future. *Global Change Biol.*, 9, 479 – 492, 2003.
- Baldocchi, D.D., L. K. Xu, and N. Kiang, How plant functional-type, weather, seasonal drought, and soil physical properties alter water and energy fluxes of an oak-grass savanna and an annual grassland. *Ag. Forest. Met.*, 123, 13-39, 2004.
- Bruhwiller, L.M.P., A. M. Michalak, W. Peters, D. F. Baker, and P. Tans, An improved Kalman Smoother for atmospheric inversions. *Atmos. Chem. Phys.*, 5, 2691-2702, 2005.
- Box, G. E. P, G. M. Jenkins, and G. C. Reinsel, *Time Series Analysis*. 3rd Ed. 592 pp. Prentice Hall, Upper Saddle River, N. J, 1994.
- Camargo, R and P. L. Silva Dias, The mesoscale adjustment in Paranaguábay: Case study of the period 10 to 25 August 1993. *Rev. Brasil. Met.* (in Portuguese), 15, 1-13, 2000.
- Chou, W. W., S. C., Wofsy, R. C. Harriss, J. C. Lin, C. Gerbig, and G. W. Sachse, Net fluxes of CO₂ in Amazônia derived from aircraft observations, *J. Geophys Res.*, 107 (D22), 4614, 10.1029/2001JD001295, 2002.
- Daube, B.C., Boering, K.A., Andrews, A.E. and Wofsy, S.C., A high-precision fast-response airborne CO₂ analyzer for in situ sampling from the surface to the middle stratosphere. *J. Atmospheric and Oceanic Technology*, 19, 1532-1543, 2002.
- Denning, A. S., M. Nicholls, L. Prihodko, I. Baker, P.-L. Vidale, K. Davis, and P. Bakwin, Simulated variations in atmospheric CO₂ over a Wisconsin forest using a coupled ecosystem-atmosphere model. *Global Change Biology*, 9, 1241-1250, 2003.

- Diak, G. R., J. R. Mecikalski, M. C. Anderson, J. M. Norman, W. P. Kustas, R. D. Torn, and R. L. DeWolf, Estimating land surface energy budgets from space - Review and current efforts at the University of Wisconsin-Madison and USDA-ARS. *Bull. Am. Met. Soc.*, 85, 65-78, 2004.
- Ebel, A., R. Friedrich, and H. Rodhe (Eds.) 1997, *Transport and Chemical Transformation of Pollutants in the Troposphere*, vol. 7, Tropospheric Modelling and Emission Estimation. Springer Verlag, New York, 1997.
- Emmons, L. K., G. G. Pfister, D. P. Edwards, J. C. Gille, G. Sachse, D. Blake, S. Wofsy, C. Gerbig, D.M. Matross, P. Nedelec, MOPITT validation exercises during Summer 2004 field campaigns over North America, *J. Geophys. Res.*, INTEX-NA Special Issue, *submitted*, 2006.
- Errico, R. M., What is an adjoint model? *Bull. Am. Meteorological Soc.*, 78, 2577-2591, 1997.
- Falge, E., D. Baldocchi, R. Olson, P. Anthoni, M. Aubinet, C. Bernhofer, G. Burba, R. Ceulemans, R. Clement, H. Dolman, A. Granier, P. Gross, T. Grunwald, D. Hollinger, N. O. Jensen, G. Katul, P. Kernonen, A. Kowalski, C. T. Lai, B. E. Law, T. Meyers, H. Moncrieff, E. Moors, J. W. Munger, K. Pilegaard, U. Rannik, C. Rebmann, A. Suyker, J. Tenhunen, K. Tu, S. Verma, T. Vesala, K. Wilson, and S. Wofsy, Gap filling strategies for defensible annual sums of net ecosystem exchange, *Ag. Forest. Met.* 107, 43-69, 2001.
- Friedlingstein, P., J. L. Dufresne, P. M. Cox, and P. Rayner, How positive is the feedback between climate change and the carbon cycle? *Tellus*, 55B, 692-700, 2003.
- Fung I. Y., S. C. Doney, K. Lindsay, and J. John, Evolution of carbon sinks in a changing climate. *Proceedings Nat. Acad. Sci.*, 102, 11201-11206, 2005.
- Gerbig, C., S. Schmitgen, D. Kley, A. Volz-Thomas, K. Dewey, and D. Haaks, An improved fast-response vacuum-UV resonance fluorescence CO instrument. *J. Geophys. Res.*, 104 (D1), 1699-1704, 1999.
- Gerbig, C., J. C. Lin, S. C. Wofsy, B. C. Daube, A. E. Andrews, A. E., B. B. Stephens, P. S. Bakwin, and C. A. Grainger, Towards constraining regional scale fluxes of CO₂ with atmospheric observations over a continent: 1. Observed spatial variability from airborne platforms, *J. Geophys. Res.*, 108, D4756, 10.1029/2002JD003018, 2003a.
- Gerbig, C., J. C. Lin, S. C. Wofsy, B. C. Daube, A. E. Andrews, A. E., B. B. Stephens, P. S. Bakwin, and C. A. Grainger, Towards constraining regional scale fluxes of CO₂ with atmospheric observations over a continent: 2. Analysis of COBRA data using a receptor oriented framework. *J. Geophys. Res.*, 108, D4757, 10.1029/2003JD003770, 2003b.

- Gerbig, C., S. R. Freitas, J. C. Lin, M. Longo, D. M. Matross, S. C. Wofsy, and M. A. Silva Dias, Consistent formulation of convective transport in a Lagrangian particle model. European Geosciences Union General Assembly 2005. Vienna, Austria, 24-29 April, 2005.
- Gloor, M., S. M. Fan, S. Pacala, J. Sarmiento, and M. Ramonet, A model-based evaluation of inversions of atmospheric transport, using annual mean mixing ratios, as a tool to monitor fluxes of nonreactive trace substances like CO₂ on a continental scale, *J. Geophys. Res.*, *104*, 14245-14260, 1999.
- Gloor, M., P. Bakwin, D. Hurst, L. Lock, R. Draxler, and P. Tans, What is the concentration footprint of a tall tower? *J. Geophys. Res.*, *106*, 17831-17840, 10.1029/2001JD900021, 2001.
- Grell, G.A. and D. Devenyi, A generalized approach to parameterizing convection combining ensemble and data assimilation techniques. *Geophys. Res. Letters*, *29*, 10.1029/2002GL015311, 2002.
- Gurney, K. R., R. M. Law, A. S. Denning, P. J. Rayner, D. Baker, P. Bousquet, L. Bruhwiler, Y. H. Chen, P. Ciais, S. Fan, I. Y. Fung, M. Gloor, M. Heimann, K. Higuchi, J. John, T. Maki, S. Maksyutov, K. Masarie, P. Peylin, M. Prather, B. C. Pak, J. Randerson, J. Sarmiento, S. Taguchi, T. Takahashi, and C. W. Yuen, Towards robust regional estimates of CO₂ sources and sinks using atmospheric transport models. *Nature*, *415*, 626-630, 2002.
- Gurney, K. R., R. M. Law, A. S. Denning, P. J. Rayner, B. C. Pak, D. Baker, P. Bousquet, L. Bruhwiler, Y. H. Chen, P. Ciais, I. Y. Fung, M. Heimann, J. John, T. Maki, S. Maksyutov, P. Peylin, M. Prather, M., and S. Taguchi, Transcom 3 inversion intercomparison: Model mean results for the estimation of seasonal carbon sources and sinks. *Global Biogeochemical Cycles*, *18*, GB1010, 10.1029/2003GB002111, 2004.
- Helliker B. R., J. A. Berry, A. K. Betts, P.S Bakwin, K. J. Davis, A. S. Denning, J. Ehleringer, J. B. Miller, M. P. Butler, and D. M. Ricciuto, Estimates of net CO₂ flux by application of equilibrium boundary layer concepts to CO₂ and water vapor measurements from a tall tower, *J. Geophys. Res.*, *109*, D20106, 10.1029/2004JD004532, 2004.
- Hollinger, D. Y., S. M. Goltz, E. A. Davidson, and J. T. Lee, Seasonal patterns and environmental control of carbon dioxide and water vapor exchange in an ecotonal boreal forest. *Global Change Biology*, *5*, 891-902. 1999.
- Hollinger, D. Y. and A. D. Richardson, Uncertainty in eddy covariance measurements and its application to physiological models. *Tree Physiology*, *25*, 873-885, 2005.

- Huete, A. R., H. O. Liu, K. Batchily, and W. V. Leeuwen, A comparison of vegetation indices global set of TM images for EOS-MODIS, *Remote Sens. Environ.*, *59*, 440-451, 1997.
- Kaminski, T and M. Heimann, Inverse modeling of atmospheric carbon dioxide fluxes. *Science*, *294*, 5541, 2001.
- Kitanidis, P. K., *Introduction to Geostatistics: Applications in Hydrogeology*, 249 pp., University of Cambridge Press, New York, N. Y., 1997.
- Law, B. E., E. Falge, L. Gu, D. D. Baldocchi, P. Bakwin, P. Berbigier, K. Davis, A. J. Dolman, M. Falk, J. D. Fuentes, A. Goldstein, A. Granier, A. Grelle, D. Hollinger, I. A. Janssens, P. Jarvis, N. O. Jensen, G. Katul, Y. Mahli, G. Matteucci, T. Meyers, R. Monson, J. W. Munger, W. Oechel, R. Olson, K. Pilegaard, K. T. Paw U, H. Thorgeirsson, R. Valentini, S. Verma, T. Vesala, K. Wilson, and S. Wofsy, Environmental controls over carbon dioxide and water vapor exchange of terrestrial vegetation. *Ag. and Forest Met.*, *113*, 97-120, 10.1016/S0168-1923(02)00104-1, 2002.
- Lin, J. C., C. Gerbig, S. C. Wofsy, A. E. Andrews, B. C. Daube, K. J. Davis, C. A. Grainger, The Stochastic Time-Inverted Lagrangian Transport Model (STILT): Quantitative analysis of surface sources from atmospheric concentration data using particle ensembles in a turbulent atmosphere. *J. Geophys. Res.*, *108*, D4493, 10.1029/2002JD003161, 2003.
- Lin, J.C., C. Gerbig, S.C. Wofsy, A. E. Andrews, B.C. Daube, C. A. Grainger, B.B. Stephens, P.S. Bakwin, and D.Y. Hollinger, Measuring fluxes of trace gases at regional scales by Lagrangian observations: application to the CO₂ Budget and Rectification Airborne (COBRA) study. *J. Geophys. Res.*, *109*, D15304, doi:10.1029/2004JD004754, 2004.
- Lin., J. C. and C. Gerbig, Accounting for the effect of transport errors on tracer inversions. *Geophys. Res. Lett.*, *32*, L01802, 10.1029/2004GL021127, 2005.
- Lin, J.C., C. Gerbig, S. C. Wofsy, B. C. Daube, D. M. Matross, V. Y. Chow, E. Gottlieb, A. E. Andrews, M. Pathmathevan, and J. W. Munger, What have we learned from intensive atmospheric sampling field programs of CO₂? *Tellus*, *58B*, in press, 2006.
- Loveland, T. R., B. C. Reed, J. F. Brown,, D. O. Ohlen, J. Zhu, L. Yang, and J. W. Merchant, Development of a Global Land Cover Characteristics Database and IGBP DISCover from 1-km AVHRR Data: *International Journal of Remote Sensing*, *21*,1,303-1,330, 2000.
- Marland, G., T. A. Boden, A. L. Brenkert, R. J. Andres, and J. G. Olivier, CO₂ from fossil fuel burning: Updates on the magnitude, distribution, and uncertainty of

- emission estimates. In *Extended Abstracts, Fifth International Carbon Dioxide Conference*, Cairns, Queensland, Australia, 4, 1997.
- Matross, D.M., A. Andrews, M. Pathmathevan, C. Gerbig, J.C. Lin, S.C. Wofsy, B.C. Daube, E.W. Gottlieb, J.T. Lee, C. Zhao, P.S. Bakwin, J.W. Munger, and D.Y. Hollinger, Estimating regional carbon exchange in New England and Quebec by combining atmospheric, ground-based, and satellite data. *Tellus*, 58B, in press, 2006.
- Medlyn, B. E., A. P. Robinson, R. Clement, and R. E. McMurtrie, On the validation of models of forest CO₂ exchange using eddy covariance data: some perils and pitfalls. *Tree Physiology*, 25, 839-857, 2005.
- Medvigy, D. M. The state of the regional carbon cycle: Results from a constrained coupled ecosystem-atmosphere model, Ph.D. Dissertation. Harvard University, Cambridge, MA, 2006.
- Michalak, A. M., L. Bruhwiler, and P. P. Tans, A geostatistical approach to surface flux estimation of atmospheric trace gases. *J. Geophys. Res.*, 109, D14109, doi:10.1029/2003JD004422, 2004.
- Michalak A. M., A. Hirsch, L. Bruhwiler, K. R. Gurney, W. Peters, and P. P. Tans, Maximum likelihood estimation of covariance parameters for Bayesian atmospheric trace gas surface flux inversions. *J. Geophys. Res.*, 110, D24107, doi:10.1029/2005JD005970, 2005.
- Mitchell, K. E., D. Lohmann, P. R. Houser, E. F. Wood, J. C. Schaake, A. Robock, B. A. Cosgrove, J. Sheffield, Q. Duan, L. Luo, R. W. Higgins, R. T. Pinker, J. D. Tarpley, D. P. Lettenmaier, C. H. Marshall, J. K. Entin, M. Pan., W. Shi, V. Koren, J. Meng, B. H. Ramsay, and A. A. Bailey, The multi-institution North American Land Data Assimilation System (NLDAS): Utilizing multiple GCIP products and partners in a continental distributed hydrological modeling system. *J. Geophys. Res.*, 109, D07S90, doi:10.1029/2003JD003823, 2004.
- Nicholls, M. E., A. S. Denning, L. Prihodko, P.-L. Vidale, I. Baker, K. Davis, and P. Bakwin, A multiple scale simulation of variations in atmospheric carbon dioxide using a coupled biosphere-atmospheric model. *J. Geophys. Res.*, 109, D18117, doi:10.1029/2003JD004482, 2004.
- Pathmathevan, M., S. C. Wofsy, D. M. Matross, X. Xiao, J. C. Lin, C. Gerbig, J. W. Munger, V. Y. Chow, E. Gottlieb, A Satellite-Based Biosphere Parameterization for Net Ecosystem CO₂ Exchange: Vegetation Photosynthesis and Respiration Model (VPRM). *Global Biogeochemical Cycles*, submitted, 2006.
- Patra, P. K., K. R. Gurney, A. S. Denning, S. Maksyutov, T. Nakazawa, D. Baker, P. Bousquet, L. Bruhwiler, Y-H. Chen, P. Ciais, S. Fan, I. Fung, M. Gloor, M. Heimann, K. Higuchi, J. John, R. M. Law, T. Maki, B. C. Pak, P. Peylin, M. Prather, P. J. Rayner, J. Sarmiento, S. Taguchi, T. Takahashi, and C.-W. Yuen, Sensitivity of

- inverse estimation of annual mean CO₂ sources and sinks to ocean-only sites versus all-sites observational networks. *Geophys. Res. Lett.*, *33*, L05814, doi:10.1029/2005GL025403, 2006.
- Peters, W., J. B. Miller, J. Whitaker, A. S. Denning, A. Hirsch, M. C. Krol, D. Zupanski, L. Bruhwiler, and P. P. Tans, An ensemble data assimilation system to estimate CO₂ surface fluxes from atmospheric trace gas observations. *J. Geophys. Res.*, *110*, D24304, 10.1029/2005JD006157, 2005.
- Rastetter, E. B., J. D. Aber, D. P. C. Peters, D. S. Ojima, and I. C. Burke, Using mechanistic models to scale ecological processes across space and time, *Bioscience*, *53* (1), 68-76, 2003.
- Raupach M. R., P. J. Rayner, D. Barrett, R. S. Defriess, M. Heimann, D. S. Ojima, S. Quegan, and C. C. Schimmlus, Model-data synthesis in terrestrial carbon observation: method, data requirements, and data uncertainty specifications. *Global Change Biology*, *11*, 378-397, 10.1111/j.136502486.2005.00917.x, 2005.
- Rodgers, C. D., *Inverse Methods for Atmospheric Sounding: Theory and Practice*, 238 pp., World Sci., River Edge, N. J, 2000.
- Rolph, G. D., *NOAA NCEP Eta Data Assimilation System (EDAS) archived by NOAA Air Resources Laboratory (The EDAS Archive)*. U.S. Department of Commerce, NOAA Air Resources Laboratory (ARL), 1997.
- Sánchez-Ccoylo, O. R. and M. F. Andrade, The influence of meteorological conditions on the behaviour of pollutants concentrations in São Paulo. *Environmental Pollution*, *116*, 257-263, 2002.
- Stephens, B. B., S. C. Wofsy, R. F. Keeling, P. P. Tans, and M. J. Potosnak, The CO₂ Budget and Rectification Airborne Study: Strategies for Measuring Rectifiers and Regional Fluxes, in *Inverse Methods in Global Biogeochemical Cycles*, edited by P. Kasibhatla, M. Heimann, P. Rayner, N. Mahowald, R. G. Prinn, and D. E. Hartley, pp. 311-324, American Geophysical Union, Washington, D.C., 2000.
- Stull, R. B., *An introduction to boundary layer meteorology*, 666 pp. Kluwer, Norwell, MA, 1988.
- Tans, P. P., I. Y. Fung, and T. Takahashi, Observational constraints on the global atmospheric CO₂ budget, *Science*, *247*, 1431-1438, 1990.
- Vay, S. A., J. H. Woo, B. E. Anderson, K. L. Thornhill, D. R. Blake, D. J. Westberg, C. M. Kiley, M. A. Avery, G. W. Sachse, D. G. Streets, Y. Tsutsumi, and S. R. Nolf, Influence of regional-scale anthropogenic emissions on CO₂ distributions over the western North Pacific, *J. Geophys. Res.*, *108*, 8801, 2003.

Washenfelder, R. A., G. C. Toon, J-F. Blavier, Z. Yang, N. T. Allen, P. O. Wennberg, D.M. Matross, and B. C. Daube, Carbon dioxide column abundance above the Wisconsin tall tower site, *J. Geophys. Res.*, in press, 2006.

Wofsy, S. C. and R. C. Harriss, 2002. *The North American Carbon Program (NACP)*, NACP Committee of the U.S. Interagency Carbon Cycle Science Program, U.S. Global Change Research Program, Washington, DC, 2002.

Xiao, X. M., Q. Y. Zhang, B. Braswell, S. Urbanski, S. Boles, S. Wofsy, M. Berrien, and D. Ojima, Modeling gross primary production of temperate deciduous broadleaf forest using satellite images and climate data. *Remote Sensing of the Environment*, 91,256-270, 2004.